UNIVERSITY OF TRENTO

Doctoral School in Civil, Environmental and
Mechanical Engineering

Curriculum 3. Modelling and Simulation

Riccardo Cavuoto

Phase-field and reduced peridynamic theories for fracture problems

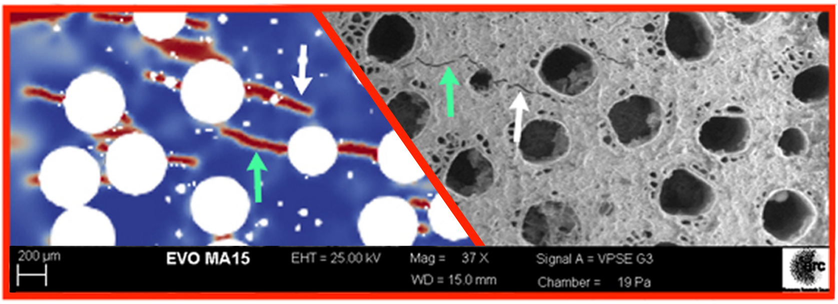
200 µm
EVO MA15
EHT = 25.00 kV
Mag = 37 X
WD = 15.0 mm
Signal A = VPSE G3
Chamber = 19 Pa

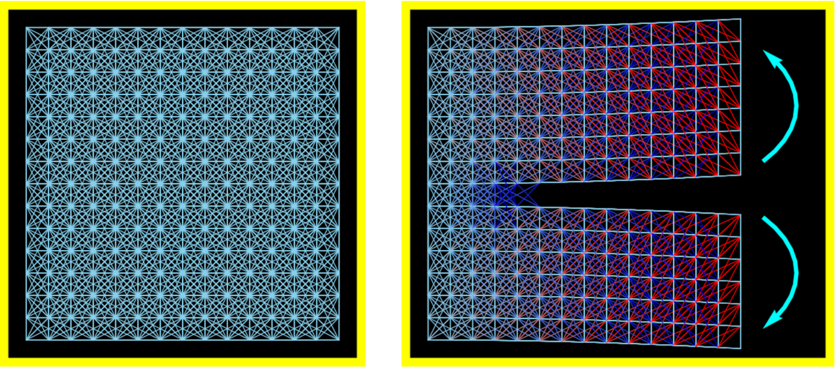

2021 - Doctoral thesis

Contents on this book are licensed under a Creative Common Attribution
Non Commercial - No Derivatives
4.0 International License, except for the parts already published by other publishers.

University of Trento
Doctoral School in Civil, Environmental and Mechanical Engineering
http://web.unitn.it/en/dricam
Via Mesiano 77, I-38123 Trento
Tel. +39 0461 282670 / 2611 - *dicamphd@unitn.it*

University of Trento

Doctoral Thesis

Phase-field and reduced peridynamic theories for fracture problems

Author:
Riccardo Cavuoto

Internal supervisors:
Prof. Davide Bigoni
Prof. Luca Deseri

External supervisors:
Prof. Massimiliano Fraldi

Modeling and Simulation – XXXIII cycle 2017/2020

Solid and Structural Mechanics Group (SSMG)
Department of Civil, Environmental and Mechanical Engineering (DICAM)

November 5, 2021

To my beloved family,
for their unwavering
and constant support.

Declaration of Authorship

I, Riccardo CAVUOTO, declare that this thesis titled, "Phase-field and reduced peridynamic theories for fracture problems" and the work presented in it are my own. I confirm that:

- This work was done wholly or mainly while in candidature for a research degree at this University.
- Where any part of this thesis has previously been submitted for a degree or any other qualification at this University or any other institution, this has been clearly stated.
- Where I have consulted the published work of others, this is always clearly attributed.
- Where I have quoted from the work of others, the source is always given. With the exception of such quotations, this thesis is entirely my own work.
- I have acknowledged all main sources of help.
- Where the thesis is based on work done by myself jointly with others, I have made clear exactly what was done by others and what I have contributed myself.

Signed:

Date:

Acknowledgements

I am deeply thankful to my advisors, Prof. Davide Bigoni, Prof. Luca Deseri, and Prof. Massimiliano Fraldi, for their continuous support and fruitful advices. Their guidance during the past three years has been pivotal to the development of this thesis and, more importantly, to my formation as a young researcher.
I am grateful to the whole staff of the *Department of Civil, Environmental and Mechanical Engineering* and to the *Solid and Structural Mechanics Group* for the support and kindness showed. More in particular, to Prof. Roberta Springhetti whose passion and care for teaching have been a model to me.

Separate, but not less affectionate, thanks go to Elena, Alessandro, Ilaria, Matteo, Farzaneh, Marco, Eleonora, Giovanni, Sara, Gianluca, Valentina, Andrea, Luca and Hamza, for creating a supporting and joyful research group. The interesting chats we have had together in the past three years have vastly broadened my mind, and helped me become a better person. What's more, special thanks go to Alessandro, Marco, Gianluca, Giovanni, Andrea and Luca, for including me in the stimulating *"scientific" dinners*.

Finally, my uttermost gratitude go to my family and to Federica. The very pillars of my life who supported me during both happy and tough moments.

Financial support from PRIN 2015 *Multi-scale mechanical models for the design and optimization of micro-structured smart materials and metamaterials*, 2015LYYXA8-006, is gratefully acknowledged.

"It is not him who commences but rather him who perseveres."

Leonardo Da Vinci

UNIVERSITY OF TRENTO

Abstract

Department of Civil, Environmental and Mechanical Engineering
(DICAM)

Modeling and Simulation

Phase-field and reduced peridynamic theories for fracture problems

by Riccardo CAVUOTO

Several aspects of fracture nucleation and growth in brittle porous ceramics and in thin films are investigated, through analytical, numerical modelling, and experimental validation.

A mechanical experimental characterization has been developed for a porous ceramic, namely, a 3D apatite, characterised by an oriented porosity and used for biomedical applications. The ceramic is produced from wood, so that the resulting porosity evidences a multi-scale nature, a feature which determines peculiar failure mechanisms and an unprecedented porosity/strength ratio. In particular, the material exhibits an exfoliation-type failure, resulting in a progressive loss in mechanical properties, occurring for compression tests parallel to the grains and for highly slender specimens. A similar cohesive-brittle behavior is also found when the compression is applied in the direction orthogonal to the porous channels, regardless of the shape ratio of the specimen. An in-depth analysis of this response is performed by means of a phase-field model. After calibrating the model, stress-strain curves and fracturing patterns are accurately reproduced. Furthermore, the effects of multi-scale porosity on mechanical behaviour is determined. Various strategies available in the literature for evaluating the properties of porous materials are compared to the proposed phase-field approach. The results open new possibilities for the prediction and characterization of complex fracturing phenomena occurring in highly porous ceramics, so to facilitate medical applications as structural bone repair.

An application of the peridynamic theory of continuum mechanics is developed to obtain a dimensional reduced formulation for the characterisation of through-thickness delamination of plates. The kinematic of the plate is carefully chosen to be composed of an absolutely continuous part and a zone where jumps in the displacements are allowed; in this way, the reduced form of the elastic bond-based peridynamic energy and the reduced

Lagrangian are explicitly retrieved in a closed form. The reduction generates a hierarchy of terms, characterizing the energy stored inside the plane element. A semi-analytical solution, obtained by means of a minimization procedure, is obtained for a test case and compared with finite element simulations. Despite the fact that the numerical model is fully three-dimensional (in other words, it is not reduced), this model leads to the same moment-curvature diagrams and nucleation/growth of the delamination surface found with the reduced formulation. Finally, convergence of the proposed reduced model to local elastic theory at vanishing internal length is determined, so that a reduced-localized cohesive model for fracture is retrieved.

Published papers

The main results presented in this thesis are summarized in the following papers:

1. D. Bigoni, R. Cavuoto, D. Misseroni, M. Paggi, A. Ruffini, S. Sprio and A. Tampieri. "Ceramics with the signature of wood: a mechanical insight". In: *Materials Today Bio* 5 (2020), pp. 100032.
2. S. Sprio, S. Panseri, M. Montesi, M. Dapporto, A. Ruffini, S.M. Dozio, R. Cavuoto, D. Misseroni, M. Paggi, D. Bigoni and A. Tampieri. "Hierarchical porosity inherited by natural sources affects the mechanical and biological behaviour of bone scaffolds". In: *Journal of the European Ceramic Society* 40 (2020), pp. 1717-1727.
3. R. Cavuoto, M. Fraldi, K. Dayal and L. Deseri. "A reduced peridynamic model for the delamination of thin films". (*submitted*).
4. R. Cavuoto, P. Lenarda, D. Misseroni, D. Bigoni and M. Paggi. "Phase-field modelling of failure in ceramics with multiscale porosity". (*submitted*)
5. R. Cavuoto, P. Lenarda, D. Misseroni, D. Bigoni and M. Paggi. "Crack trajectories in materials containing voids via phase-field modelling". (*submitted*)

Contents

Declaration of Authorship v

Acknowledgements vii

Abstract xi

Published papers xiii

1 Introduction 1

2 Ceramics with the signature of wood: a mechanical insight 9
- 2.1 Introduction . . . 9
- 2.2 The lacunar fractal nature of porosity . . . 12
- 2.3 Mechanical testings . . . 13
  - 2.3.1 Uniaxial compression test . . . 18
  - 2.3.2 Three-point bending tests . . . 23
  - 2.3.3 Ring tests . . . 26
  - 2.3.4 Ultrasonic tests . . . 29
  - 2.3.5 In situ mechanical tests and further analysis of crack patterns . . . 30
- 2.4 Biomorphic apatite vs. wood and bone: the Ashby plot . . . 33
- 2.5 Conclusions . . . 35

3 Failure of porous ceramics via phase-field modelling 37
- 3.1 Introduction . . . 37
- 3.2 The phase-field approach to fracture . . . 39
  - 3.2.1 The regularised variational formulation . . . 40
  - 3.2.2 Weak form of the variational problem . . . 41
  - 3.2.3 Finite element formulation . . . 41
  - 3.2.4 Newton-Raphson procedure . . . 42
- 3.3 Crack trajectories in plates with holes . . . 43
- 3.4 Two scales porosity and mesh generation . . . 44
- 3.5 The effect of the porosity on the elastic properties . . . 47
- 3.6 Crack propagation in a material with two-scale porosity . . . 51
- 3.7 Results and conclusions . . . 56

4 Reduced peridynamics for delamination of thin films 59
4.1 Introduction . . . 59
4.2 A brief review of bond-based peridynamics . . . 61
4.3 A dimensionally-reduced model for thin plates . . . 64
  4.3.1 Kinematics . . . 65
  4.3.2 Damage . . . 65
  4.3.3 Lagrangian formulation . . . 66
  4.3.4 Hierarchical form of the reduced pairwise potential function . . . 68
  4.3.5 A comparison with numerical results . . . 70
4.4 Convergence to a local elastic model . . . 73
  4.4.1 Peridynamic parameter evaluation . . . 73
  4.4.2 Displacement scaling . . . 74
  4.4.3 The scaling of the crisis criterion . . . 75
  4.4.4 Localised energy in plane strain . . . 76
  4.4.5 Kirchhoff-like plate under mode I delamination . . . 78
4.5 Conclusions . . . 79

Bibliography 81

List of Figures

1.1 A sequence of photos taken during a uniaxial compression test of a cylindrical sample of BA. The instants when the photos have been taken are marked on the stress/strain curve, Fig. 1.3 on the left. Note the progressive exfoliation of the sample, strongly enhancing toughness and related to the peaks in the stress/strain diagram. 2

1.2 A sequence of photos taken during a uniaxial compression test of hydroxyapatite samples. The instants when the photos have been taken are marked on the stress/strain curve, Fig. 1.3 on the right. Note the abrupt failure of the specimen immediately following the appearance of a splitting crack. . . . 2

1.3 Stress/strain behaviour of a BA sample (on the left) and of a HA sample (on the right) subject to uniaxial compression, parallel to the grain for BA. The green spot identifies the peak strength, while a straight line drawn through two blue spots was used to evaluate the Young modulus, $E = \tan\alpha$. The superior toughness of BA is evidenced by the slow load fall, contrasting with the sharp jump to zero displayed by HA. 3

1.4 Ashby chart reporting Young modulus vs porosity for biomorphic apatite, loaded parallel ($BA_{//}$) and perpendicular ($BA_{\perp}$) to the microtubule structure ('grain' in the following, a nomenclature borrowed from the wood from which BA was obtained), and bones. 3

1.5 Crack pattern in a BA sample tested under compression orthogonal to the grains (upper part). Phase-field simulating crack pattern in a porous material with two scales of porosity (lower part). 4

1.6 Photoelastic experiment of a tensile test on a v-notched PMMA plate, showing a crack 'attracted' by a circular void (upper part) and its simulation using the phase-field approach (lower part). 5

1.7 Left: comparison between FEM analysis and the semi-analytical reduced formulation of a clamped plate, subjected to two opposite couples acting on the free-end (see the inset). The analysis has been continued until the end (or loaded) section reached a value of curvature of $\chi_0 = 3.0\ 10^{-3}/L$ (where L is the length of the plate). Right: deformed shape of the free-end of the plate subjected to the applied bending moments. The colours indicate the mean strain level in the plate. 8

2.1 Ashby charts reporting Young modulus vs strength (upper part) and vs porosity (lower part) for biomorphic apatite, loaded parallel ($BA_{//}$) and perpendicular ($BA_{\perp}$) to the microtubule structure ('grain' in the following), for rattan wood (from which BA was obtained), and bones. 11

2.2 SEM image of the microstructure of biomorphic apatite showing long open channels surrounded by finer alveolar closed pores. 12

2.3 SEM images of cross sections biomorphic apatite, BA, and corresponding apparent porosity identified on the basis of the application of an *ad hoc* image analysis software with a filter index of 0.2. In particular: (a) 38× SEM image of BA; (b) At 38×, the porosity is detected to be 14.6%; (c) 100× SEM image of BA; (d) At 100×, the porosity is detected to be 19.0%; (e) 250× SEM image of BA; (f) At 250×, the porosity is detected to be 27.0%. The image correlation software shows that porosity is increasing with the magnification and this reveals the the lacunar fractality of the cross-section domain. 14

2.4 Increase of apparent porosity for BA with filter index at different magnification scales, showing the lacunar fractal nature of BA. 14

2.5 Local fractal dimension D (which quantifies the porosity) as a function of r (the lateral side division of the image in the box-counting algorithm). 15

2.6 XRD pattern of one sample of BioApatite used for mechanical tests, where the dots point to reflections addressing the β-TCP phase. All the unmarked peaks point to HA phase. 15

2.7 A sequence of photos taken during a uniaxial compression test of a cylindrical sample of BA. The instants when the photos have been taken are marked on the stress-strain curve (Fig. 2.9 on the left) reported in the the following. Note the progressive exfoliation of the sample, strongly enhancing toughness and related to the peaks in the stress-strain diagram. 19

2.8 A sequence of photos taken during a uniaxial compression test of hydroxyapatite samples. The instants when the photos have been taken are marked on the stress-strain curve (Fig. 2.9 on the right) reported in the the following. Note the abrupt failure of the specimen immediately following the appearance of a splitting crack. 19

2.9 Stress-strain behaviour of a BA sample (#1, on the left) and of a HA sample (#1, on the right) subject to uniaxial compression, parallel to the grain for BA. The green spot identifies the peak strength, while a straight line drawn through the two indicated blue spots was used to evaluate the Young modulus $E = \tan\alpha$. The superior toughness of BA is evidenced by the slow load fall, contrasting with the sharp jump to zero displayed by HA. 20

2.10 A sequence of photos showing progressive failure during uniaxial compression orthogonal to the grain of a BA prismatic sample (from set #4, geometrical and mechanical properties reported in Table 2.4). 21

2.11 Stress-strain behaviour of a BA sample compressed parallel to the grain. The green spot identifies the peak strength, while a straight line drawn through the two indicated blue spots was used to evaluate the Young modulus $E = \tan\alpha$. 21

2.12 A sequence of photos taken during a three-point bending test on prismatic sample of biomorphic apatite (BA set # 1), tested in the direction parallel to the grain. The growth of a tensile fracture is clearly documented (see the insets marked blue and green; the inset marked red shows a detail of the loading blade). 23

2.13 Tensile stress-strain behaviour of BA (Set #1, on the left) and of HA (Set # 2, on the right) from a three-point bending test, parallel to the grain for BA. The green spot identifies the peak strength, while a straight line drawn through the two indicated blue spots was used to evaluate the Young modulus $E = \tan\alpha$. The superior toughness of BA is highlighted by the failure strain much higher than in the HA sample. 24

2.14 A sequence of photos taken during a three-point bending test on biomorphic apatite prismatic samples (Set #4) tested in the direction orthogonal to the grain. Note the growth of a tensile fracture. 25

2.15 Tensile stress-strain behaviour of BA (Set #4) from a three-point bending test, with tensile stress parallel to the grain. The green spot identifies the peak strength, while a straight line drawn through the two indicated blue spots was used to evaluate the Young modulus $E = \tan\alpha$. The high toughness of BA is highlighted by the slow load fall. 26

2.16 A sequence of photos taken during a ring compression test on biomorphic apatite, BA, tubular samples (Set #3) tested in the direction orthogonal to the grain. The growth of tensile fractures is clearly documented (see the insets). . 27

2.17 Tensile stress-strain behaviour of BA (Set #3) from a ring compression test test, with tensile stress parallel to the grain. The green spot identifies the peak strength, while a straight line drawn through the two indicated blue spots was used to evaluate the Young modulus $E = \tan\alpha$. The high toughness of BA is highlighted by the slow load fall. 28

2.18 Amplitued of the signal versus time for two ultrasonic tests on a BA sample (Set #1, on the left) and on a HA sample (Set #1, on the right) at two different frequencies (0.5 and 1.0 MHz) 29

2.19 stress-strain curve of BA specimens tested in situ with a SEM under uniaxial compression at two levels of friction (at the specimen/platens contacts) and for eccentric loading. 32

2.20 Specimen tested under uniaxial compression with high friction. On the left: view of the specimen at failure; on the right: cracks at failure. 32

2.21 Specimen tested under uniaxial compression in side the SEM in conditions of low friction. On the left: view of the specimen at failure (note the high density polyethylene layer of black colour); on the right: cracks at failure. . . 32

2.22 BA specimen tested under eccentric compression in situ with a SEM and shown at failure on the left (note the paperboard layers in contact with the sample); cracks at failure are detailed on the right. 33

2.23 A sequence of photos showing progressive failure (involving exfoliation by fibre buckling) of a rattan wood specimen during uniaxial compression. . . . 34

2.24 stress-strain behaviour of a rattan wood sample subject to uniaxial compression (on the left) and three-point bending (on the right), parallel to the grain. The red spots (in the compression plot) identify different stress levels corresponding to different definitions of failure. A straight line drawn through the two indicated blue spots was used to evaluate the Young modulus $E = \tan\alpha$. 34

3.1 SEM image of a BA sample undergoing an uniaxial compression test. A crack nucleates at the external surface of a void, where a tensile stress locally develops, although the mean stress in the sample is compressive. Note also the porosity at macro and meso levels. 38
3.2 Tensile test on a v-notched PMMA plate with a single hole. 44
3.3 Left: Probability density function (PDF) representing the distribution of the voids' radius, r, in a typical BA specimen and evidencing a double porosity (macro-porosity is marked in blue, while meso-porosity in green). Function f reported in red is an interpolating function for the density distribution of BA samples. Right: An example of a sample generated in silico, displaying a double porosity, in agreement with our experimental data and resembling the transverse section of the rattan wood from which the BA has been obtained. 45
3.4 From left to right: finite element meshes of the specimen in-silico tested at increasing porosity. 46
3.5 Mesh sensitivity analysis: strength and stiffness dimensionless ratios as functions of the mesh and for different values of macro-porosity. 47
3.6 Evolution of the crack pattern in the deformed mesh for subsequent compressive loading steps for sample S2 ($\Phi_{\text{macro}} = 20\%$) at increasing values of displacement applied at the two lateral edges. 48
3.7 Simulations of the mean stress-strain response for porous specimens undergoing uniaxial compression. Only a macro porosity is present. 49
3.8 On the left: overall peak stress (normalized with respect to the matrix strength) as a function of macroporosity; on the right: overall Young's Modulus as a function of macro-porosity. The Hashin$-$Shtrikman upper bound and Coble$-$Kingery approach give good approximation of the scatter of the data. 50
3.9 Deformed meshes (up) and phase-field evolution (down) for samples tested under uniaxial compression in the horizontal direction. 51
3.10 MSA prediction of the cross-section where nucleation can occur in a specimen with $\Phi_{\text{macro}} = 20\%$ (on the left) and with $\Phi_{\text{macro}} = 40\%$ (on the right). . 51
3.11 Energy evolution in the specimen S2 ($\Phi_{\text{macro}} = 20\%$, on the left) and S16 ($\Phi_{\text{macro}} = 40\%$, on the right) as a function of the horizontal displacement (u). W stands for the maximum of the input energy; *input* stands for input energy; *dissipated* for the dissipated energy; *strain* for the strain energy. Points b,c and d are those referring to Figures 3.6-3.7. 52
3.12 Mean stress vs mean strain for specimens with a macro-porosity equal to 15% (left) or to 25% (right) at increasing meso-porosity. 53
3.13 Summary of the overall mechanical properties for porous materials with different void sizes. On the left: overall stiffness (continuous lines) and strength (dashed lines) as functions of macro-porosity, for different values of meso-porosity. On the right: overall stiffness (continuous lines) and strength (dashed lines) as functions of meso-porosity, for different values of macro-porosity. 53
3.14 Dimensionless peak stress (left) and Young's modulus (right) versus total porosity for samples characterised by double porosity. 54
3.15 Density plot for the normalised Young's Modulus and normalised strength of the specimens as functions of macro and meso porosity. 54

3.16 Energy evolution (normalised with respect the total energy input W) for samples with double porosity. Macro-porosity is 25% (left) and 30% (right) and meso-porosity 10% (left) and 5% (right). *Input*, which stands for input energy, evaluated as the scalar product between the imposed displacement and the traction at the right boundary of the samples; 54
3.17 Phase-field evolution of sample S2D. The sample is characterised by a macro-porosity Φ_{macro} of 25% while meso-porosity Φ_{meso} amounts to the 10%. Meso pores are responsible for two mechasims: for the nucleation (a-b) and accretion (c) of cracks; for connecting far away macro pores (d-e) ultimately leading to failure (e). 56
3.18 MSA prediction of the cross-section where damage should occur, and comparison with the results of the phase-field simulations for the specimens S2D ($\Phi_{\text{macro}} = 25\%$, $\Phi_{\text{meso}} = 10\%$). 56
3.19 Crack pattern in a BA sample tested under compression orthogonal to the main channels (up). Phase-field simulating crack pattern in a porous material with two scales of porosity (down). 57

4.1 On the left, the shape of the micromodulus function for different σ; b is a scalar parameter; $||\mathbb{C}||$ is the norm of the micromodulus tensor, δ is the horizon, d is the dimension of the problem, β is a constant quantity expressing the proportionality between the bond constant c and the horizon. On the right, the force $|f|$ exerted by the bonds for increasing bond length. In the present paper only discontinuous micromodulus functions have been considered 64
4.2 Deformation map $g(\boldsymbol{x})$ for a plate of thickness H undergoing delamination. Each point $P \equiv [x_1, x_2]$ of the reference configuration lying on the delamination surface jump to a new position specified by the vector $\boldsymbol{j}[P]$. 66
4.3 Computation of the total energy necessary to break all the bonds connecting the material point $\boldsymbol{x}$ with those $\boldsymbol{x}'$ on the other side of the fracture surface h. . 67
4.4 Side-view of a clamped plate implemented in ANSYS. Bonds have been modeled as trusses. 71
4.5 Comparison between numerical and analytical model of a clamped plate subjected to two opposite couples acting on the free end. 72
4.6 Post-elastic behaviour of the analytical model showing normalised average strain (average strain devided by maximum average strain in the body) upon crack nucleation for the chosen load distribution. The displacement of the configuration are scaled by a factor of 100 in order to make the deformed shape appreciable. 72
4.7 Evolution of crack surface (in red) from undamaged beam (left) to damaged one (right). 73
4.8 Acting force versus curvature (on the left); acting force versus crack advancement. Nonlinear behaviour arises due to crack propagation once the energy stored in the peridynamic bonds reaches a critical value. 78
4.9 Sensitivity analysis performed on the nonlocal model for varying horizon (δ). Here, K is the bending stiffness, β is the constant quantity of equation (4.35), L is the length of the plate, H is the thickness, and α is a scalar depending on the load distribution. 78

List of Tables

2.1 Summary of the mechanical properties of the biomorphic apatite (BA), obtained from uniaxial compression, three-point bending, and compression ring tests on samples of different geometry (prismatic, cylindrical and tubular). All the mechanical properties are expressed in terms of their average $\pm$ the standard deviation: σ_c strength in compression, σ_t strength in tension, E_c Young modulus in compression, E_f Young modulus in flexure; index '$\|$' and '$\perp$' stand for parallel and orthogonal to the grains, respectively. Finally, ρ/ρ_0 is the ratio between the density and the reference density of 1.47 g/cm^3 to which all mechanical values have been reported. 17

2.2 Summary of the mechanical properties of commercial hydroxyapatite, obtained from uniaxial compression and three-point bending tests on prismatic samples. All the mechanical properties are expressed in terms of their average $\pm$ the standard deviation: σ_c strength in compression, σ_t strength in tension, E_c Young modulus in compression, E_f Young modulus in flexure; ρ/ρ_0 is the ratio between the density and the reference density of 1.47 g/cm^3 to which all mechanical values have been reported. 18

2.3 Mechanical characteristics from uniaxial compression tests on different stocks of BA and HA; compression is parallel to the grain for BA. On the left the averages of the geometrical properties of each stock are shown: ϕ is the main dimension of the samples' base (which corresponds to the outer diameter of samples #1, #2, #3, and to a side of prismatic samples #4); H the height; A the average cross-sectional area and ρ the average density. On the right the following average properties ($\pm$ standard deviation) are reported (from left to right): compressive strength; Young modulus. Finally, ρ/ρ_0 is the ratio between the density and the reference density of 1.47 g/cm^3 to which all mechanical values have been reported. 20

2.4 Mechanical characteristics from uniaxial compression tests orthogonal to the grain. All samples are prismatic, with the following average dimensions: B width; H height; S depth; A cross-sectional area; ρ density. On the right, the following average properties ($\pm$ standard deviation) are reported (from left to right): compressive strength; Young modulus. Finally, ρ/ρ_0 is the ratio between the density and the reference density of 1.47 g/cm^3 to which all mechanical values have been reported. 22

2.5 Mechanical characteristics from three-point bending tests on the different stocks of BA (with tension parallel to the grain) and HA. All the samples are prismatic, with the following average dimensions: B depth; H height; L length; ρ density. On the right the following average properties (± standard deviation) are reported (from left to right): tensile strength; Young modulus. Finally, ρ/ρ_0 is the ratio between the density and the reference density of 1.47 $\mathrm{g/cm^3}$ to which all mechanical values have been reported. 24

2.6 Mechanical characteristics from three-point bending tests with tension orthogonal to the grain. All the samples are prismatic, with the following average dimensions: B depth; H height; L length; ρ density. On the right the following average properties (± standard deviation) are reported (from left to right): tensile strength; Young modulus. Finally, ρ/ρ_0 is the ratio between the density and the reference density of 1.47 $\mathrm{g/cm^3}$ to which all mechanical values have been reported. 26

2.7 Mechanical characteristics from ring tests on BA samples (tensile stresses are orthogonal to the grain). All the samples are tubular, with the following average dimensions: H depth; r_o outer radius; r_i internal radius, and ρ density. On the right the following average properties (± standard deviation) are reported (from left to right): tensile strength; Young modulus. Finally, ρ/ρ_0 is the ratio between the density and the reference density of 1.47 $\mathrm{g/cm^3}$ to which all mechanical values have been reported. 28

2.8 Mechanical characteristics from ultrasonic tests on BA samples (parallel to the grain) and HA. All the samples are cylindrical, with the following average dimensions: H height; ϕ diameter; A cross-sectional area; ρ density. On the right the following average properties (± standard deviation) are reported (from left to right): wave velocity; uniaxial strain elastic modulus; Young modulus for two different values of Poisson's ratio. All reported values have not been normalised to the reference density. 30

2.9 Geometrical properties for the BA specimens tested *in situ* with a SEM and subject to different loading conditions. H is the height of the sample, w the width, t the thickness. ρ/ρ_0 is the ratio between the density and the reference density of 1.47 $\mathrm{g/cm^3}$ and p is the porosity 31

2.10 Mechanical characteristics from uniaxial compression tests and three-point bending (in both cases stress is parallel to the grain) on rattan wood. All the samples are prismatic, with the following average dimensions: H height; L span; ϕ base dimension; ρ density. On the right the following average properties (± standard deviation) are reported (from left to right): compressive strength; Young Modulus. 35

3.1 Sets of tested samples: Φ_{macro} stands for macro-porosity. 46

3.2 Mean value and standard deviation of Young's Modulus and peak stress for different values of the macro-porosity as obtained from simulations of compression tests. 49

3.3 Two porosities of the samples generated for in-silico testing. Φ_{macro} stands for the macro-porosity and Φ_{macro} represents the meso-porosity. 52

4.1 Parameters of the local equivalent material and geometry of the plate (up); nonlocal parameter of the peridynamic bond-based reduced model (down). . 71

List of Abbreviations

PD	**P**eridynamic theory
BPD	**B**ond-based **P**eridynamics
BA	**B**io-**A**patite

1

Introduction

Various mechanisms of fracture nucleation and propagation are analyzed in brittle-porous ceramics and in thin structures.

Mimicking the microstructure of natural materials in order to craft superior materials has been the objective of a massive research investment [1–11]. In particular, ceramics implementing a micro and nano structure almost identical to wood exhibit unprecedented mechanical performances. Due to the similar and exceptionally performing mechanical behaviour of wood and bone, biotemplating processes to fabricate 3-D functional ceramics (such as apatites) from natural wood for biomedical purposes have been proposed. The majority of these ceramics are subject to a fabrication process highly depending on sintering [4–7]. The latter process requires high temperatures, which ultimately degrades nanocrystalline, non-stoichiometric or metastable phases and reduces the biocompatibility of materials. Recently Tampieri et al. developed a new procedure to chemically transform rattan wood into a biomimetic hierarchically structured hydroxyapatite without resorting to sintering [12]. The new procedure can directly transform wood pieces into large hydroxyapatite scaffolds, preserving the original multi-scale structure through an heterogeneous reaction in supercritical condition directly applied to the 3-D state. The resulting material (called *biomorphic apatite*, BA, in the following) possesses a highly bioactive composition and is characterised by a multi-scale hierarchical pore structure, based on nano-twinned hydroxyapatite lamellae, very similar to the parent wood. In addition, BA shows a nano size structure and unprecedented mechanical properties due to great cohesion of the neo formed nano-crystals, which display a lacunar fractal nature (as will be shown in Section 2.1-2.2). The mechanical properties of BA are found to be exceptional [13], when compared to usual porous hydroxyapatite and other ceramics obtained from wood through sintering.

A systematic investigation of the mechanical behaviour and a morphological analysis (reported in Section 2.2), show that the fractal nature of BA is a feature which may justify its excellent damage tolerance. In fact, the fractality of the porosity explains the experimental observation that the fracture is not abrupt and straight, but evidences growth and tortuosity (as usual for

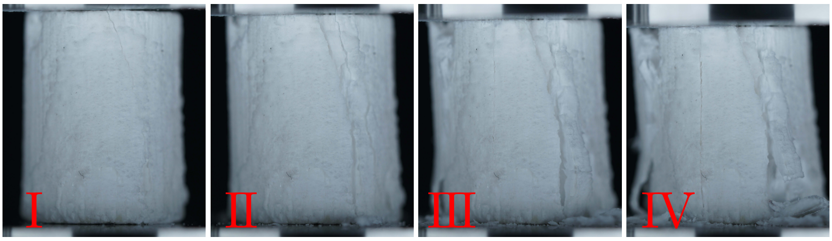

FIGURE 1.1: A sequence of photos taken during a uniaxial compression test of a cylindrical sample of BA. The instants when the photos have been taken are marked on the stress/strain curve, Fig. 1.3 on the left. Note the progressive exfoliation of the sample, strongly enhancing toughness and related to the peaks in the stress/strain diagram.

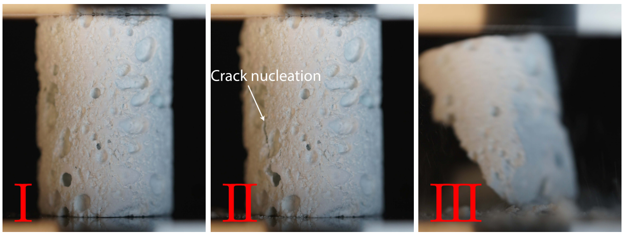

FIGURE 1.2: A sequence of photos taken during a uniaxial compression test of hydroxyapatite samples. The instants when the photos have been taken are marked on the stress/strain curve, Fig. 1.3 on the right. Note the abrupt failure of the specimen immediately following the appearance of a splitting crack.

bone) (see Figure 1.1). On the other hand, standard hydroxyapatite (HA) is characterised by abrupt failure of the specimen immediately following the appearance of a splitting crack (see Figure 1.2), a feature which affects the stress/strain response of compressed apatites. In Figure 1.3 BA is compared to HA, when subject to a uniaxial compression. A peak strength occurs for BA higher than for HA, both peaks occur practically at the same strain level, but while HA is abruptly crushed at that strain, exfoliation takes place for BA, which continues to carry load and attains a final strain of more than 35%, thus displaying a great toughness. The positioning of BA in an Ashby chart of Young Modulus vs porosity, show that BA occupies a zone free from ceramics and displays a similarity to the ligneous material from which it was 'born' and to several different bones, which evidences that the material is particularly suited for applications in biotechnologies, Figure 1.4. Results from an experimental campaign are presented in Section 2.3, based on multiple mechanical tests: uniaxial compression (in both a standard configuration and in-situ inside a SEM), three-point bending, ring tests, and ultrasound evaluation.

These mechanical tests show that: (i.) the strength in tension may exceed

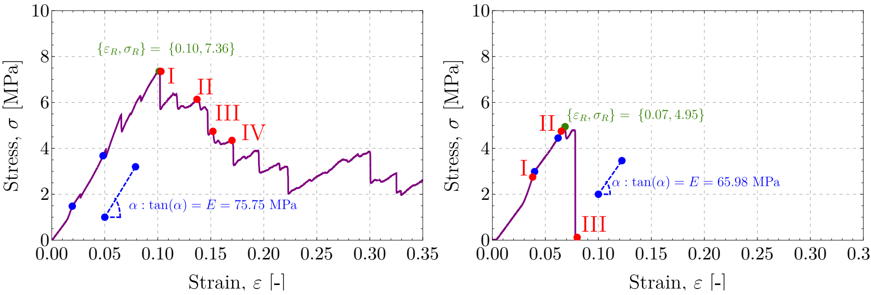

FIGURE 1.3: Stress/strain behaviour of a BA sample (on the left) and of a HA sample (on the right) subject to uniaxial compression, parallel to the grain for BA. The green spot identifies the peak strength, while a straight line drawn through two blue spots was used to evaluate the Young modulus, $E = \tan\alpha$. The superior toughness of BA is evidenced by the slow load fall, contrasting with the sharp jump to zero displayed by HA.

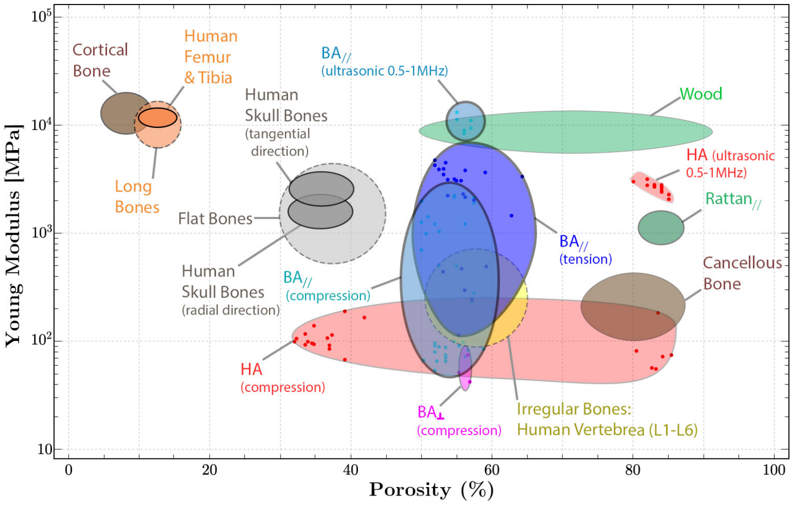

FIGURE 1.4: Ashby chart reporting Young modulus vs porosity for biomorphic apatite, loaded parallel ($BA_{//}$) and perpendicular ($BA_{\perp}$) to the microtubule structure ('grain' in the following, a nomenclature borrowed from the wood from which BA was obtained), and bones.

that in compression, (ii.) failure in compression involves complex exfoliation patterns, thus resulting in high toughness, (iii.) differently from sintered porous hydroxyapatite, fracture does not occur 'instantaneously', but its growth may be observed and it exhibits tortuous patterns that follow the original fibrillar structure of wood, thus yielding outstanding toughness (see Figure 1.5 upper part), (iv.) the anisotropy of the elastic stiffness and strength show unprecedented values when situations of stresses parallel and orthogonal to the main channels are compared. Despite being a ceramic material, BA displays a mechanical behaviour similar on the one hand to the ligneous material from which it was produced (therefore behaving as a 'ceramic with the signature of wood') and on the other to the cortical/spongy osseous complex constituting the structure of compact bone.

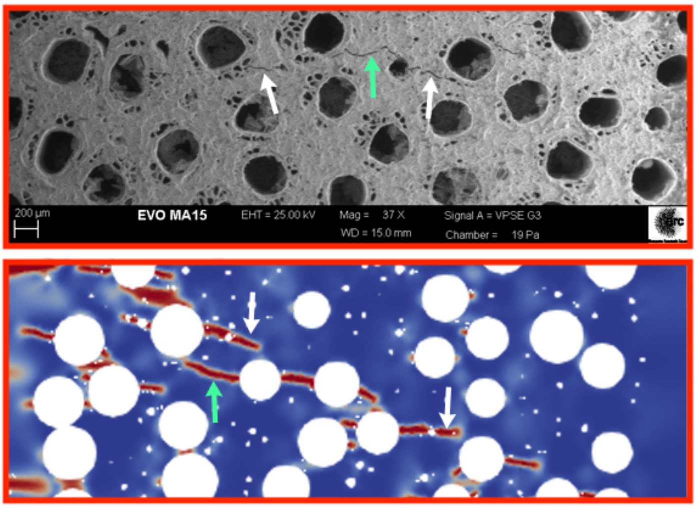

FIGURE 1.5: Crack pattern in a BA sample tested under compression orthogonal to the grains (upper part). Phase-field simulating crack pattern in a porous material with two scales of porosity (lower part).

Theoretical considerations and experiments show that fracture growth is strongly influenced by inhomogeneities [14–20]. Crack deviations from a rectilinear path usually enhance toughness [21, 22] and an isolated crack can even be stopped, when it hits a hole with smooth boundary. The so-called 'phase-field approach' has been developed to simulate fracture growth involving complex crack topologies. Following this approach, an approximation is introduced through the regularization of the crack topology, which then becomes smooth, by defining a phase field: a scalar field representing damage measured over the entire body under examination. Hence, the phase field interpolates between a state of complete damage and an undamaged state.

In Chapter 3, the ability of the approach to correctly model complex crack pattern is confirmed through careful experimental evaluation [23]. In particular, a comparison with photoelastic experiments performed on PMMA plates containing notches and circular holes, shows that the phase-field approach is particularly well-suited to describe crack trajectories. Fig. 1.6 reports the evolution of a crack growing from a notch during a tensile test on a PMMA plate containing an isolated circular void. Crack nucleation at the tip of the notch is visible in panel (1); horizontal crack propagation in panel (2). Crack visibly deviates from rectilinearity in panel (3) and finally touches the void in panel (4). The simulations reported in the figure demonstrate the quality of the phase-field approach to fracture. The ability of the phase-field to model complex fracture patterns stimulated the idea to analyse the effect that pores of different size can have on crack evolution in porous materials. Examples of materials where their multi-porous characteristics induce complex mechanical behaviours at failure are bone, porous carbides, and ceramics (in particular BA). In brittle materials, such as glass or ceramics, fracture nucleation primarily occurs under tensile stresses, but in the case of a porous material it may occur, and sometimes be even common (for instance as bone repair applications), for compressive loads, as shown in Fig. 1.5. In the figure a crack is visible, nucleating from the surface of a pore where the local stress is tensile, although the mean stress applied to the whole sample is compressive [24–26] [1]. The mechanical modelling of porous-brittle solids is primarily based on the void volume fraction (the average volume of voids per unit volume), which may be used as a simple parameter to determine the mechanical characteristics of a porous material [28–31]. With the knowledge of this parameter, the *minimal solid area method* (MSA) allows for a simple determination of the elastic stiffness of the material and of the peak strength [30]. This methodology, compared with the more sophisticate

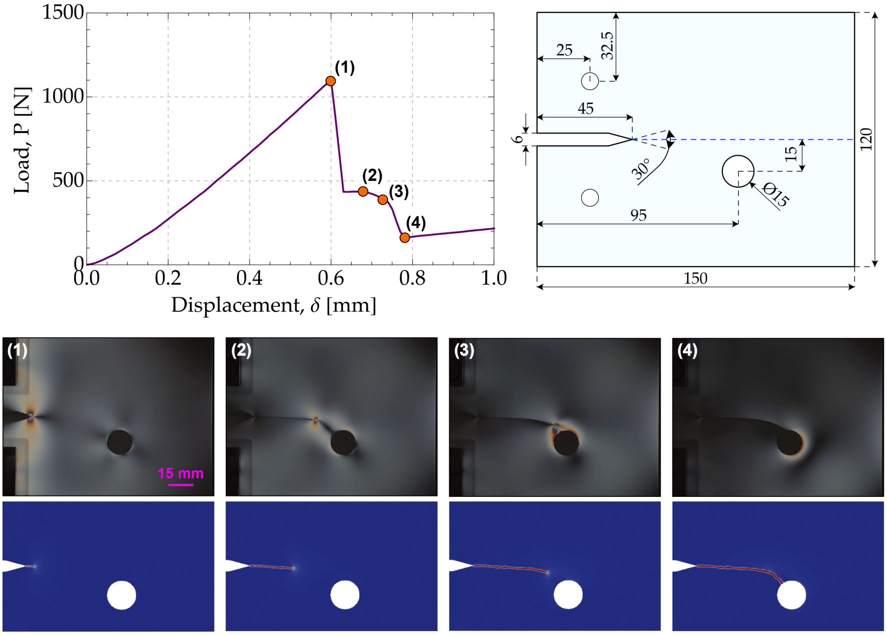

FIGURE 1.6: Photoelastic experiment of a tensile test on a v-notched PMMA plate, showing a crack 'attracted' by a circular void (upper part) and its simulation using the phase-field approach (lower part).

---

[1] Considering any sample of a material with a generic distribution of internal voids, and subject to compressive tractions on the external surface, the mean stress theorem [27] leads to the conclusion that the mean stress internal to the sample is compressive.

stress concentration effect method [32, 33], leads to the conclusion that pore shape has less influence than pore size on the global mechanical behaviour. However, multiscale porosity has been only scarcely analyzed so far [34], so that, in Chapter 3, the phase-field approach is shown to be successfully applicable to porous brittle material with multiscale porosity.
Simulations are shown to capture the main experimental features of failure, see Figure 1.5: (i.) large pores act as 'attractors' for cracks (the green arrow); (ii.) small pores act as 'attractors' for smaller cracks (white arrows); (iii.) small pores induce bridging effects, fostering crack propagation between distant macro-cracks (white arrow).
The phase-field approach implemented and used to simulate failure of porous brittle materials is therefore shown to represent an excellent tool in the design of mechanical pieces made up of such materials.

In Chapter 4, with regard to the recent framework of peridynamics [35], a reduced model is proposed for the characterization of through-thickness delamination of thin plates.
Composite materials, and in particular laminates, find several applications in the aerospace and automotive industries, because of their outstanding mechanical properties, such as strength and stiffness, combined with a low weight. Among the various type of damage that can affect their mechanical response, composite laminates are especially subject to delamination. Delamination is a type of failure which involves a loss of continuity of the material at an interface region, and which has negative consequences on the laminates strength and stiffness [36, 37]. Therefore, a strong effort has been developed to correctly model and predict its evolution, mainly through the application of Cohesive Zone Models (CZM) [38–43]. CZM assigns to the damage zones a traction-separation law which is cohesive and damage begins to develop when the stress reaches a limit defined with a constitutive law. The need for special techniques, such as CZM, to deal with delamination emerges from the fact that local theories of continuum mechanics relay on the definition of strain. Therefore, equilibrium equations require the displacement to be differentiable, a condition excluding involvement of jump discontinuities [44].
In this regard, strongly nonlocal theories which employs integrals to define the equilibrium equations are particularly well-suited. Among the many [45–48], peridynamics has gained the attention of the research community primarily because of its capability of treating fracture. Nevertheless, a very recent paper points the attention to a fully nonlocal theory of fractional order continua which seems to compete with peridynamics [49], although fracture and delamination has not yet been addressed there.

Peridynamics (PD) is a fairly recent nonlocal theory proposed in 2000 by S. A. Silling [35]. This approach can be regarded as the natural extension of molecular dynamics to a continuous medium and to arbitrarily large systems with long range interactions at the macroscale [50]. In the PD theory, the continuum is modelled as a collection of particles which can interact with one another through forces. The maximum distance between particles at which an interaction exists is called *horizon*. The type of interaction defines the kind of peridynamics at hand: a model where the forces acting on a pair of particles depend only on their own movement is called *bond-based* [51, 52]. An alternative form of PD, called *state-based*, has also been introduced in [53, 54]: there forces also depend on all the particles in their neighbourhood. PD has also been employed to model impact, explosion and high speed crashing [55–57].

The applications of PD to 2D elements have been thoroughly studied and numerical schemes have been developed to deal with these problems [58–60]. For instance, this is the case of debonding of multilaminates, which has been studied in [61–63] among others. Within 2D PD, dimensionally reduced formulations suitable for geometrically thin (nonlocal) solids have also been pursued. This is because they are particularly attractive as they can lead to faster computational algorithms and still lead to a good insight of the physical phenomenon (see e.g. [64, 65]). The proposed reduced models treat membrane tearing or in-plane failure, although they do not deal with damages occurring through the thickness, such as delamination.

From here on, we briefly outline the content of our work. In Chapter 4 it is in the framework of PD that a reduced model is proposed in this thesis for the characterization of through-thickness delamination of plates. Here, a reduced formulation of *bond-based* peridynamics, specifically tailored to account for through-thickness mode-I cracks, is introduced [66]. This is achieved first by carefully characterizing the kinematics. To this aim, the displacement field is additively decomposed in the sum of its absolutely continuous part and its jump one. In a more mathematical language, we would say that the natural functional space in which geometrical changes for the continua at hand are allowed is the one formed by functions of Special Bounded Variations, SBV, largely utilized in analysis and its applications (see e.g. [67]). The latter singles out both the sites of discontinuities and their magnitude. Further assumptions on both parts of the displacement field lead to a reduced form of the elastic bond-based PD energy. For such an effective energy the reduced Lagrangian is then explicitly retrieved. This procedure and the assumptions mentioned above generate a hierarchy of terms characterizing the strain energy stored inside the planar element. This hierarchy of functionals allows for a consistent variational approach, governing the search of unknown displacement fields by means of a minimization procedure. Semi-analytical solutions for test cases are then compared with numerical simulations. These are performed on fully three-dimensional systems and built by means of standard FEM analysis of PD bond-based body [68, 69], while the analytical model is based on the dimensionally reduced formulation previously described. The above mentioned comparison allows for showing that the numerical and analytical solutions exhibit a high degree of agreement, both in terms of moment-curvature relationship and in terms of nucleation and growth of the delamination surface (see Figure 1.7). A key result obtained in this thesis is the assessment of convergence between the proposed reduced model and local theories, when the *horizon*(δ) tends to zero. By enforcing a condition of bounded and non-vanishing energy the scaling of the displacement field with the horizon is

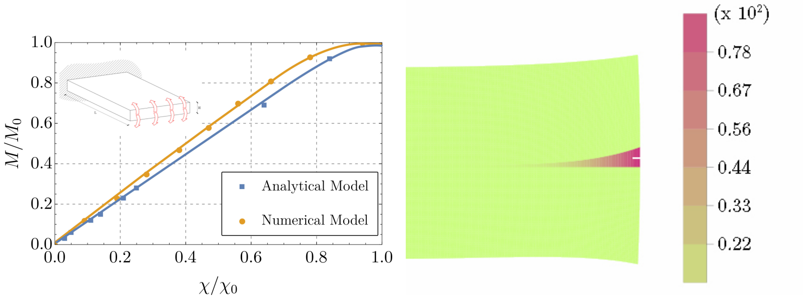

FIGURE 1.7: Left: comparison between FEM analysis and the semi-analytical reduced formulation of a clamped plate, subjected to two opposite couples acting on the free-end (see the inset). The analysis has been continued until the end (or loaded) section reached a value of curvature of $\chi_0 = 3.0\ 10^{-3}/\mathrm{L}$ (where L is the length of the plate). Right: deformed shape of the free-end of the plate subjected to the applied bending moments. The colours indicate the mean strain level in the plate.

established. Since the scaling of all the terms in the energy is then known, the nonlocal model can be localized and a cohesive reduced local formulation is retrieved. This is due to some terms of the energy associated to the jump part of the displacement surviving the limit operation.

2

Ceramics with the signature of wood: a mechanical insight

2.1 Introduction

Wood and bone are natural materials displaying a similar and exceptionally performing mechanical behaviour, which is rooted in their highly hierarchical and fibrous microstructure [70, 71]. Therefore, mimicking of this microstructure to produce superior materials has been the objective of a massive research investment [2, 3, 5–11, 72–85].

In this vein, ceramics implementing a micro and nano structure almost identical to wood can be easily believed to exhibit unprecedented mechanical performances and also to be ideal candidates for bone replacement. Following these ideas, biotemplating processes to fabricate 3-D functional ceramics (such as apatites) from natural wood have been proposed, all terminating with sintering [3, 5–7].

Recently Tampieri et al. developed a new procedure[1] to chemically transform rattan wood into a biomimetic hierarchically structured hydroxyapatite[87]. Differently from previous approaches where the wood was infiltrated with hydroxyapatite slurries and finally sintered to eliminate the organic component and to consolidate the final ceramic [6, 7], the new procedure can directly transform wood pieces into large hydroxyapatite scaffolds, preserving the original multi-scale structure through an heterogeneous reaction in supercritical condition directly in the 3-D state, without adopting any sintering process. This is an important advantage, because high temperature treatments can represent a serious drawback for the scaffold bioactivity[2]. The resulting ceramic material (referred in the following as 'biomorphic apatite', 'BA') not only maintains a highly bioactive composition and a multi-scale pore hierarchy almost identical to the parent wood (thanks to a careful control of the reaction kinetics that prevents critical deformations at all scales, and to the absence of sintering processes), but also shows nano size structure and unprecedented mechanical properties due to great cohesion of the neo formed nano-crystals [87]. BA represents a significant improvement in the development of 3-D inorganic devices with complex microstructure and multi-scale details, which are relevant for smart functionality, which is still an open challenge, due to the ineffectiveness of the current ceramic fabrication processes.

---

[1] Even if the details of the process are reported in [12, 86, 87], it may be important to mention that the maintenance of the complex architecture of wood was achieved through a chemical transformation process characterised by a very strict control of the reactions kinetics, which was obtained through the use of an equipment permitting the regulation and control of the temperature and pressure of reacting gases, thus establishing the more suitable thermodynamic conditions to reach a complete phase transformation in the whole solid [87]. Specifically, gas-solid reactions are strongly affected by various phenomena related to the adsorption of the gaseous reactant by the solid, the kinetic of nucleation and growth of the newly forming inorganic phase at the surface and, most importantly, the penetration of the gaseous reactant in the inner regions of the structure, so that only an effective control of all these processes yields the complete transformation of the template into the desired phase [88]. This control becomes more and more critical when large ceramic pieces are to be obtained, because diffusive phenomena are predominant and regulate the rate of phase transformation. Hence, the strict control of the reaction kinetic is the key feature needed: (i.) to activate the chemical reactions throughout the whole solid without inducing deformations and relevant structural defects, (ii.) to limit the grain growth, thus maintaining the multi-scale porosity, up to the nanosize, and (iii.) to obtain highly reactive inorganic precursors, in turn facilitating subsequent transformation reactions [87]. This complex and challenging chemical process has been used to produce the samples of sufficiently relevant dimensions for our mechanical experiments (and also for bone replacement applications).

In the following we present a systematic investigation of the mechanical properties of biomorphic apatite, which are found to be similar to the mechanical properties of both wood and bone, so that BA becomes promising for bone regeneration, in particular for load-bearing regions. A morphological investigation is reported, which shows that the porosity of BA displays a fractal nature of the lacunar type, a feature which may justify its excellent damage tolerance. In fact, the fractal characteristic of the porosity explains our experimental observation that the fracture is not abrupt and straight (as usual for ceramics), but evidences growth and tortuosity (as usual for bone). Results from an experimental campaign are presented, based on multiple mechanical tests: uniaxial compression (in both a standard configuration and *in-situ* inside a SEM), three-point bending, ring tests, and ultrasound evaluations. It is shown that biomorphic apatite performs better than standard hydroxyapatite [89, 90] ('HA' in the following) in several mechanical characteristics: elastic stiffness, strength, damage tolerance before failure and related toughness. Moreover, differently from HA and similarly to wood and bone, BA is found to exhibit a strength in tension often superior to that in compression, to evidence a transversely isotropic behaviour, which permits optimization of stiffness in the direction of loading, a feature particularly useful for bone replacement.

Our experiments allow the placement of biomorphic apatite in the Ashby charts, in terms of Young modulus vs strength or vs porosity, Fig. 2.1.

---

[2] The drawback becomes particularly evident when the material's functionality is related to the presence of nanocrystalline, non-stoichiometric or metastable phases, which can be easily degraded by high energy processes. Moreover, sintering processes destroy the surface chemistry, reducing the biocompatibility of materials.

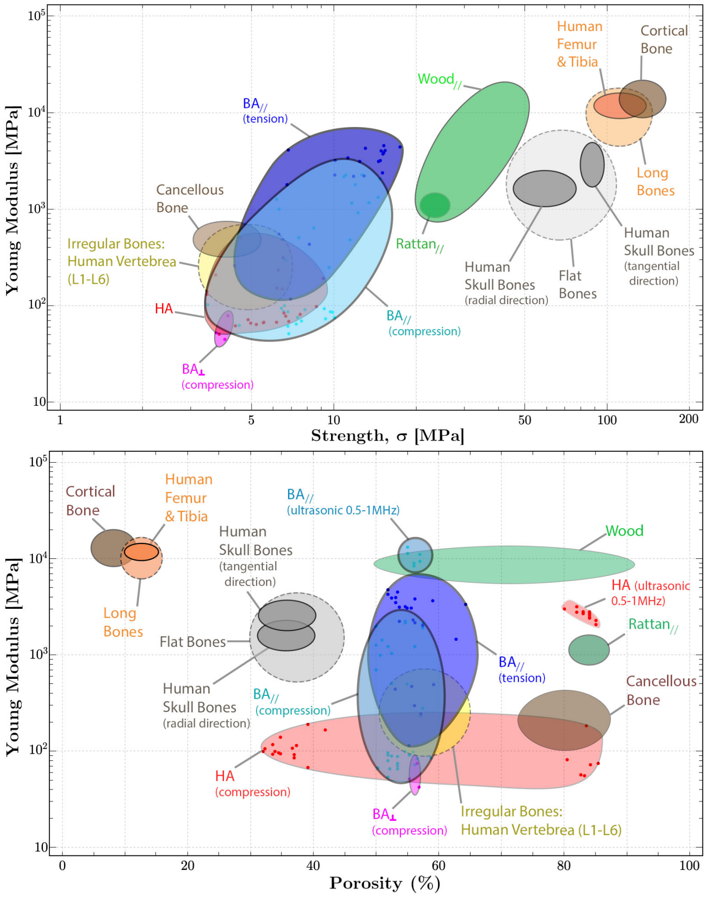

FIGURE 2.1: Ashby charts reporting Young modulus vs strength (upper part) and vs porosity (lower part) for biomorphic apatite, loaded parallel ($BA_{//}$) and perpendicular ($BA_{\perp}$) to the micro-tubule structure ('grain' in the following), for rattan wood (from which BA was obtained), and bones.

The Ashby charts reveal that BA occupies a virgin zone for ceramics and displays a similarity to the ligneous material from which it was 'born' and to several different bones, which evidences that the material is particularly suited for several biotechnologies.

It has to be finally mentioned that the results reported in here indicate that outstanding mechanical properties could be obtained for materials different from BA, but obtained with a process similar to that employed for BA, which can therefore be used as a guide for the fabrication of a new generation of inorganic materials with significant improvement in structural performance. This perspective is encouraged by previous results obtained with the chemical transformation of natural woods into various oxide (for instance Al2O3, ZrO2, TiO2, MnO) [91–95], and non-oxide (for instance SiC, TiC, ZrC) [4, 96–98] ceramics, which are particularly relevant for structural applications.

2.2 The lacunar fractal nature of porosity

Nano-twinned hydroxyapatite lamellae are a unique nanostructure characterising BA [86] and form a complex multi-scale porosity, where large pores (approximately 300 μm in diameter) are surrounded by medium-size pores (up to 50 μm in diameter), and coexist with a distributed fine porosity (1 μm of diameter), see a SEM image in Fig.2.2. The fine porosity is alveolar and closed, while the large and medium size porosity is two-dimensional, so that longitudinal channels are present, closely resembling the structure of the wood from which the material was indeed originated.

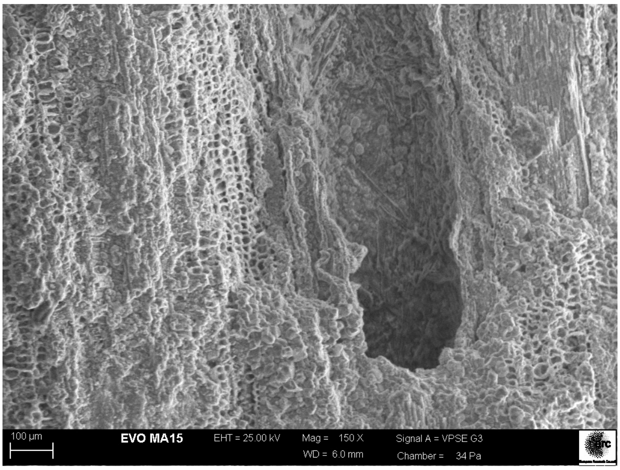

FIGURE 2.2: SEM image of the microstructure of biomorphic apatite showing long open channels surrounded by finer alveolar closed pores.

In order to show that the porosity of BA possesses a lacunar fractal nature [99, 100], images of microstructures captured within a SEM at different magnifications (38×, 100×, and 250×, in all cases employing a variable pressure inside the SEM chamber in the $20 - 25$MPa range) have been analysed with an image recognition program *ad hoc* developed in MATLAB to filter the grayscale SEM images and transform them into binary data (depicted in yellow or blue in Fig. 2.3). This program allowed a fast computation of the apparent porosity of the material based on the ratio between the number of blue pixels over the total number of pixels. As usually occurs with real images, an intensity threshold of grey (a parameter ranging between 0 and 255) has to be introduced to filter the data and transform the grey scale image into black and white. Therefore, the curves in Fig. 2.4 show the evolution of the apparent porosity vs. the filter index, which is defined as the ratio between the above intensity threshold and the value 255, for the three SEM images acquired at different magnifications. The porosity is clearly resolution-dependent, being an increasing function of the magnification. Such a resolution-dependency reveals a lacunar fractal nature for BA. For a rigorous quantification, the box-counting method has been applied to compute the local fractal dimension of the lacunar domain D. For each box of lateral size r, the number N of boxes containing at least one black pixel is counted. This operation is repeated at varying r from 1 up to 512 lateral size divisions, with a geometric progression of 2. From the $N(r)$ relation, the local fractal dimension D of the porous material has been finally obtained by differentiating $\log N$ with respect to $\log r$, thus obtaining

$$D(r) = -\frac{\mathrm{d}(\log N)}{\mathrm{d}\log r}.$$

Results are presented in Fig. 2.5 where, for 500 computations equally sampled by varying the filter index between 0 and 0.3, the mean value of $D(r)$ (with their error bars, corresponding to $\pm s$, where s is the root mean square of the computed values) are plotted as a function of $\log r$. As expected, the local fractal dimension quantifying the effect of porosity is always below 2, which corresponds to a Euclidean surface, over the whole range of r.

The fact that the porosity of BA has a lacunar fractality has a deep influence on the fracture propagation and trajectory, which (as shown later) is not abrupt and straight, but displays a growth with load in tortuous patterns which are unusual for ceramics and similar to bone [101, 102].

2.3 Mechanical testings

Mechanical tests have been performed on 48 prismatic, 19 cylindrical samples and also on 17 hollows cylinders of BA and, for comparison, on 42 samples of two Engipore hydroxyapatites [87].

Before testing, the chemical composition of the specimens has been investigated, in order to assess the successful and complete transformation of rattan. This was verified through X-ray diffraction tests, one of which is presented in Fig. 2.6, showing that the composition of hydroxyapatite is accompanied by relatively small quantities (less than 5%) of $\beta - \mathrm{Ca}_3(\mathrm{PO}_4)_2$ (beta-tricalcium phosphate), represented by the black dots.

In the following a nomenclature borrowed from wood mechanics will be adopted for BA, namely, 'parallel or orthogonal to the grain' will denote alignment parallel or normal to the fibres (also denoting the direction of transverse isotropy) of the wood from which the ceramic was made.

Results of (i.) uniaxial compression tests, (ii.) three-point bending, and (iii.) ring tests, are summarized respectively for the two materials in Tables 2.1 and 2.2, where mean values and standard deviations are reported. Note that the tests (i.) and (ii.) have been performed following the standards [103, 104].

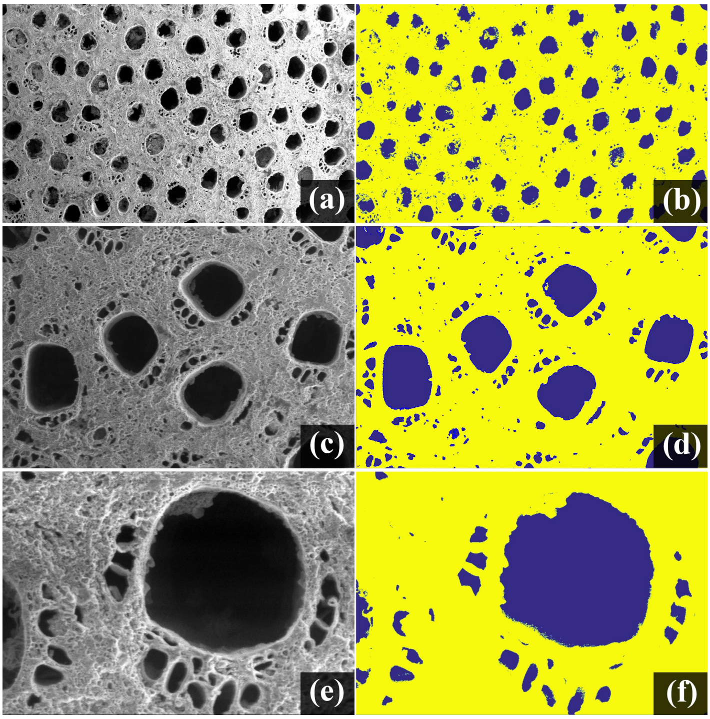

FIGURE 2.3: SEM images of cross sections biomorphic apatite, BA, and corresponding apparent porosity identified on the basis of the application of an *ad hoc* image analysis software with a filter index of 0.2. In particular: (a) 38× SEM image of BA; (b) At 38×, the porosity is detected to be 14.6%; (c) 100× SEM image of BA; (d) At 100×, the porosity is detected to be 19.0%; (e) 250× SEM image of BA; (f) At 250×, the porosity is detected to be 27.0%. The image correlation software shows that porosity is increasing with the magnification and this reveals the the lacunar fractality of the cross-section domain.

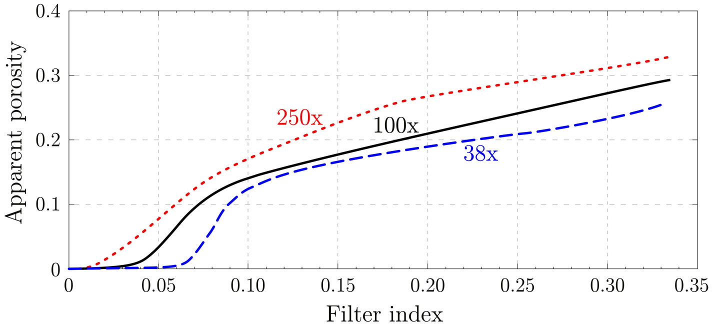

FIGURE 2.4: Increase of apparent porosity for BA with filter index at different magnification scales, showing the lacunar fractal nature of BA.

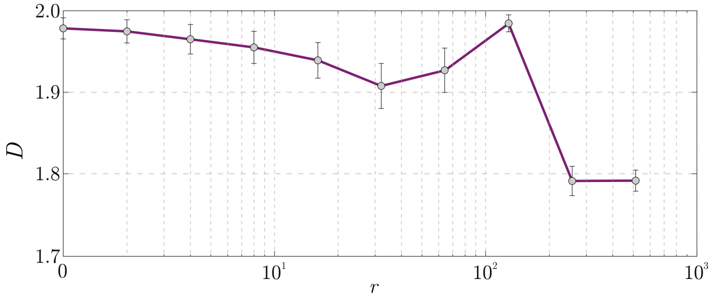

FIGURE 2.5: Local fractal dimension D (which quantifies the porosity) as a function of r (the lateral side division of the image in the box-counting algorithm).

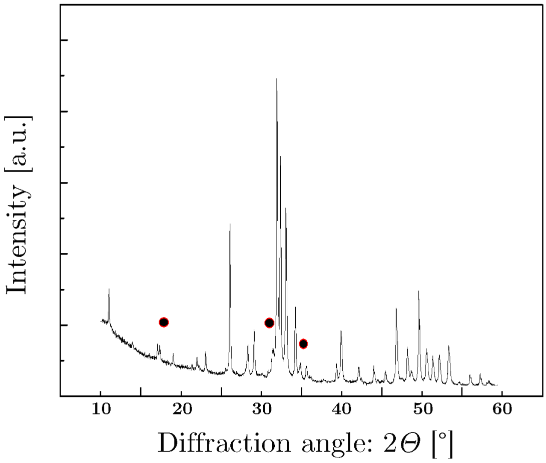

FIGURE 2.6: XRD pattern of one sample of BioApatite used for mechanical tests, where the dots point to reflections addressing the β-TCP phase. All the unmarked peaks point to HA phase.

Values of compression σ_c, and tension strengths σ_t, elastic modulus E (subscript 'c' in compression; subscript 'f' in flexure), are summarised in Tables 2.1 and 2.2.

Different stocks of ceramics (four for BA and two for HA) have been investigated; for BA these will be denoted with a number (#1, ... , #4) while for HA with HA1 and HA2. The samples have been *ad hoc* produced with different shapes, so as to allow for the execution of multiple mechanical tests. The mass density was varying for different stocks, so that the results presented in all Tables (except for Tables 2.8 and 2.10) and in all figures (except for Fig. 2.24), have been reported (with a linear proportion) to a same value of the mass density, $\rho_0 = 1.47$ g/cm^3, assumed as reference (as it was the most representative value for BA).

The possibility of using ultrasonic tests has also been analysed (on 6 samples taken from stocks #1and #2) to investigate the mechanical properties of BA on a scale much smaller than that explored through the other mechanical tests and typical of the cells forming bone tissues (osteoblasts).

An additional series of compressive tests were performed on prismatic samples inside a SEM, with different purposes: (i.) to assess the role of friction between the steel platens and BA prismatic specimens, (ii.) to document crack pattern evolution and sample exfoliation under uniaxial compression, and (iii.) to evaluate the effect of the eccentricity in the axial load, which can be caused in real applications by local imperfections in the specimen geometry and by inhomogenity of material's microstructure. In a first experiment, the BA specimen has been tested under uniaxial compression with steel platens in direct contact with the BA specimen, which leads to a contact problem with high friction. In a second experiment, a high density polyethylene layer has been interposed at the interface between specimen and steel platen, to reduce friction, while the opposite interface has been left with friction. Finally, a third experimental setup has been designed (through the interposition of paper board layers) to induce eccentric compression at low friction with the steel platens. Further evidence is provided in videos filmed during different tests (see Support electronic material).

	Uniaxial compression (‖)			Uniaxial compression (⊥)			3-point bending (‖)			Ring test (⊥)	3-point bending (⊥)	
	#1,2. 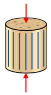	#3. 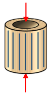	#4. 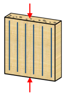		#4. 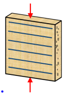		#1,2. 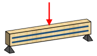	#4. 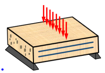		#3. 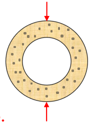	#4. 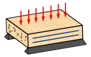	
Sample Set	$\sigma_{c\parallel}$ [MPa]	$E_{c\parallel}$ [MPa]	ρ/ρ_0 [−]	$\sigma_{c\perp}$ [MPa]	$E_{c\perp}$ [MPa]	ρ/ρ_0 [−]	$\sigma_{t\parallel}$ [MPa]	$E_{f\parallel}$ [MPa]	ρ/ρ_0 [−]	$\sigma_{t\perp}$ [MPa]	$E_{f\perp}$ [MPa]	ρ/ρ_0 [−]
# 1	6.5 ± 3.0	216 ± 99	0.95	–	–	–	8.7 ± 3.1	3426 ± 1448	0.83	–	–	–
# 2	7.7 ± 1.6	79 ± 13	1.01	–	–	–	13.8 ± 2.5	3342 ± 884	1.00	–	–	–
# 3	10.8 ± 2.9	1011 ± 448	1.06	–	–	–	–	–	–	6.0 ± 0.94	2851 ± 1152	1.1
# 4	12.3 ± 1.6	2201 ± 147	0.96	3.9 ± 0.1	59 ± 18	0.96	6.4 ± 1.5	359 ± 157	0.97	1.1 ± 0.6	8.0 ± 1.8	1.00

TABLE 2.1: Summary of the mechanical properties of the biomorphic apatite (BA), obtained from uniaxial compression, three-point bending, and compression ring tests on samples of different geometry (prismatic, cylindrical and tubular). All the mechanical properties are expressed in terms of their average ± the standard deviation: σ_c strength in compression, σ_t strength in tension, E_c Young modulus in compression, E_f Young modulus in flexure; index '‖' and '⊥' stand for parallel and orthogonal to the grains, respectively. Finally, ρ/ρ_0 is the ratio between the density and the reference density of 1.47 g/cm^3 to which all mechanical values have been reported.

Sample Set	Uniaxial compression			Three-point bending		
	σ_c [MPa]	E_c [MPa]	ρ/ρ_0 [−]	σ_t [MPa]	E_f [MPa]	ρ/ρ_0 [−]
HA 1	6.2 ± 2.5	239 ± 131	0.36	3.5 ± 0.6	3686 ± 1087	0.36
HA 2	5.6 ± 1.6	79 ± 23	1.41	5.7 ± 0.8	5235 ± 886	1.27

TABLE 2.2: Summary of the mechanical properties of commercial hydroxyapatite, obtained from uniaxial compression and three-point bending tests on prismatic samples. All the mechanical properties are expressed in terms of their average ± the standard deviation: σ_c strength in compression, σ_t strength in tension, E_c Young modulus in compression, E_f Young modulus in flexure; ρ/ρ_0 is the ratio between the density and the reference density of $1.47\ \mathrm{g/cm^3}$ to which all mechanical values have been reported.

Mechanical tests were conducted at the Instability Lab (University of Trento) with a Midi 10 and a Beta 100 electromechanical testing machines (Messphysik Materials Testing) used in different configurations for uniaxial compression tests, three-point bending, and ring tests (on hollow cylinders), which are detailed in this section. Additional in situ-compression tests were conducted with the tensile and compression stage DEBEN 5000S from GATAN, which is placed within the scanning electron microscope (SEM) EVO MA15 from Zeiss, both available in the MUSAM-Lab (the experimental laboratory of the Multi-scale Analysis of Materials Research Unit at the IMT School for Advanced Studies Lucca).

2.3.1 Uniaxial compression test

BA and HA prismatic and cylindrical samples and BA tubular samples have been tested under uniaxial compression. While HA is isotropic and does not show any orientation characteristic, BA is strongly anisotropic (due to its fibrous nature inherited from wood), so that compression has both applied parallel and orthogonal to the fibres (both tests have been performed only on prismatic samples, while cylindrical samples have been tested only parallelly to the fibres). The sample, in direct contact with two circular steel platens (40 mm in diameter and 5 mm thick), is compressed by imposing displacements to the upper platen. Figure 2.7 reports a sequence of photos taken during a typical uniaxial compression test on a BA cylindrical sample and related to the corresponding stress-strain curve (reported below). For comparison, in Figure 2.8, a uniaxial compression test on standard hydroxyapatite is reported, which abruptly fails as soon as a splitting crack (visible in the photo) is enucleated.

The photos show a progressive failure with continuing exfoliation for BA sample compressed parallel to the grain, in sharp contrast with the typically brittle failure displayed by HA, Fig. 2.8 and [105]. The exfoliation failure pattern is similar to that documented by Gei et al. [106] for silicon

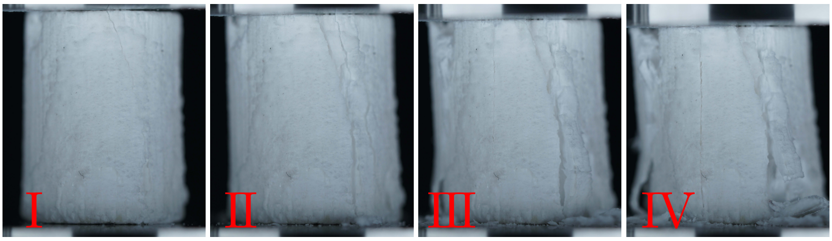

FIGURE 2.7: A sequence of photos taken during a uniaxial compression test of a cylindrical sample of BA. The instants when the photos have been taken are marked on the stress-strain curve (Fig. 2.9 on the left) reported in the the following. Note the progressive exfoliation of the sample, strongly enhancing toughness and related to the peaks in the stress-strain diagram.

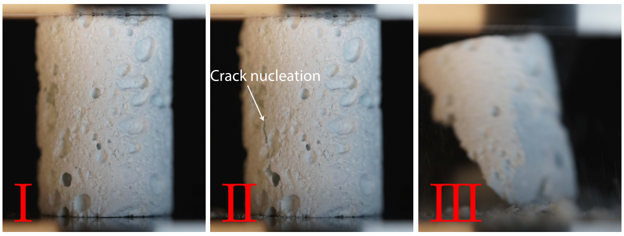

FIGURE 2.8: A sequence of photos taken during a uniaxial compression test of hydroxyapatite samples. The instants when the photos have been taken are marked on the stress-strain curve (Fig. 2.9 on the right) reported in the the following. Note the abrupt failure of the specimen immediately following the appearance of a splitting crack.

nitride at high temperature, but is now much more pronounced and yields a much more evident softening in the stress-strain curve, see Fig. 2.9, where a result for BA is reported (on the left) and contrasted with an analogous result for HA (on the right). Note that the stress-strain curves have been both reported to the reference density of 1.47 g/cm^3.

Note that the BA evidences a higher peak strength than HA, both occurring practically at the same strain level, but while HA is abruptly crushed at that strain, exfoliation takes place for BA, which continues to carry load and attains a final strain of more than 35%, thus displaying a great toughness for a ceramic.

Further results from compression tests parallel to the grain are reported in Table 2.3, for four different stocks of BA, each one characterised by different geometries and dimensions. Results are contrasted with the analogous for the two standard hydroxyapatites, also reported in the same Table.

It can be observed from Table 2.3 that the fibrous microstructure of BA implies that during compression parallel to the grain the sample is not in perfect contact with the loading platens, an effect which produces a pronounced scattering of experimental results and is detrimental to the measured strength. This effect is much less pronounced for HA samples, where

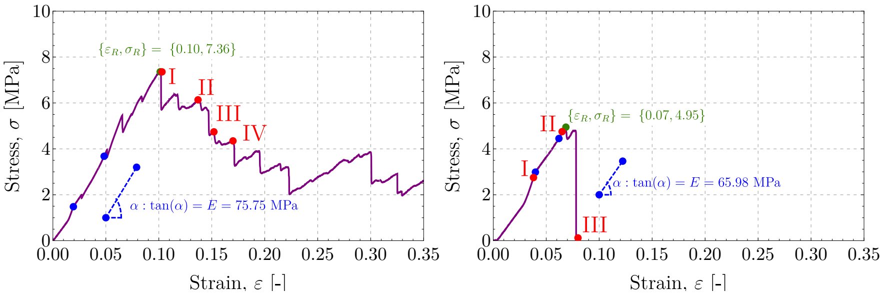

FIGURE 2.9: Stress-strain behaviour of a BA sample (#1, on the left) and of a HA sample (#1, on the right) subject to uniaxial compression, parallel to the grain for BA. The green spot identifies the peak strength, while a straight line drawn through the two indicated blue spots was used to evaluate the Young modulus $E = \tan \alpha$. The superior toughness of BA is evidenced by the slow load fall, contrasting with the sharp jump to zero displayed by HA.

Sample Set	Geometrical properties				Uniaxial compression test		
	ϕ [mm]	H [mm]	A [mm^2]	ρ [g/cm^3]	$\sigma_{c\parallel}$ [MPa]	$E_{c\parallel}$ [MPa]	ρ/ρ_0 [−]
# 1	14.30	19.89	160.62	1.39	6.5 ± 3.0	216 ± 99	0.95
# 2	15.21	19.83	181.62	1.49	7.7 ± 1.6	79 ± 13	1.01
# 3	29.35	31.13	511.29	1.56	10.8 ± 2.9	1011 ± 448	1.06
# 4	19.47	31.22	213.27	1.44	12.3 ± 3.2	2201 ± 147	0.96
HA 1	10.07	14.29	79.59	0.54	6.2 ± 2.5	239 ± 131	0.36
HA 2	10.03	14.75	79.05	2.07	5.6 ± 1.6	79 ± 23	1.41

TABLE 2.3: Mechanical characteristics from uniaxial compression tests on different stocks of BA and HA; compression is parallel to the grain for BA. On the left the averages of the geometrical properties of each stock are shown: ϕ is the main dimension of the samples' base (which corresponds to the outer diameter of samples #1, #2, #3, and to a side of prismatic samples #4); H the height; A the average cross-sectional area and ρ the average density. On the right the following average properties (± standard deviation) are reported (from left to right): compressive strength; Young modulus. Finally, ρ/ρ_0 is the ratio between the density and the reference density of 1.47 g/cm^3 to which all mechanical values have been reported.

parallelism and planarity of the surfaces can be better obtained than for BA.

Prismatic samples from stock BA #4 have been compressed orthogonally to the grain (i.e. normally to the weak plane), with the same experimental configuration used for the other compression tests. A sequence of photos during this compression is reported in Figure 2.10, showing the progressive formation of a set of inclined fractures, something that would be hardly visible for standard hydroxyapatite.

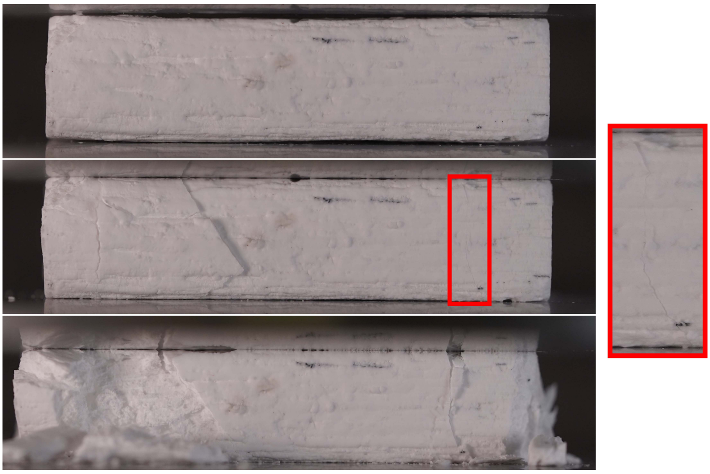

FIGURE 2.10: A sequence of photos showing progressive failure during uniaxial compression orthogonal to the grain of a BA prismatic sample (from set #4, geometrical and mechanical properties reported in Table 2.4).

In the direction orthogonal to the grain, BA is weaker than HA, as a consequence of the highly-oriented micro-structure of BA, providing strong transverse isotropy in strength and also in elastic stiffness. This can be observed from the stress-strain curve reported in Fig. 2.11, typical for compression orthogonal to the grain of BA prismatic samples. However, although strength and stiffness orthogonal to the grain are noticeably inferior to those measured parallel to the grain, BA still retains an excellent toughness.

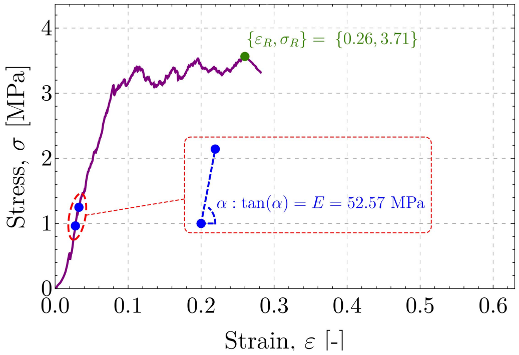

FIGURE 2.11: Stress-strain behaviour of a BA sample compressed parallel to the grain. The green spot identifies the peak strength, while a straight line drawn through the two indicated blue spots was used to evaluate the Young modulus $E = \tan\alpha$.

Compression orthogonal to the BA fibres was performed on prismatic samples only. In Table 2.4, the geometric properties of such samples are reported, along with the mechanical results of the tests.

Sample Set	Geometrical properties					Uniaxial compression test		
	B [mm]	H [mm]	S [mm]	A [mm^2]	ρ [g/cm^3]	$\sigma_{c\perp}$ [MPa]	$E_{c\perp}$ [MPa]	ρ/ρ_0 [−]
# 4	40.51	10.21	19.72	799.01	1.41	3.9 ± 0.1	59 ± 18	0.96

TAB. 2.4: Mechanical characteristics from uniaxial compression tests orthogonal to the grain. All samples are prismatic, with the following average dimensions: B width; H height; S depth; A cross-sectional area; ρ density. On the right, the following average properties (± standard deviation) are reported (from left to right): compressive strength; Young modulus. Finally, ρ/ρ_0 is the ratio between the density and the reference density of 1.47 g/cm^3 to which all mechanical values have been reported.

2.3.2 Three-point bending tests

Three-point bending tests have been carried out to evaluate the tensile stiffness and strength of BA and, for comparison, of HA. The tests have been performed by imposing the vertical displacements of a steel tip placed at the centreline of a prismatic sample, supported by two cylindrical elements placed at a distance L. The value of the stress σ, strain ε, and elastic Young modulus in tension E_f are determined respectively from the value of the applied load P and deflection at centreline v, and from a difference between two selected values of the load ΔP (measured during elastic response of the sample), together with the corresponding difference between midspan deflections Δv. The specimen is treated as a linear elastic beam [107], so that

$$\sigma = P \frac{L\,h}{8\,I}, \qquad \varepsilon = v \frac{6\,h}{L^2}, \qquad E_f = \frac{\Delta P}{\Delta v} \frac{L^3}{48\,I}, \tag{2.1}$$

where I is the moment of inertia of the cross section, L is the distance between the supports and h is the height of the cross-section.

Three-point bending test with tension parallel to the grain were carried out on BA samples and on HA samples for comparison, to evaluate the tensile elastic stiffness and strength in the direction parallel to the grain. A sequence of photos taken during a three-point bending test on BA is reported in Fig. 2.12, showing a feature rarely visible in a ceramic sample, namely, the growth of a tensile crack, something which cannot be observed in a HA sample and again demonstrating the superior damage tolerance of BA.

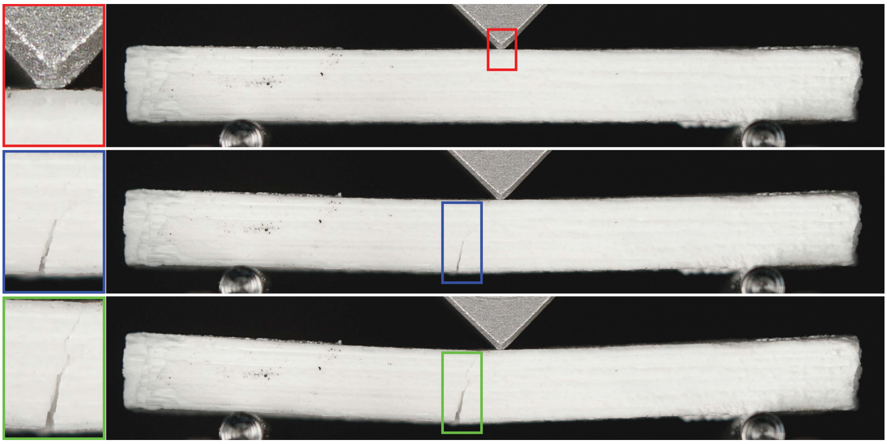

FIGURE 2.12: A sequence of photos taken during a three-point bending test on prismatic sample of biomorphic apatite (BA set # 1), tested in the direction parallel to the grain. The growth of a tensile fracture is clearly documented (see the insets marked blue and green; the inset marked red shows a detail of the loading blade).

A typical stress-strain curve obtained from a three-point bending test is shown in Fig. 2.13, on the left for BA (with tension parallel to the grain) and on the right for HA.

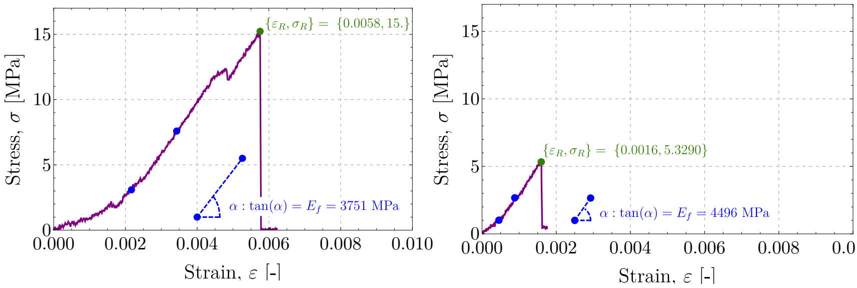

FIGURE 2.13: Tensile stress-strain behaviour of BA (Set #1, on the left) and of HA (Set # 2, on the right) from a three-point bending test, parallel to the grain for BA. The green spot identifies the peak strength, while a straight line drawn through the two indicated blue spots was used to evaluate the Young modulus $E = \tan\alpha$. The superior toughness of BA is highlighted by the failure strain much higher than in the HA sample.

Further results on mechanical properties measured in bending (with tension parallel to the grain for BA) for different stocks are presented (in terms of average stress and stiffness) in Table 2.5.

Sample Set	Geometrical properties				Three-point bending parallel to the grain		
	B [mm]	H [mm]	L [mm]	ρ [g/cm^3]	$\sigma_{t\parallel}$ [MPa]	$E_{f\parallel}$ [MPa]	ρ/ρ_0 [−]
# 1	11.04	5.72	37.33	1.22	8.7 ± 3.1	3426 ± 1448	0.83
# 2	9.94	5.21	35.00	1.47	13.8 ± 2.5	3341 ± 884	1.00
# 4	19.49	10.10	26.00	1.42	6.4 ± 1.5	359 ± 157	0.97
HA 1	10.03	5.11	40.00	0.53	3.5 ± 0.6	3686 ± 1087	0.36
HA 2	10.16	5.00	35.00	1.81	5.7 ± 0.8	5235 ± 886	1.27

TAB. 2.5: Mechanical characteristics from three-point bending tests on the different stocks of BA (with tension parallel to the grain) and HA. All the samples are prismatic, with the following average dimensions: B depth; H height; L length; ρ density. On the right the following average properties (± standard deviation) are reported (from left to right): tensile strength; Young modulus. Finally, ρ/ρ_0 is the ratio between the density and the reference density of 1.47 g/cm^3 to which all mechanical values have been reported.

Table 2.5 shows that the mechanical properties, in particular the elastic Young modulus of BA, are noticeably different from stock to stock. This effect can be related to the different aspect ratio (H/L) of the specimens, as this parameter influences the failure mechanism of the sample. In fact, stock #4 is characterised by an aspect ratio 2.5 times larger than that for the other stocks (BA #1, #2). Therefore, a shear mechanism of failure prevails, leading to underestimate the Young modulus.

Three-point bending test with tension orthogonal to the grain were carried out on BA samples, to evaluate the tensile stiffness and strength in that direction. A sequence of photos taken during a test is reported in Fig. 2.14, showing once more the growth of a tensile crack, again something rarely visible in ceramics and documenting the great toughness of BA.

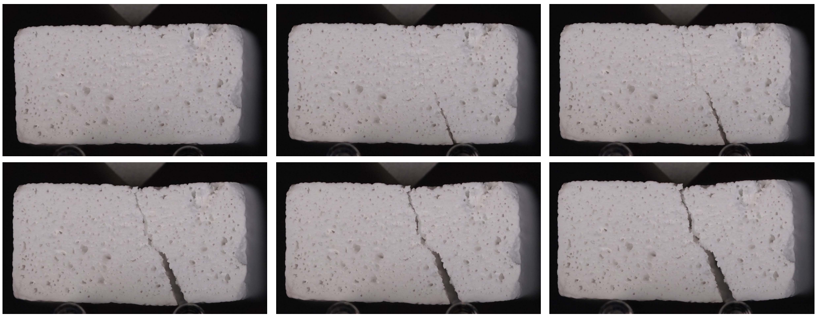

FIGURE 2.14: A sequence of photos taken during a three-point bending test on biomorphic apatite prismatic samples (Set #4) tested in the direction orthogonal to the grain. Note the growth of a tensile fracture.

A typical stress-strain curve obtained from a three-point bending test for tensile stress orthogonal to the grain is shown in Fig. 2.15.

Further results on mechanical properties measured in bending with tensile stress orthogonal to the grain are presented (in terms of average stress and stiffness) in Table 2.6.

Table 2.6 shows that the mechanical properties of BA, evaluated orthogonally to the grain, in particular the elastic Young modulus, are significantly lower than the same properties evaluated in the direction parallel to the grain. The fact that the measured values are much smaller than those referred to tests parallel to the grain (and also are smaller than the values obtained with the ring test presented in the next section) is related to the dimensions of the samples, which are too thick to be represented as beams, so that for example, the failure shown in Fig. 2.14 is more related to the shear force applied by one support than to flexure.

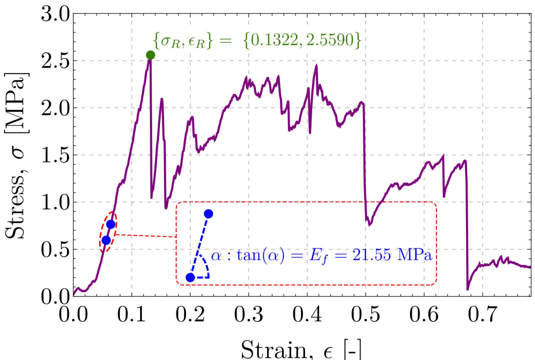

FIGURE 2.15: Tensile stress-strain behaviour of BA (Set #4) from a three-point bending test, with tensile stress parallel to the grain. The green spot identifies the peak strength, while a straight line drawn through the two indicated blue spots was used to evaluate the Young modulus $E = \tan\alpha$. The high toughness of BA is highlighted by the slow load fall.

Sample Set	Geometrical properties				Three-point bending orthogonal to the grain		
	B [mm]	H [mm]	L [mm]	ρ [g/cm^3]	$\sigma_{t\perp}$ [MPa]	$E_{f\perp}$ [MPa]	ρ/ρ_0 [−]
# 4	37.00	10.13	12.07	1.44	1.9 ± 1.2	11 ± 7	0.98

TAB. 2.6: Mechanical characteristics from three-point bending tests with tension orthogonal to the grain. All the samples are prismatic, with the following average dimensions: B depth; H height; L length; ρ density. On the right the following average properties (± standard deviation) are reported (from left to right): tensile strength; Young modulus. Finally, ρ/ρ_0 is the ratio between the density and the reference density of 1.47 g/cm^3 to which all mechanical values have been reported.

2.3.3 Ring tests

The ring test is performed on tubular samples which are compressed along the diametral direction until failure occurs. This set-up is similar to the so-called 'Brazilian test', except that the samples for the latter test are solid cylinders. Both tests are used to investigate the tensile mechanical properties of brittle materials. Consistently, the ring test has been thoroughly used for rocks as these materials are brittle (as ceramics), so that the tensile properties can be inferred from a compressive experimental set-up.

Many works [108–111] have shown that the tensile strength of a linear elastic - perfectly brittle material evaluated in the ring test is a function of the ratio between the internal and external radii $\bar{r}$. Nonetheless, for values of $\bar{r}$ larger than 0.3, Hudson [112] proved that the evaluated tensile strength tends to become a constant quantity, in other words, the strength results unaffected by such ratio. Furthermore, Srinath [113] demonstrated that the beam theory [107] is effective in the evaluation of the tensile strength of ring specimen for values of $\bar{r}$ ranging between 0.6 and 1, in other words, when the ring thickness is very small. Since in our study $\bar{r} = 0.512 \pm 0.009$, the stress-strain relation σ/ϵ has been obtained via:

$$\sigma = P\,\frac{h\,R}{2\pi\,I}, \quad \varepsilon = v\,\frac{8\,h}{(\pi^2 - 8)R^2}, \tag{2.2}$$

where v is the vertical displacement of the steel plate applying the force P to the specimen, R is the average between external and internal radii, and finally h is the thickness of the cylinder wall and I its moment of inertia, respectively.

It should be noted that the ring tests are loading the sample in the 'weak' direction, orthogonal to the grain, so that these tests are particularly suited to reveal the less stiff and less resistant behaviour of the material.

A sequence of photos taken during the testing of BA is reported in Fig. 2.16, showing initially the growth of two vertical tensile cracks and later of two horizontal tensile cracks, terminating the load carrying capacity of the specimen. This growth of a tensile fracture, as already observed for three-point bending tests is unusual for ceramic materials, which usually display a sudden failure.

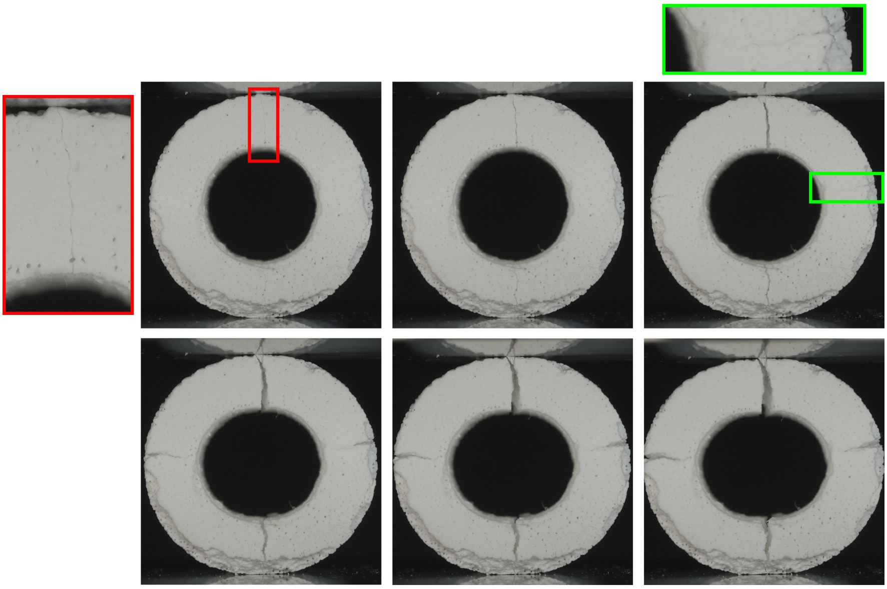

FIGURE 2.16: A sequence of photos taken during a ring compression test on biomorphic apatite, BA, tubular samples (Set #3) tested in the direction orthogonal to the grain. The growth of tensile fractures is clearly documented (see the insets).

A typical stress-strain curve obtained from a ring test (tensile stresses are orthogonal to the grain) is shown in Fig. 2.17.

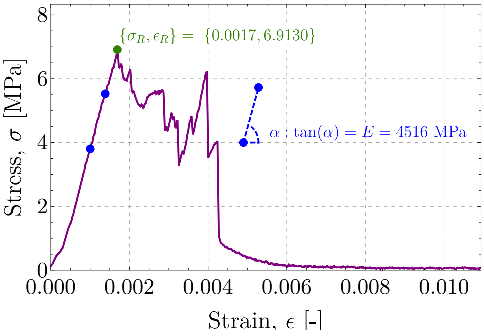

FIGURE 2.17: Tensile stress-strain behaviour of BA (Set #3) from a ring compression test test, with tensile stress parallel to the grain. The green spot identifies the peak strength, while a straight line drawn through the two indicated blue spots was used to evaluate the Young modulus $E = \tan \alpha$. The high toughness of BA is highlighted by the slow load fall.

Further results of the mechanical tests are shown in Table 2.7, together with the geometrical properties of the samples.

Sample Set	Geometrical properties				Ring test		
	H [mm]	r_o [mm]	r_i [mm]	ρ [g/cm^3]	$\sigma_{t,\perp}$ [MPa]	$E_{f,\perp}$ [MPa]	ρ/ρ_0 [$-$]
# 3	30.85	12.79	6.54	1.572	6.0 ± 0.94	2851 ± 1152	1.1

TAB. 2.7: Mechanical characteristics from ring tests on BA samples (tensile stresses are orthogonal to the grain). All the samples are tubular, with the following average dimensions: H depth; r_o outer radius; r_i internal radius, and ρ density. On the right the following average properties (± standard deviation) are reported (from left to right): tensile strength; Young modulus. Finally, ρ/ρ_0 is the ratio between the density and the reference density of 1.47 g/cm^3 to which all mechanical values have been reported.

The results reported in the Table report good values of strength for biomorphic apatite subject to tension orthogonal to the grain, values better than those obtained from three-point bending. Figure 2.17, displays an interesting feature, namely, a double peak in the stress-strain curve, which shows that the maximum tensile strength is achieved twice: the first time at the first vertical cracking and a second time at the formation of the horizontal crack. Before cracking the sample is a ring loaded with two opposite concentrated forces, but after the first crack has formed, the static scheme changes to an arch loaded with two opposite forces acting on its springer points. This new configuration reminds that of the Half ring test [114], where the tensile strength of the specimen is obtained by using the Beer's formulation of a prismatic circular arch.

2.3.4 Ultrasonic tests

The multi-scale structure of biomorphic apatite requires a mechanical characterisation of both macro-scale, for load-bearing applications, and nanoscale, for the interaction of biomorphic apatite with bone cells. Therefore, in addition to the mechanical tests performed at the scale of the sample, ultrasonic measurements were taken at high wavelength in an attempt to characterize the elastic properties of the material at a micro scale. P-waves were used (generated and recorded with a pressure wave transducer, Olympus A102S, frequency 1 and 0.5 MHz, connected to an ultrasonic square wave pulser/receiver unit, Olympus 5077PR, combined with a NI PCI-5152 Digitizer/Oscilloscope). The tests were performed by measuring the time t_v needed for P-waves to travel along the height H of the sample and reach a sensor, so that the velocity of the wave is given by $v_p = H/t_v$ which, for an isotropic elastic material, is linked to the Lamé constants through:

$$v_p = \sqrt{\frac{\lambda + 2\mu}{\rho}}, \tag{2.3}$$

so that the elastic modulus E may be evaluated, once the Poisson's ratio ν is known, from the equation

$$E = \frac{(\lambda + 2\mu)(1+\nu)(1-2\nu)}{1-\nu}. \tag{2.4}$$

The result of two typical ultrasonic tests on BA (right) and HA (left) is shown in Fig. 2.18 at two different frequencies (0.5 and 1.0 MHz), in terms of signal amplitude ('Amp') versus time. Note that the points which have been identified as representative of the time of flight t_v have been identified in agreement with the standards [115], so that the arrival of the P-wave has been marked at the instant when the leading edge of the first peak was reached at 80% (the evaluation was done automatically using a Mathematica routine *ad hoc* developed).

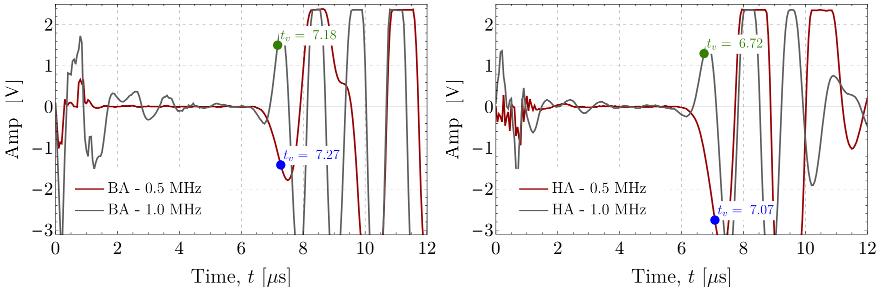

FIGURE 2.18: Amplitued of the signal versus time for two ultrasonic tests on a BA sample (Set #1, on the left) and on a HA sample (Set #1, on the right) at two different frequencies (0.5 and 1.0 MHz)

Mechanical properties derived from ultrasonic tests (parallel to the grain) are reported in Table 2.8, in terms of mean values of uniaxial strain elastic modulus $\lambda + 2\mu$ and Young modulus E, the latter evaluated for two extreme values of Poisson's ratio ν. Note that the data collected in the Table have not been reported to the reference density, because in an ultrasonic test the measurements are believed to be referred to the skeleton material.

Set	Geometrical properties				Ultrasonic test			
	H [mm]	ϕ [mm]	A [mm^2]	ρ [g/cm^3]	v_p [m/s]	$\lambda + 2\mu$ [MPa]	E [MPa] $\nu = 0$	$\nu = 0.25$
# 1,2	20.84	14.19	158.08	1.42	2723 ± 212	10398 ± 1661	10398 ± 1661	8665 ± 1384
HA 1,2	15.01	10.07	79.61	0.54	2191 ± 72	2583 ± 290	2583 ± 290	2152 ± 241

TAB. 2.8: Mechanical characteristics from ultrasonic tests on BA samples (parallel to the grain) and HA. All the samples are cylindrical, with the following average dimensions: H height; ϕ diameter; A cross-sectional area; ρ density. On the right the following average properties (± standard deviation) are reported (from left to right): wave velocity; uniaxial strain elastic modulus; Young modulus for two different values of Poisson's ratio. All reported values have not been normalised to the reference density.

It is worth mentioning that knowing the frequencies of the applied P-wave and its speed allows to check the wave length of the applied exciting pulse as:

$$\lambda_p = \frac{v_p}{f_p} \approx \frac{2500\ \mathrm{m/s}}{10^6\ \mathrm{Hz}} = 2.5\ \mathrm{mm}, \tag{2.5}$$

which is greater than the typical dimensions of osteoblasts (on the order of 20 ¯m), so that the elasticity detected with the ultrasound tests is not believed to be representative of the scale of a single cell, but may still be acceptable to characterize the biological response of the material, because these osteoblasts tend to interact with bone in large groups rather than individually.

2.3.5 In situ mechanical tests and further analysis of crack patterns

A series of compression tests were performed using a micromechanical compressive stage placed inside a SEM (Zeiss EVO MA15 equipped with the DEBEN5000S tensile/compressive stage) with the purpose of analyzing the effects of boundary conditions on the samples and the fracture paths typical of BA.

Compression is applied under displacement control with a gearbox speed of 0.1 mm/minute, to achieve quasi-static conditions. The equipment has a 10 mm linear extensometer for position readout, with 300 nm resolution.

The combined use of the stage and the SEM allows inspecting the evolution of crack pattern and the role of the material microstructure during the application of the axial displacement. Three BA prismatic specimens, whose geometrical data are collected in Table 2.9, were tested under different boundary conditions in order to assess the sensitivity of the material response and of the fracture pattern upon variations from a reference testing configuration characterised by uniaxial compression with steel platens in direct contact with the specimen (where friction is present at the interface between steel and BA).

Loading Condition	Geometrical properties				
	H [mm]	w [mm]	t [mm]	ρ/ρ_0 [$-$]	p (%)
Uniax. Comp. (high friction)	31.47	20.52	10.11	0.91	57.29
Uniax. Comp. (low friction)	31.29	21.29	10.53	0.93	56.21
Eccentric Compression	31.55	21.46	10.22	0.95	55.83

TAB. 2.9: Geometrical properties for the BA specimens tested *in situ* with a SEM and subject to different loading conditions. H is the height of the sample, w the width, t the thickness. ρ/ρ_0 is the ratio between the density and the reference density of 1.47 $\mathrm{g/cm^3}$ and p is the porosity

In the first test, the BA specimen is inserted between the steel platens without introducing measures to reduce friction and is loaded under uniaxial compression. The overall stress-strain mechanical response is represented by the red curve in Fig. 2.19, labelled as 'high friction'. The progress of the crack pattern inspected by SEM imaging shows the appearance of cracks predominantly aligned with the axial direction, parallel to the grain, Fig. 2.20. The stress-strain curve shows a peak stress of 9 MPa, corresponding to first cracking, followed by a plateau and a progressive hardening continuing up to $\sigma \approx 10 - 11$ MPa and a significant toughness at failure, so that the failure strain is $\epsilon \approx 0.05$. The failure strength observed from the test is consistent with that obtained on similar specimens using the Messphysik Materials Testing, reporting $\sigma \approx 12.3$ MPa (Table 1, first column, row #4).

In the second test, a high density polyethylene layer (visible in Fig. 21) is inserted at the contact between one of the BA bases and the steel platen, so that friction is reduced on one base, but not on the opposite base. The overall stress-strain curve is shown by the blue curve in Fig. 2.19, labelled as 'low friction'. The perturbed boundary conditions have not significantly modified the values of the failure strength and of the corresponding deformation, when compared to the 'high friction' case. However, the crack pattern leading to failure was found substantially different, with the appearance of a major exfoliating crack perpendicular to the grain direction and

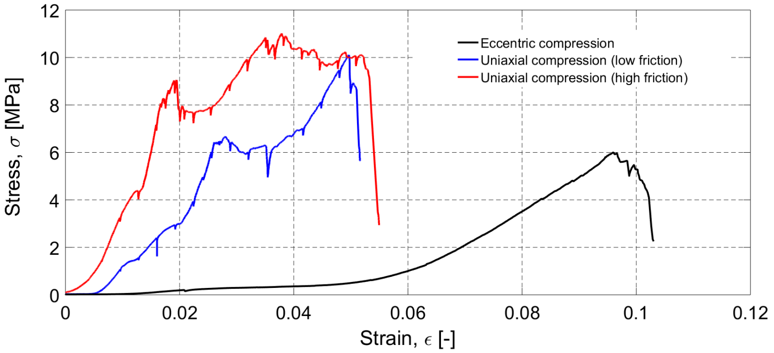

FIGURE 2.19: stress-strain curve of BA specimens tested in situ with a SEM under uniaxial compression at two levels of friction (at the specimen/platens contacts) and for eccentric loading.

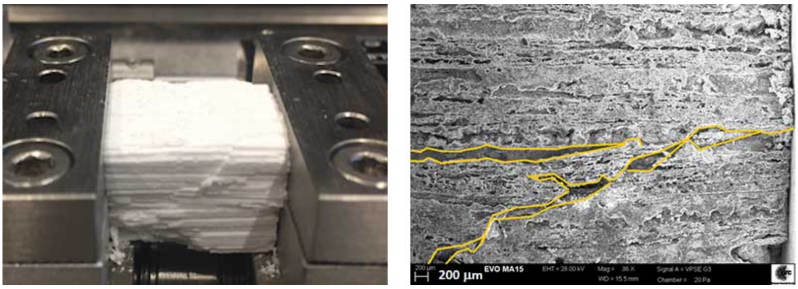

FIGURE 2.20: Specimen tested under uniaxial compression with high friction. On the left: view of the specimen at failure; on the right: cracks at failure.

clearly visible on the specimen surface (Fig. 2.21). Inspection of the specimen after failure showed also the existence of many cracks aligned parallel to the grain direction, again as observed in the 'high friction' case.

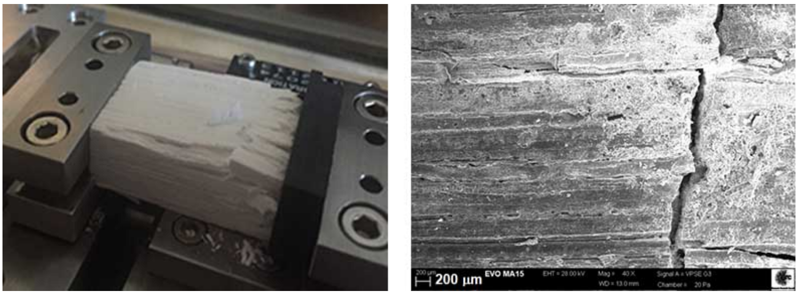

FIGURE 2.21: Specimen tested under uniaxial compression in side the SEM in conditions of low friction. On the left: view of the specimen at failure (note the high density polyethylene layer of black colour); on the right: cracks at failure.

In the third test, the BA specimen was inserted with paperboard layers at both its bases to reduce friction on both sides. Moreover, the loading platens were modified with the purpose of inducing an eccentricity $e = h/4$ (h is the specimen height) in the compression load N. This testing condition leads to a linear variation of the stress σ orthogonal to the cross-section of the specimen (and thus parallel to the grain):

$$\sigma = \frac{N}{A} + \frac{Ne}{bh^3/12}y, \tag{2.6}$$

where A is the cross-section area of the specimen, b its width, and y picks up the position along the cross-section. At the extrados, $y = -h/2$, which corresponds to the upper side of the BA specimen observed in the SEM, the axial stress reaches its maximum positive value, corresponding to a tensile stress, while at the opposite side compression prevails. This stress state leads to a very peculiar failure mode, where exfoliation of a thick layer of BA parallel to the grain takes place, followed by the final failure by transverse cracking on the side subject to tension, see Fig.2.22. The corresponding stress-strain curve represents the evolution of the tensile stress at the extrados, is reported with a black line in Fig.2.19, labelled as 'eccentric compression'. The failure strength (parallel to the grain) approaches 6 MPa in tension, which is consistent with data reported in Table 2.9 obtained from three-point bending tests.

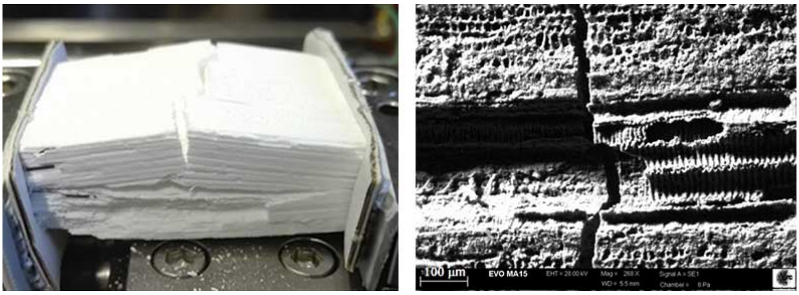

FIGURE 2.22: BA specimen tested under eccentric compression in situ with a SEM and shown at failure on the left (note the paperboard layers in contact with the sample); cracks at failure are detailed on the right.

2.4 Biomorphic apatite vs. wood and bone: the Ashby plot

The mechanical behaviour of BA is now compared with that of its parent material, Rattan wood, used to produce the BA, and with that of human bones. Tests have been conducted on rattan wood, taken from a plant belonging to the subfamily of Calamoideae, which mechanical properties have been investigated through compression and three-point bending experiments (performed following the standards [116–119]), with the same configurations used for ceramics. A series of photos taken during a typical compression test are shown in Fig. 2.23 and the relative stress-strain curve is shown in Fig. 2.24 on the left, while the same figure presents a tensile stress-strain curve obtained from a three-point-bending test on the right.

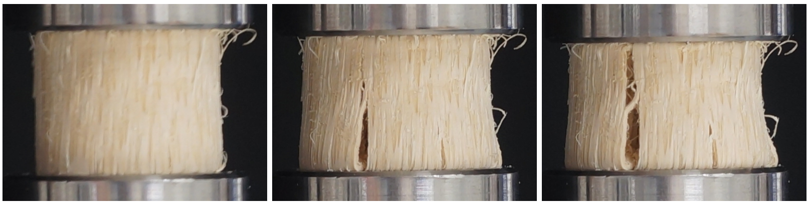

FIGURE 2.23: A sequence of photos showing progressive failure (involving exfoliation by fibre buckling) of a rattan wood specimen during uniaxial compression.

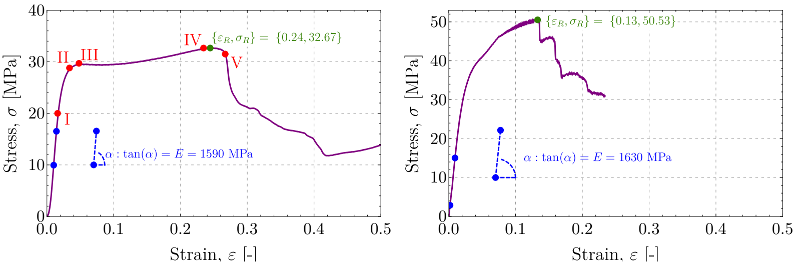

FIGURE 2.24: stress-strain behaviour of a rattan wood sample subject to uniaxial compression (on the left) and three-point bending (on the right), parallel to the grain. The red spots (in the compression plot) identify different stress levels corresponding to different definitions of failure. A straight line drawn through the two indicated blue spots was used to evaluate the Young modulus $E = \tan \alpha$.

Further results from the mechanical compression and three-point bending tests on rattan wood (with the stress always aligned parallel to the grain) are shown in Table 2.10, together with the geometrical properties of the samples.

Fig. 2.23 shows a failure process characterised by exfoliation by buckling, a long process highlighting the outstanding resistance of the material, while Fig. 2.24 shows a flat post-elastic regime, characterised by large deformations. In rattan wood, failure may take different definitions, so that it can be identified with the first load corresponding to visible local buckling of the fibres (I), or to maximum curvature in the diagram (II), or with the beginning of the plateau (III) or with the peak (IV) in the curve, or, finally, (V) with the beginning of softening. Therefore, when failure is identified with the first appearance of local buckling of fibres its strength in compression becomes lower than that in tension. It can be concluded that the behaviour

Tests	Geometrical properties			Mechanical parameters	
	H^a, L^b [mm]	ϕ [mm]	ρ [g/cm^3]	σ [MPa]	E [MPa]
Compression[a]	29.18	21.90	0.46	23.7 ± 2.7	1326 ± 164
3-Point Bending[b]	240	19.87	0.46	50.0 ± 11.8	2127 ± 415

TAB. 2.10: Mechanical characteristics from uniaxial compression tests and three-point bending (in both cases stress is parallel to the grain) on rattan wood. All the samples are prismatic, with the following average dimensions: H height; L span; ϕ base dimension; ρ density. On the right the following average properties (± standard deviation) are reported (from left to right): compressive strength; Young Modulus.

of rattan wood has several points in common with that of its derived material, BA.

Bones are highly-hierarchical composite materials, so that their mechanical behaviour is controlled by its two main constituents: cancellous bone (soft and deformable) and cortical bone (stiff and strong). Both of these materials are transversally isotropic [120–122] and with stiffness and strength different in tension and in compression [120–122], see also [123]. Overall, the mechanical behaviour of bone is also affected by the amount of cancellous vs. cortical bone, so that for flat, long and irregular bones the mechanical properties are unique and different from one another [122, 124–126].

The Ashby charts expressed in terms of Young Modulus vs. Strength and Young Modulus vs. porosity for biomorphic apatite, loaded parallel ($\mathrm{BA}_{//}$) and perpendicular ($\mathrm{BA}_{\perp}$) to the grain, for the rattan wood used to produce the BA (parallel to the grain) and bones (data from the above-mentioned literature) are shown in Fig. 2.1.

The Ashby charts show that BA is occupying a region usually not covered by ceramics, moreover, the Young modulus is fully compatible with values typical of wood and bone (particularly flat bone). If, on the one hand, the strength of BA is smaller than that of bone and wood, on the other hand, it is much higher than that of the hydroxyapatite usually used for bone replacement. These considerations, in addition to the fact that porosity and hierarchical structure of BA are similar to those of wood and bone, suggest that BA is a ceramic with outstanding mechanical characteristics, particularly suited for bone replacement and biological applications.

2.5 Conclusions

Biomorphic apatite, a ceramic obtained through a biomorphic transformation process from rattan wood, presents a nano and micro structure which retains elements inherited from its parent material, the ligneous essence.

This structure has been shown to generate a lacunar fractal porosity, which yields the outstanding mechanical properties that we have measured for biomorphic apatite. In particular, biomorphic apatite shows a damage and defect tolerance, a strength and elastic stiffness superior to its competitor material, a porous sintered hydroxyapatite, but also to other biomorphic hydroxyapatite obtained from different type of woods, that are present in the literature [6, 7, 92]. Moreover, biomorphic apatite is transversely isotropic, so that it can be effectively employed in all the situations (such as for instance as bone replacement) where the ceramic piece is subject to a load having a privileged direction. The fact that biomorphic apatite is produced without sintering and its superior mechanical performance suggest use of this material for several challenging biotechnologies.

3

Failure of porous ceramics via phase-field modelling

3.1 Introduction

Theoretical considerations [14–19, 127, 128] and experiments [20, 129, 130] show that the trajectory of a fracture growing in a material is strongly influenced by the presence of inhomogeneities. Crack deviations from rectilinearity usually enhance toughness [21, 22, 131] and an isolated crack can even be stopped, when it hits a hole with smooth boundary (a feature also visible in the experiments reported here later Figs. 3.2). The phase-field approach to fracture has been developed as an energy minimization, via Γ-convergence regularization of free discontinuities modelling cracks [132–139]. This approach has been advocated as capable of overcoming problems related to complex trajectory topologies [140, 141] , an assertion which is confirmed through careful experimental evaluation in the first part of this chapter. In particular, simulations performed with our implementation of the model developed in [141] are compared to experiments, referred to photoelastic PMMA plates, containing notches and circular holes, where the crack trajectory strongly deviates from rectilinearity and terminates against the void. Therefore, the first conclusion reached in this chapter is the validity of the phase-field technique to describe crack trajectories. This conclusion provides a firm experimental basis to several studies dedicated to the numerical simulation of crack propagation via phase-field in brittle materials [140–148].

Starting from section 3.4 we address materials characterised by a high-density distribution of multiscale voids and later show that the phase-field approach can also be successfully applied to brittle porous materials. These materials are diffused in nature (for instance bone, rock –sandstone, tuff, pumice–, coal) and as man-made materials (for instance concrete, cellular ceramics, and porous carbide). Crucial uses of porous ceramics are in the scaffolds and bone repair technologies. In this field, a 3-D porous apatite (called ‘BioApatite’, BA in the following) has recently been obtained

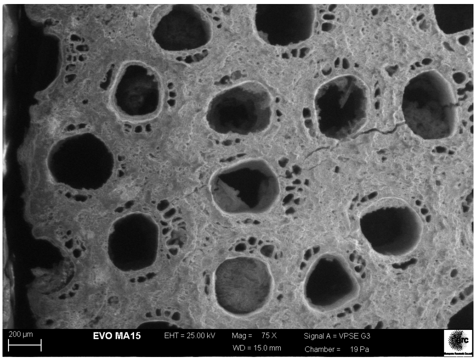

FIGURE 3.1: SEM image of a BA sample undergoing an uniaxial compression test. A crack nucleates at the external surface of a void, where a tensile stress locally develops, although the mean stress in the sample is compressive. Note also the porosity at macro and meso levels.

through biomorphic transformation of natural wood [87] , Fig. 3.1. BA replicates the multiscale hierarchical structure of wood, which mimics bone and thus becomes an ideal candidate for biomechanical applications. From a mechanical perspective, BA displays outstanding properties [13, 149] , which are one of the important factors for structural applications, typically, in bone repair, where a correct failure analysis may lead to care and time prediction for rehabilitation.

In brittle materials, such as glass or ceramics, fracture nucleation primarily occurs under tensile stresses, but in the case of a porous material it may occur, and sometimes be even common (for instance as bone repair applications), for compressive loads, as shown in Fig. 3.1. In the figure a crack is visible, nucleating from the surface of a pore where the local stress is tensile, although the mean stress applied to the whole sample is compressive [24–26] [1]. The mechanical modelling of porous-brittle solids is primarily based on the void volume fraction (the average volume of voids per unit volume), which may be used as a simple parameter to determine the mechanical characteristics of a porous material [28–31] . With the knowledge of this parameter, the *minimal solid area method* (MSA) allows for a simple determination of the elastic stiffness of the material and of the peak strength [30] . This methodology, compared with the more sophisticate *stress concentration effect method* [32, 33] , leads to the conclusion that pore shape has less influence than pore size on the global mechanical behaviour. However, multiscale porosity has been only scarcely analyzed so far [34] , so that the phase-field approach will be shown to be successfully applicable to porous brittle material with multiscale porosity.

---

[1] Considering any sample of a material with a generic distribution of internal voids, and subject to compressive tractions on the external surface, the mean stress theorem [27] leads to the conclusion that the mean stress internal to the sample is compressive.

To summarize, chapter 3 is structured as follows: after the phase field model is introduced (Section 3.2), the approach is validated in Section 3.3 against a series of photoelastic tests of samples containing notches and circular holes. For porous brittle materials, the phase field model is calibrated in Section 3.4 through comparison with test results available for samples characterised by single-scale porosity. Failure of samples characterised by a double-scale porosity is finally analyzed in Section 3.6.

3.2 The phase-field approach to fracture

We consider an arbitrary body occupying a domain $\Omega \in \mathbb{R}^{n_{dim}}$, with boundary $\partial\Omega \in \mathbb{R}^{n_{dim}-1}$, in the Euclidean space of dimension n_{dim}, in which an evolving internal discontinuity surface Γ is postulated to exist. A material point is denoted by $\mathbf{x}$ and body forces by $\mathbf{b} : \Omega \rightarrow \mathbb{R}^{n_{dim}}$. Mixed boundary conditions are prescribed along non-overlapping parts $\partial\Omega_t \cup \partial\Omega_u = \partial\Omega$ in the usual form

$$\mathbf{u} = \overline{\mathbf{u}} \quad \text{on } \partial\Omega_u \quad \text{and} \quad \boldsymbol{\sigma} \cdot \mathbf{n} = \overline{\mathbf{T}} \quad \text{on } \partial\Omega_t\,, \tag{3.1}$$

where $\mathbf{n}$ denotes the outward unit normal to the boundary, $\mathbf{u}$ is the displacement field and $\boldsymbol{\sigma}$ the Cauchy stress tensor, while $\overline{\mathbf{u}}$ and $\overline{\mathbf{T}}$ are prescribed surface displacements and tractions.

The variational approach to brittle fracture governing the crack nucleation, propagation and branching is set up through the definition of the free energy functional [141, 150]:

$$\Pi(\mathbf{u}, \Gamma) = \Pi_\Omega(\mathbf{u}, \Gamma) + \Pi_\Gamma(\Gamma), \tag{3.2}$$

embodying the sum between the elastic bulk energy Π_Ω stored in the damaged body and the energy Π_Γ necessary to nucleate and propagate a Griffith crack [151], defined as

$$\Pi_\Omega(\mathbf{u}, \Gamma) + \Pi_\Gamma(\Gamma) = \int_{\Omega\backslash\Gamma} \psi^e(\boldsymbol{\varepsilon})\, \mathrm{d}\mathbf{x} + \int_\Gamma \mathcal{G}_c(\mathbf{u}, s)\mathrm{d}\Gamma\,, \tag{3.3}$$

where ψ^e is the elastic strain energy density, function of strain $\boldsymbol{\varepsilon}$, and $\mathcal{G}_c$ is the fracture energy, function of the displacement $\mathbf{u}$ and of the phase field variable s. The phase field variable $s \in [0, 1]$ is an internal state variable, ranging between 0 and 1 and representing isotropic damage, so that $s = 0$ is representative of the intact material, while $s = 1$ characterises the fully damaged state.

3.2.1 The regularised variational formulation

Within the regularised framework of the phase field approach [133, 141] , the potential energy of the system is decomposed into two terms:

$$\Pi(\mathbf{u},s) = \int_{\Omega} \psi^e(\boldsymbol{\varepsilon},s)\,\mathrm{d}\mathbf{x} + G_c \int_{\Omega} \gamma(s,\nabla s)\,\mathrm{d}\mathbf{x}\,, \tag{3.4}$$

where $\psi^e(\boldsymbol{\varepsilon},s)$ is the energy density of the bulk for the damaged state, and $\gamma(s,\nabla s)$ is the crack density functional, with ∇ denoting the spatial gradient operator. As a result, the total free energy density of the bulk $\hat{\psi}$ reads $\hat{\psi}(\boldsymbol{\varepsilon},s) = \psi^e(\boldsymbol{\varepsilon},s) + G_c\gamma(s,\nabla s)$. According to [141] , the functional $\gamma(s,\nabla s)$, which is a convex function composed by a quadratic term of s and another quadratic term involving its gradient, is given by:

$$\gamma(s,\nabla s) = \frac{1}{2l}s^2 + \frac{l}{2}|\nabla s|^2\,, \tag{3.5}$$

where l stands for a regularisation characteristic length, physically related to the smeared crack width. Thus, when the characteristic regularisation parameter tends to zero ($l \to 0$), then the formulation outlined in Eq.(3.4) tends to Eq.(3.3) in the sense of the so-called Γ-convergence, so that the corresponding Euler equations associated with the phase-field problem become

$$s - l^2\nabla^2 s = 0 \quad \text{in}\,\Omega \quad \text{and} \quad \nabla s\cdot\mathbf{n} = 0 \quad \text{in}\,\partial\Omega, \tag{3.6}$$

where $\nabla^2 s$ stands for the Laplacian of the phase field variable.

To avoid damage in compression and allow fracture only due to a tensile stress state, the following 'tensile-compressive' decomposition is assumed for the energy density in the bulk $\psi^e(\boldsymbol{\varepsilon},s)$, see [152]

$$\psi^e(\boldsymbol{\varepsilon},s) = g(s)\psi^e_+(\boldsymbol{\varepsilon}) + \psi^e_-(\boldsymbol{\varepsilon}), \tag{3.7}$$

where the positive and negative parts of the energy density are defined as

$$\psi^e_\pm(\boldsymbol{\varepsilon}) = \frac{\lambda}{2}\langle \mathrm{tr}\boldsymbol{\varepsilon}\rangle^2_\pm + \mu\,\mathrm{tr}\boldsymbol{\varepsilon}^2_\pm, \tag{3.8}$$

where λ and μ are the Lamé constants, $\mathrm{tr}(\cdot)$ denotes the trace operator, the Macaulay brackets are defined for every scalar x as $\langle x\rangle_\pm = (x \pm |x|)/2$, and $g(s)$ is a degradation function that assumes the form $g(s) = (1-s)^2 + k$, where k is a residual stiffness to avoid ill conditioning issues. In the above equations, $\boldsymbol{\varepsilon} = \boldsymbol{\varepsilon}_+ + \boldsymbol{\varepsilon}_-$, so that if the spectral representation for the strain is denoted as

$$\boldsymbol{\varepsilon} = \sum_{i=1}^{3} \epsilon_i \boldsymbol{e}_i \otimes \boldsymbol{e}_i, \tag{3.9}$$

where ϵ_i are the three principal strains and $\boldsymbol{e}_i$ the corresponding principal strain directions, the tensile and compressive parts associated to ε are, respectively:

$$\boldsymbol{\varepsilon}_+ = \sum_{i=1}^{3} \langle \epsilon_i \rangle_+ \boldsymbol{e}_i \otimes \boldsymbol{e}_i, \qquad \text{and} \qquad \boldsymbol{\varepsilon}_- = \sum_{i=1}^{3} \langle \epsilon_i \rangle_- \boldsymbol{e}_i \otimes \boldsymbol{e}_i. \tag{3.10}$$

The split of the strain into tensile and compressive components is necessary to introduce the assumption that damage only occurs under tensile strain. A standard derivation [153] leads to the Cauchy stress tensor from the strain energy density (3.8):

$$\boldsymbol{\sigma} = g(s)\boldsymbol{\sigma}_+ + \boldsymbol{\sigma}_- = \left\{(1-s)^2 + k\right\} \left(\lambda \langle \mathrm{tr}\boldsymbol{\varepsilon}\rangle_+ \mathbf{I} + 2\mu\boldsymbol{\varepsilon}_+\right) + \lambda \langle \mathrm{tr}\boldsymbol{\varepsilon}\rangle_- \mathbf{I} + 2\mu\boldsymbol{\varepsilon}_-, \tag{3.11}$$

where $\mathbf{I}$ denotes the second-order identity tensor. The thermodynamic consistency according to the Clausius-Plank inequality of the present formulation has been comprehensively addressed in [141], and consequently specific details are omitted here for the sake of brevity.

3.2.2 Weak form of the variational problem

The weak form corresponding to the phase field model for brittle fracture can be derived following a standard Galerkin procedure. In particular, the weak form of the coupled displacement and phase-field damage problem according to Eq.(3.4) can be written as

$$\begin{aligned} \delta\Pi = \int_{\Omega} \boldsymbol{\sigma}(\mathbf{u}) : \boldsymbol{\varepsilon}(\mathbf{v})\, \mathrm{d}\mathbf{x} - \int_{\Omega} 2H(1-s)\phi\, \mathrm{d}\mathbf{x} + \\ + \int_{\Omega} G_c l \left\{ \frac{1}{l^2} s\phi + \nabla s \cdot \nabla \phi \right\} \mathrm{d}\mathbf{x} + \delta\Pi_{\mathrm{ext}}, \end{aligned} \tag{3.12}$$

where $\mathbf{v}$ is the vector of the displacement test functions defined on $\mathbf{H}^1_0(\Omega)$, ϕ stands for the phase field test function defined on $\mathrm{H}^1_0(\Omega)$, and $H(\boldsymbol{\varepsilon}) = \max_{\tau\in[0,t]} \left\{\psi^e_+(\boldsymbol{\varepsilon}(\tau))\right\}$, is the strain history function accounting for the irreversibility of crack formation [141, 154] . Eq.(3.12) holds for any trial functions $\mathbf{v}$ and ϕ. The external contribution to the variation of the bulk functional in Eq.(3.12) is defined as follows:

$$\delta\Pi_{\mathrm{ext}}(\mathbf{u}, \mathbf{v}) = \int_{\partial\Omega} \overline{\mathbf{T}} \cdot \mathbf{v}\, \mathrm{d}\Gamma + \int_{\Omega} \mathbf{b} \cdot \mathbf{v}\, \mathrm{d}\mathbf{x}. \tag{3.13}$$

3.2.3 Finite element formulation

The mechanical problem can be stated as:
find $\mathbf{u} \in \mathbf{U} = \left\{\mathbf{u} \,|\, \mathbf{u} = \overline{\mathbf{u}} \text{ on } \partial\Omega_u, \mathbf{u} \in \mathbf{H}^1(\Omega)\right\}$ such that

$$\int_{\Omega} \boldsymbol{\sigma}(\mathbf{u}) : \boldsymbol{\varepsilon}(\mathbf{v})\, \mathrm{d}\mathbf{x} = \int_{\partial\Omega} \overline{\mathbf{T}} \cdot \mathbf{v}\, \mathrm{d}\Gamma + \int_{\Omega} \mathbf{b} \cdot \mathbf{v}\, \mathrm{d}\mathbf{x},\ \forall \mathbf{v} \in \mathbf{H}^1_0(\Omega), \tag{3.14}$$

while the phase field problem is formulated as:
find $s \in S = \{s \mid s = 0 \text{ on } \Gamma, s \in \mathrm{H}^1(\Omega)\}$ such that

$$\int_\Omega G_c l \,\nabla s \cdot \nabla \phi \,\mathrm{d}\mathbf{x} + \int_\Omega \Big\{\frac{G_c}{l} + 2H\Big\} s\phi \,\mathrm{d}\mathbf{x} = \int_\Omega 2H\phi \,\mathrm{d}\mathbf{x},\ \forall \phi \in \mathrm{H}^1_0(\Omega). \tag{3.15}$$

To solve the quasi-static evolution problems for brittle fracture, isoparametric linear triangular finite elements are used for the spatial discretisation, and a staggered solution scheme is considered. This scheme introduces a simple approximation[2] which allows to decouple the governing equations, which can then solved independently. Staggered schemes based on alternate minimisation, exploit the convexity of the energy functional with respect to each individual variable **u** and s [155] . The solver has been implemented in the software FEniCS.

3.2.4 Newton-Raphson procedure

Despite the splitting into the two dynamics (3.14) and (3.15) reduces the phase field to a linear problem, the mechanical problem still remains nonlinear, because of the piece-wise linearity of the constitutive law, requiring a spectral decomposition of the strain. Therefore, its consistent linearisation is required. The linear form defined by the residual is given by:

$$\begin{aligned} F(\mathbf{u},\mathbf{v}) = &\int_\Omega \Big\{((1-s)^2 + k)\boldsymbol{\sigma}_+(\mathbf{u}) : \boldsymbol{\varepsilon}(\mathbf{v}) + \boldsymbol{\sigma}_-(\mathbf{u}) : \boldsymbol{\varepsilon}(\mathbf{v})\Big\} \,\mathrm{d}\mathbf{x} + \\ &- \int_{\partial\Omega} \overline{\mathbf{T}} \cdot \mathbf{v} \,\mathrm{d}\Gamma - \int_\Omega \mathbf{b} \cdot \mathbf{v} \,\mathrm{d}\mathbf{x} \end{aligned} \tag{3.16}$$

Given $\mathbf{u}^k$, the correction $\delta\mathbf{u}$ is the solution of the following linear variational problem:
find $\delta\mathbf{u} \in \mathbf{U}_0 = \{\mathbf{u} \mid \mathbf{u} = \mathbf{0} \text{ on } \partial\Omega_u, \mathbf{u} \in \mathbf{H}^1(\Omega)\}$ such that

$$J(\delta\mathbf{u}, \mathbf{v}; \mathbf{u}^k) = -F(\mathbf{u}^k, \mathbf{v}),\ \forall \mathbf{v} \in \mathbf{H}^1_0(\Omega)$$

and then iterate as $\mathbf{u}^{k+1} = \mathbf{u}^k + \delta\mathbf{u}$. The Jacobian entering the formulation is given by:

$$J(\delta\mathbf{u}, \mathbf{v}; \mathbf{u}) = \int_\Omega \Big\{((1-s)^2 + k)\partial\boldsymbol{\sigma}_+(\delta\mathbf{u}, \mathbf{u}) : \boldsymbol{\varepsilon}(\mathbf{v}) + \partial\boldsymbol{\sigma}_-(\delta\mathbf{u}, \mathbf{u}) : \boldsymbol{\varepsilon}(\mathbf{v})\Big\} \,\mathrm{d}\mathbf{x}. \tag{3.17}$$

Let be $\{\lambda_i(\mathbf{u})\}_i$ and $\{\mathbf{v}_i(\mathbf{u})\}_i$ respectively the eigenvalues and eigenvectors of $\boldsymbol{\varepsilon}$ at the current iteration $\mathbf{u}$ (where the superscript k is here not displayed to simplify notation) of the Newton-Raphson scheme, and $\mathbf{Q}$ is the orthogonal matrix whose columns are the normalised eigenvectors. The following matrices are defined $\mathbf{D}_i^* = (d_{i,j}^*)$ for $i = 1, 2, 3$, where

---

[2] Algorithmic decoupling of the coupled governing equations is achieved by approximating the history field variable H, of equation (3.15), at the current time step in terms of the displacement field at the previous time step [141].

$$d_{i,j}^* = \begin{cases} \dfrac{1}{\lambda_j - \lambda_i} & i \neq j \\ 0 & i = j \end{cases} \tag{3.18}$$

and $\mathbf{L}_i^* = \mathbf{Q}\mathbf{D}_i^*\mathbf{Q}_i^{\mathrm{T}}$. Then, following [156], the derivatives of the eigensystem are defined as $\delta\mathbf{v}_i = -\mathbf{L}_i^*\boldsymbol{\varepsilon}(\delta\mathbf{u})\mathbf{v}_i$ and $\delta\lambda_i = \mathbf{v}_i^{\mathrm{T}}\varepsilon(\delta\mathbf{u})\mathbf{v}_i$. Moreover, the derivatives of matrix $\mathbf{Q}$ and $\boldsymbol{\Lambda}_+$ can be defined as $\delta\mathbf{Q} = (\delta\mathbf{v}_1|\delta\mathbf{v}_2|\delta\mathbf{v}_3)$ and $\delta\boldsymbol{\Lambda}_+ = \mathrm{diag}(\delta\lambda_1^+, \delta\lambda_2^+, \delta\lambda_3^+)$, where

$$\delta\lambda_i^+ = \begin{cases} 0 & \text{if } \lambda_i < 0 \\ \delta\lambda_i & \text{else} \end{cases}. \tag{3.19}$$

Finally the derivatives of the stress tensor components $\partial\sigma_+$ and $\partial\sigma_-$ are defined as:

$$\partial\sigma_+ = \lambda H_+(\mathrm{tr}\boldsymbol{\varepsilon}(\delta\mathbf{u}))\mathbf{I} + 2\mu\left(\delta\mathbf{Q}\boldsymbol{\Lambda}_+\mathbf{Q}^{\mathrm{T}} + \mathbf{Q}\delta\boldsymbol{\Lambda}_+\mathbf{Q}^{\mathrm{T}} + \mathbf{Q}\boldsymbol{\Lambda}_+\delta\mathbf{Q}^{\mathrm{T}}\right) \tag{3.20}$$

where

$$H_+(\mathrm{tr}\boldsymbol{\varepsilon}(\delta\mathbf{u})) = \begin{cases} \mathrm{tr}(\boldsymbol{\varepsilon}(\delta\mathbf{u})) & \text{if } \mathrm{tr}(\boldsymbol{\varepsilon}(\mathbf{u})) > 0 \\ 0 & \text{else} \end{cases} \tag{3.21}$$

and an analogous expression holds for $\partial\sigma_-$.

3.3 Crack trajectories in plates with holes

A series of experiments has been designed and performed at the ‘Instabilities Lab’ of the University of Trento, in which PMMA plates perforated with one or two circular holes and containing one or two notches have been subjected to increasing tensile opening far field displacement, so to induce crack growth and curvilinear crack paths influenced by holes. During the tests, the force is measured by the loading cell of the testing machine in correspondence of each imposed displacement value. Moreover, photoelasticity is exploited to visualise the principal stress field component and the crack trajectory for selected steps of crack growth..

In particular, Figure 3.2 reports the experimental result for a tensile test on a V-notched PMMA plate with one isolated circular hole. The plate has been put under traction at one end, so to induce crack nucleation at the tip of the notch (1); the particular loading condition induces tensile stress in the region ahead of the crack thus making it propagate horizontally (2); upon reaching a zone sufficiently far away from the notch tip, compression stresses develops and the crack abruptly changes direction to a more vertical one (3), until eventually converging into the hole (4).

To reproduce the behaviour of the crack, the phase-field model proposed above (3.2.1) has been calibrated and tested. The parameters G_c (fracture energy) and l (crack smoothness) have been chosen to be equal to 8 MPa mm and 0.1mm, respectively. As it is shown from Fig. 3.2 (down) the phase-field is capable of reproducing the whole crack trajectory.

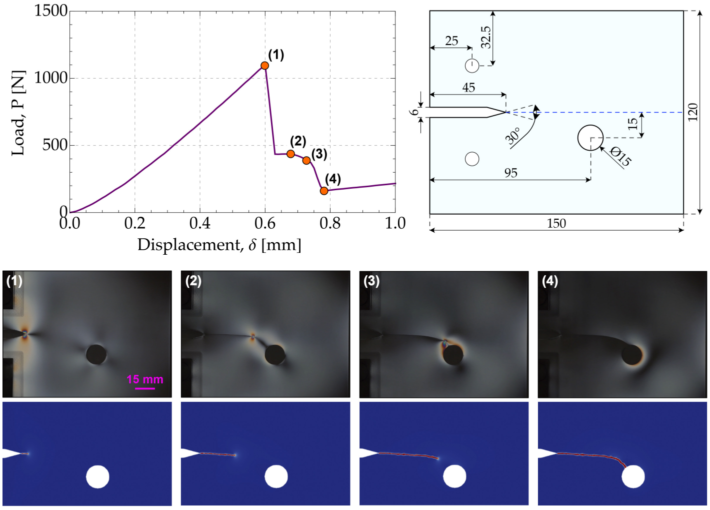

FIGURE 3.2: Tensile test on a v-notched PMMA plate with a single hole.

3.4 Two scales porosity and mesh generation

In a representative volume element, the porosity $0 \leq \Phi \leq 1$, or void fraction, is defined as the ratio between the volume of voids and the total volume of the element. Under the assumption that the voids are circular holes in a two-dimensional formulation, a probability distribution function (PDF) of the voids' size of a typical BA sample has been built by means of an *ad hoc* Matlab code.

Note that BA samples are characterised by three levels of porosity, namely, macroscopic, mesoscopic, and microscopic [149] . The microscopic level will not be considered, as it is believed not to influence macroscopic crack growth. Note also that the two-dimensional formulation developed in this chapter correctly fits the specific structure that BA inherits from wood, which presents elongated grains and parallel channels, with approximately circular section (Figure 3.1). The obtained PDF has a characteristic bi-modal shape, clearly visible in Figure 3.3. The first peak, occurring at high values of the void radius, is representative of a macro-porosity Φ_{macro}, while the second peak, is representative of a meso-porosity Φ_{meso}. The total porosity can be obtained as the sum of the two contributions $\Phi = \Phi_{\text{macro}} + \Phi_{\text{meso}}$.

The obtained PDF was then used as a reference for a large in silico generation of samples of porous materials, to be tested in simulations performed

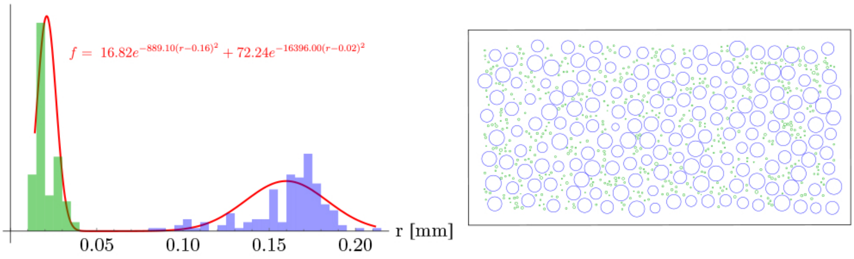

FIGURE 3.3: Left: Probability density function (PDF) representing the distribution of the voids' radius, r, in a typical BA specimen and evidencing a double porosity (macro-porosity is marked in blue, while meso-porosity in green). Function f reported in red is an interpolating function for the density distribution of BA samples. Right: An example of a sample generated in silico, displaying a double porosity, in agreement with our experimental data and resembling the transverse section of the rattan wood from which the BA has been obtained.

with the proposed phase-field approach. These samples have been constructed by randomly placing non-overlapping voids, characterised by the pore-radius distribution in agreement with that of real specimens (see Figure 3.3) inside a rectangle having the dimensions of the tested BA samples.

In order to effectively investigate the influence of two-scale porosity on crack pattern in a ceramic material, simulations have been performed of an uniaxial compression tests on samples characterised by a distribution of both macro and meso voids and, for comparison, on a set of samples where only a macro porosity is present. Specimens belonging to the latter set have been built with a value of porosity ranging between 15% and 40%. For each value of porosity, three specimens differing only in the spatial arrangement of voids were considered. The placement of the voids has been obtained through a random generation algorithm, using the software Mathematica. In addition, specimens characterised by double scale porosities have been generated via a dedicated algorithm developed in Mathematica.

The same macroscopic porosity was assumed for the samples characterised by porous of only one size porosity and for the samples with the double scale void distribution. The value of the meso porosity was assumed to range between 2% and 10% of the total specimen porosity. Note that to enhance the numerical performance of simulations, interactions were avoided between voids and the free boundary of the sample. Therefore, a thin perimetral layer free from voids has been always introduced.

All the samples generated in silico, have the aspect ratio

$$L/H = 4.5\text{mm}/9\text{mm}$$

and are characterised by a Young's Modulus and a Poisson ratio of the matrix material respectively set to be equal to E $=$ 70 MPa and $\nu = 0.25$. The lengthscale parameter l, which regulates the sharpness of the phase-field, and fracture energy G_c, were chosen to be equal to 0.012 mm and 0.0025 MPa mm respectively. These are the values that allows to retrieve the overall stiffness and strength of a BA sample when the proper macro-porosity (15%) is selected.

Five of the in silico generated samples are shown in Fig. 3.4, where the macro-porosity has been set to be equal to

$$\Phi_{\text{macro}} = \{15\%, 20\%, 25\%, 30\%, 40\%\}$$

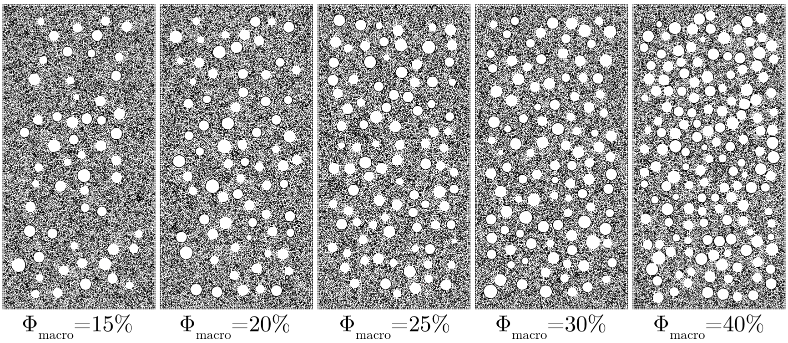
Φ_{macro}=15%
Φ_{macro}=20%
Φ_{macro}=25%
Φ_{macro}=30%
Φ_{macro}=40%

FIGURE 3.4: From left to right: finite element meshes of the specimen in-silico tested at increasing porosity.

The sets of samples generated in silico, characterised by different porosity and critical surface energy G_c are reported in table 3.1.

Samples name	Φ_{macro}
S0	0%
S1, S6, S11	15%
S2, S7, S12	20%
S3, S8, S13	25%
S4, S9, S14	30%
S5, S10, S15	40%

TAB. 3.1: Sets of tested samples: Φ_{macro} stands for macro-porosity.

Prior to the analysis of the set of specimen of Table 3.1, reported in the section 3.5, a sensitivity analysis on the mesh refinement has been conducted. Numerical analysis of a compression test on various in silico samples for increasing mesh refinement (h, number of nodes discretising the side L of samples) were analysed. Different mesh refinements $h \in$ {100, 150, 200, 250, 300} are considered. The samples are characterised by a fixed aspect ratio L/H=4.5 mm/9 mm and with different values of macro-porosity Φ_{macro}.

In order to find the value of h for which the solution becomes independent from the mesh size, strength and stiffness dimensionless ratios $\underline{E}$ and $\underline{\sigma}$

were evaluated from the resulting stress-strain curves as a function of h. As shown in Fig. 3.5, independence of mesh size is achieved for h$\geq$ 200. The value h= 200 is than used in the subsequent simulations.

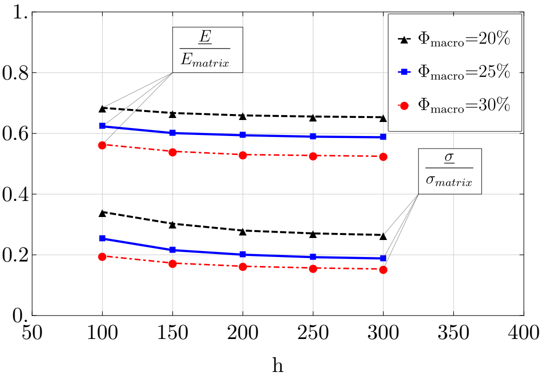

FIGURE 3.5: Mesh sensitivity analysis: strength and stiffness dimensionless ratios as functions of the mesh and for different values of macro-porosity.

3.5 The effect of the porosity on the elastic properties

The overall elastic properties of a porous material can be determined in a number of ways. Following the Coble-Kingery model , the effective Young's modulus defining an equivalent homogeneous elastic solid $\underline{\mathrm{E}}$ is defined by the relation

$$\frac{\underline{\mathrm{E}}}{\mathrm{E}_{matrix}} = (1-\Phi)^2, \tag{3.22}$$

valid in the special case of spherical voids and Poisson ratio close to 0.2. The approach by Coble is the simplest way to account for non linear dependence of effective elastic moduli on porosity and is obtained by adding a quadratic term to the linear relation $\mathrm{E}(\Phi)$ obtained in the dilute approximation. Equation (3.22) is exactly the same as the one obtained with the differential approach in micromechanics.

Another important relation which provides the stress at failure (in other words the peak stress) in a uniaxial compression test, $\underline{\sigma}$, was provided by in the form

$$\underline{\sigma}/\sigma_{\mathrm{matrix}} = \mathrm{e}^{-b\Phi}, \tag{3.23}$$

where b is a coefficient to be fitted with experimental measurements.

A group of simulations have been conducted on specimens characterised by single-scale porosity, $\Phi_{\mathrm{meso}} = 0$ and $\Phi = \Phi_{\mathrm{macro}}$. As previously pointed out, a uniaxial compression test, aligned parallel to the horizontal direction, is simulated on sets of three numerical specimens with varying macroporosity, Fig. 3.4. The only difference among each set of specimens is the spatial distribution of the circular voids.

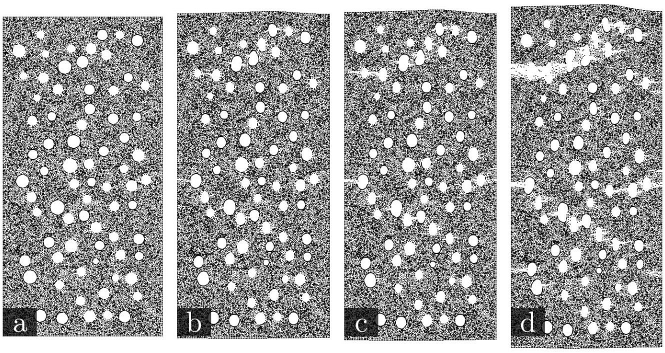

(u=0.0 mm) (u=-1.9 • 10^{-1}mm) (u=-2.4 • 10^{-1}mm) (u=-2.8 • 10^{-1}mm)

FIGURE 3.6: Evolution of the crack pattern in the deformed mesh for subsequent compressive loading steps for sample S2 ($\Phi_{\text{macro}} =$ 20%) at increasing values of displacement applied at the two lateral edges.

The simulations of the compression test have been carried out until complete failure of the specimens, results are reported in Figures 3.6 and 3.7 the former in terms of displacement fields, the latter in terms of mean stress vs. mean strain. In particular, figure 3.6 shows the evolution of the displacements in a specimen with $\Phi_{\text{macro}} = 20\%$. As clearly depicted, the model can effectively catch the damage nucleation (Figure 3.6, **a**-**b**), propagation (Figure 3.6, **c**), and final failure of the specimen (Figure 3.6, **d**). The cracks are shown to develop aligned almost parallel to the loading direction. Stress-strain curves show that the behaviour of the specimens remains linear up to the peak value of stress (Figures 3.6 and 3.7 **a**→**b**), and later a softening branch develops, as a consequence of cracks evolution, interaction with voids and other cracks, and merging into large fractures (**c**, **d**). The stress was evaluated as the mean value (the total force exerted on the faces of the specimen where displacement is imposed, divided by the cross sectional area, $A = 1 \cdot \mathrm{H}$ in a two-dimensional context). The strain, likewise, is reported as a mean value, obtained by dividing the horizontal imposed displacement by the length of the specimen L.

For each value of macro-porosity, three specimens with different distribution of voids have been prepared. Each stress-strain curve is characterised by an almost linear part, in which stiffness (the tangent line to the stress-strain curve) varies up to the 10% with respect to the slope at the origin, followed by a softening branch. As one can see from Figure 3.7 (graph on the right) the shape of the softening branch and the value of the peak stress depend on the geometrical distribution of voids. By increasing the value of macro-porosity, the effect of the geometrical distribution of the

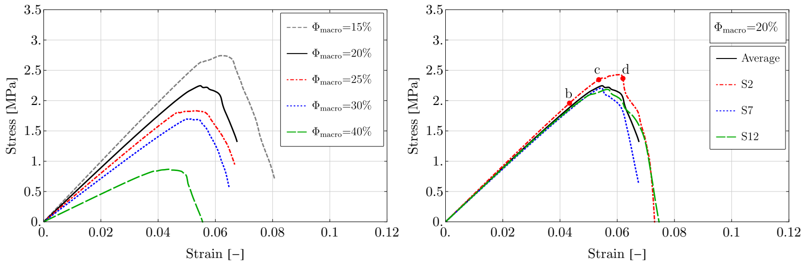

FIGURE 3.7: Simulations of the mean stress-strain response for porous specimens undergoing uniaxial compression. Only a macro porosity is present.

voids on the overall behaviour becomes more and more negligible, Table 3.3.

$\Phi_{\text{macro}} =$	15%	20%	25%	30%	32%	40%
Mean($\underline{E}$) [MPa]	49.8	44.7	40.2	35.9	33.5	23.0
Mean($\underline{\sigma}$) [MPa]	2.84	2.27	1.86	1.73	1.59	0.90
St.Dev($\underline{E}$)/Mean($\underline{E}$)	2.31%	2.88%	3.06%	3.41%	1.90%	2.87%
St.Dev($\underline{\sigma}$)/Mean($\underline{\sigma}$)	12.9%	5.9%	6.70%	6.87%	4.03%	10.8%

TAB. 3.2: Mean value and standard deviation of Young's Modulus and peak stress for different values of the macro-porosity as obtained from simulations of compression tests.

The simulated responses of the samples with single scale porosity, allows for the evaluation of the peak stress and of the overall Young's modulus at different values of macro porosity, Φ_{macro}. Results are reported in Figure 3.8, respectively on the left and on the right. The results of the computations are compared with the exponential relation, equation (3.23) and with equation (3.22). Results obtained with the Hashin-Shtrikman upper bound are also reported for comparison. In Figure 3.8 the fitting of the Young's modulus data has been done using the Coble-Kingery model.

The phase field approach permits an investigation of the crack nucleation and of the mechanisms of its evolution, Figure 3.9. After nucleation on the boundary of the pores, cracks develop horizontally (parallel to the loading direction) until they merge with one another to create large patterns that cross the whole sample (Figure 3.9, below). This mechanism appears to be the same for all samples regardless of the value of total porosity, yet it is enhanced in high porous solids since, there, pores are inevitably closer to each other, a fact that speeds up the complete collapse of the specimen.
Observations of crack nucleation in the phase-field simulations are compared with the predictions of the so-called *minimum solid area* method (MSA). This method, which has been thoroughly studied by Rice [157–159], gives accurate estimates of the overall mechanical properties of porous materials by assuming that the desired property is proportional to the zero porosity value through the minimum fraction of solid area of the total body area

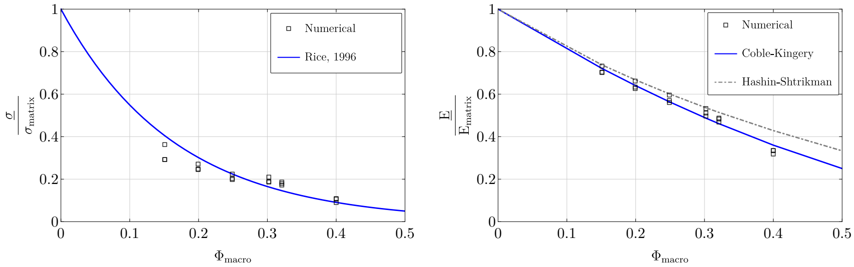

FIGURE 3.8: On the left: overall peak stress (normalized with respect to the matrix strength) as a function of macroporosity; on the right: overall Young's Modulus as a function of macro-porosity. The Hashin–Shtrikman upper bound and Coble–Kingery approach give good approximation of the scatter of the data.

normal to the stress axis. In the case of a compression test in the horizontal direction, the minimum solid area is evaluated among the vertical sections. As such, the method does not account for pore shapes nor orientations, nonetheless, as explained in , the technique has proven to be very efficient. Figure 3.10 shows the results of the comparison: in some cases (low porosity) damage nucleated at different locations, but the onset of crack was situated in the proximity of the MSA; in other cases (high porosity), on the other hand, the greater closeness of the pores plays an important role causing crack to nucleate in sections far away from the MSA. Lastly, Figure 3.11 shows the temporal evolution in two specimens ($\Phi_{\text{macro}} = 20\%$ and $\Phi_{\text{macro}} = 40\%$) of the elastic strain energy and the dissipated energy given respectively by:

$$E_{\text{s}} = \int_{\Omega} \{(1-s)^2 \psi^e_+(\mathbf{u}) + \psi^e_-(\mathbf{u})\}\, \mathrm{d}\mathbf{x}$$

and

$$E_{\text{d}} = \int_{\Omega} \{G_c l |\nabla s|^2 + \frac{G_c}{l} s^2\}\, \mathrm{d}\mathbf{x}.$$

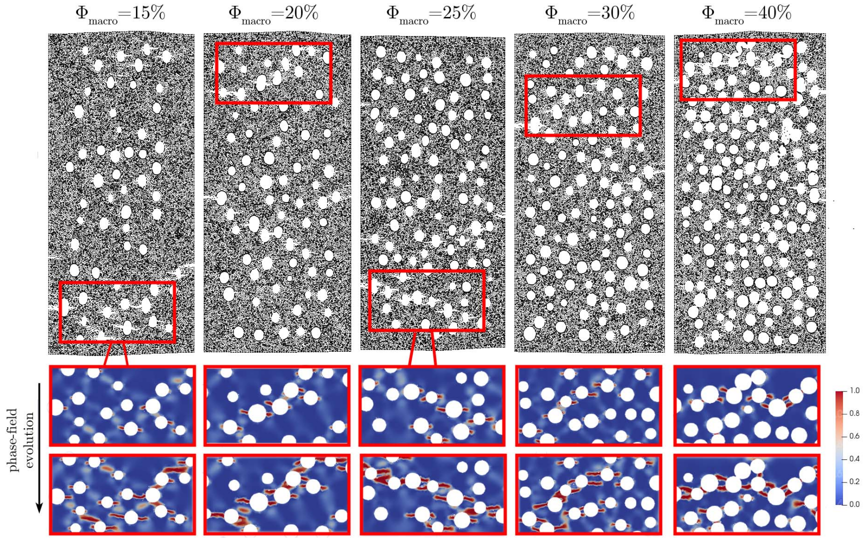
Φ_{macro}=15%
Φ_{macro}=20%
Φ_{macro}=25%
Φ_{macro}=30%
Φ_{macro}=40%
phase-field evolution
1.0
0.8
0.6
0.4
0.2
0.0

FIGURE 3.9: Deformed meshes (up) and phase-field evolution (down) for samples tested under uniaxial compression in the horizontal direction.

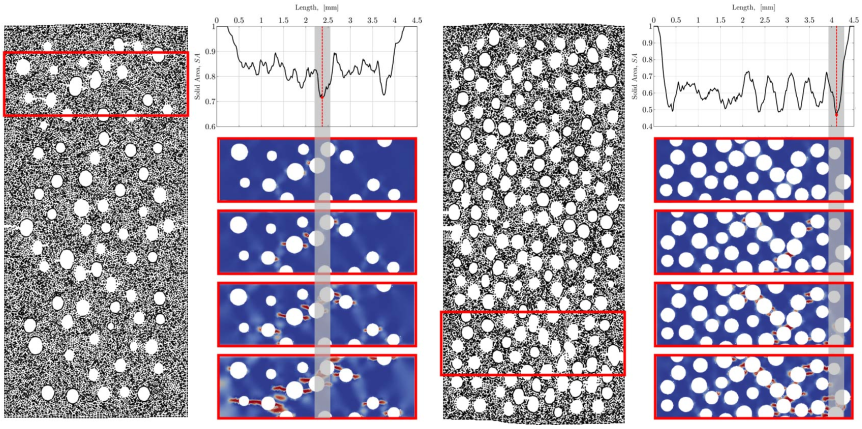

FIGURE 3.10: MSA prediction of the cross-section where nucleation can occur in a specimen with $\Phi_{\text{macro}} = 20\%$ (on the left) and with $\Phi_{\text{macro}} = 40\%$ (on the right).

3.6 Crack propagation in a material with two-scale porosity

Samples with pores of two different sizes were created by means of an ad hoc algorithm on Mathematica. Each sample is characterised by two levels of porosity, as illustrated by the bimodal PDF chosen as reference in Figure

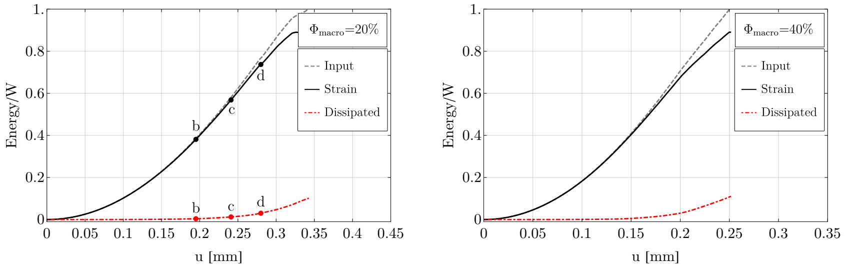

FIGURE 3.11: Energy evolution in the specimen S2 ($\Phi_{macro} = 20\%$, on the left) and S16 ($\Phi_{macro} = 40\%$, on the right) as a function of the horizontal displacement (u). W stands for the maximum of the input energy; *input* stands for input energy; *dissipated* for the dissipated energy; *strain* for the strain energy. Points b,c and d are those referring to Figures 3.6-3.7.

3.3 and shown to be representative of BA samples. For the 5 different values of macro-porosity, 5 specimens each with a different value of meso-porosity, were generated. The 25 specimens were then in-silico tested, accordingly to the previous simulations, under uniaxial compression. The porosities of the two sets of samples are summarised in table 3.3.

Samples name	Φ_{macro}	Φ_{meso}	Φ
S1A	15%	0%	15%
S1B	15%	2%	17%
S1C	15%	3%	18%
S1D	15%	5%	20%
S1E	15%	10%	25%
S2A	25%	0%	25%
S2B	25%	2%	27%
S2C	25%	3%	28%
S2D	25%	5%	30%
S2E	25%	10%	35%

TAB. 3.3: Two porosities of the samples generated for in-silico testing. Φ_{macro} stands for the macro-porosity and Φ_{macro} represents the meso-porosity.

Results are expressed in terms of mean stress vs. mean strain in Figure 3.12. Similarly to the single porosity specimens, those characterised by a double porosity showed an almost linear branch with slope variations of less than 10%, until the first peak is reached. Later, a softening behaviour prevails. For the specimens with higher values of meso-porosity, the softening curves display a slope less steep that those exhibited by the specimens with single porosity. This has to be attributed to greater damage diffusion occurring before the specimen failure, an effect which is less pronounced in specimens with a low level of macro-porosity.

The Young's modulus and peak stress are shown in Figure 3.13 at increasing macro-porosity and for different levels of meso-porosity. As expected, an increase in meso-porosity results in a degradation of the mechanical properties of a sample, regardless its given macro-porosity. This degradation affects the overall Young's Modulus much more than it does for the

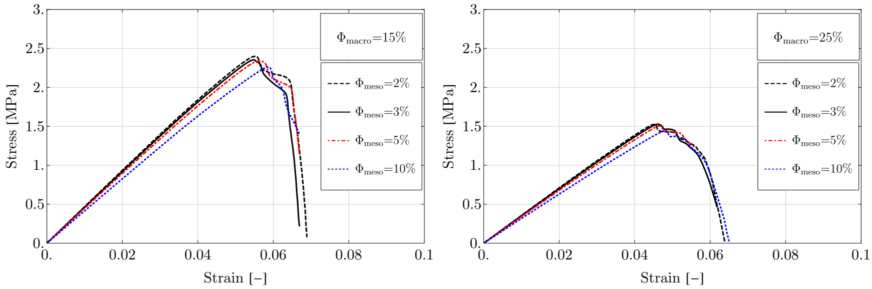

FIGURE 3.12: Mean stress vs mean strain for specimens with a macro-porosity equal to 15% (left) or to 25% (right) at increasing meso-porosity.

peak stress. On the other hand, increase on the macro-porosity (Figure 3.13 on the right) seems to have similar effects on both material properties.

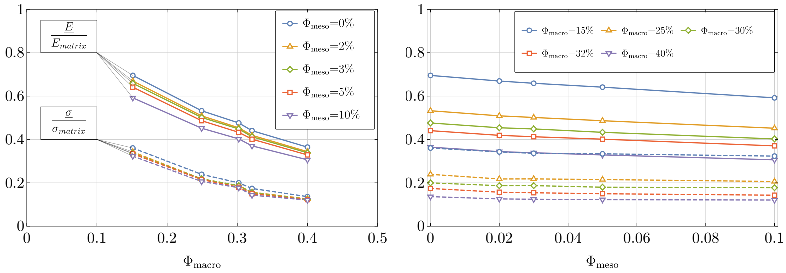

FIGURE 3.13: Summary of the overall mechanical properties for porous materials with different void sizes. On the left: overall stiffness (continuous lines) and strength (dashed lines) as functions of macro-porosity, for different values of meso-porosity. On the right: overall stiffness (continuous lines) and strength (dashed lines) as functions of meso-porosity, for different values of macro-porosity.

Reported in Figure 3.14 are the overall properties of the different specimen in terms of total porosity. A striking, yet relatively known in the literature , result is that for a fixed value of total porosity, samples behave best when they have lower macro porosity (triangles facing downwards clearly above the trendlines). This means that macro porosity is more detrimental than meso-porosity on the mechanical behaviour.

Color maps of the normalized Young modulus and strength resulting from the stress-strain curves as a functions of macro and meso porosities Φ_{macro} and Φ_{meso}, are shown in Figure 3.15. It can be noticed that the two scales of porosity have a combined non-linear effect on the macroscopic overall elastic behaviour of the properties of the porous material. In particular, there is an interaction between the two scales of porosity resulting in a non-linear effect (the two scales Φ_{macro} and Φ_{meso} are correlated) on the resulting toughness of the material in the strip $0 \leq \Phi_{\text{macro}} \leq 0.3$. For

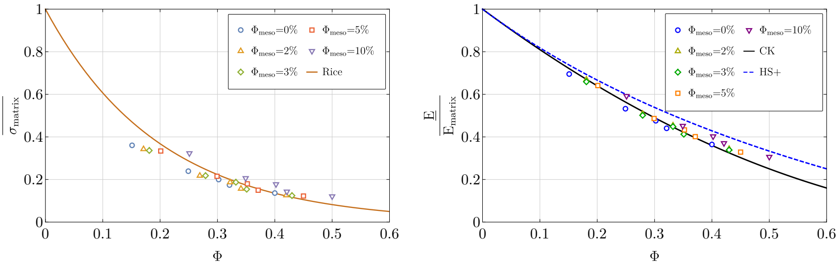

FIGURE 3.14: Dimensionless peak stress (left) and Young's modulus (right) versus total porosity for samples characterised by double porosity.

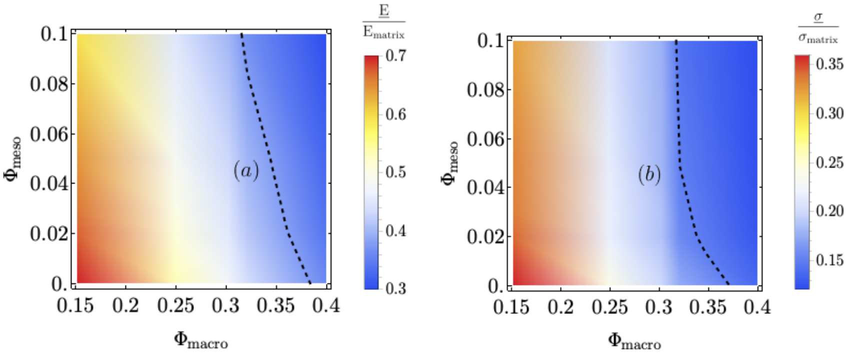

FIGURE 3.15: Density plot for the normalised Young's Modulus and normalised strength of the specimens as functions of macro and meso porosity.

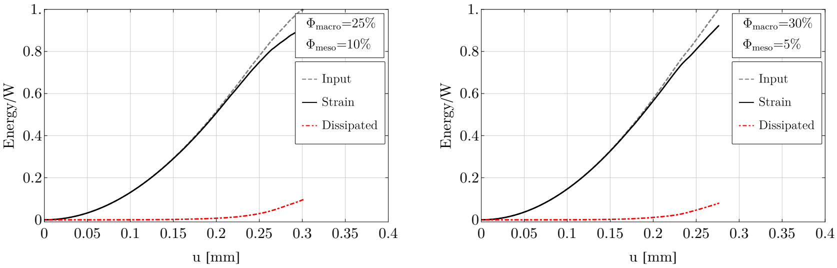

FIGURE 3.16: Energy evolution (normalised with respect the total energy input W) for samples with double porosity. Macro-porosity is 25% (left) and 30% (right) and meso-porosity 10% (left) and 5% (right). *Input*, which stands for input energy, evaluated as the scalar product between the imposed displacement and the traction at the right boundary of the samples;

$\Phi_{\text{macro}} > 0.3$ the effect of the macro-scale of porosity Φ_{macro} becomes predominant.

Investigation of the crack patterns as influenced by meso porosity at fixed values of macro porosity, can be inferred from results reported in Figure 3.17. Two are the main mechanism of failure in the double porosity specimen (Figure 3.17, where the phase-field of a compression test on specimen with 25% macro-porosity is shown): i. crack nucleates at the edge of macro-pores, and meso-pores helps those reach and connect to other cracks (phase-field in red); ii. cracks are born in proximity of meso-pores and develops by connecting to macro-pores (phase-field in green).

Figure 3.18 shows that the MSA method is quite accurate at locating the section in which damage onset will take place. The method seems more effective for lower levels of meso-porosity while for higher meso-porosity voids interactions become more detrimental and thus the prediction is unreliable.

We present now the comparison between phase-field analysis and experimental results of a compression test on BA carried in the direction orthogonal to the fibres (fibrous nature inherited from wood) The test was performed by placing a prismatic sample in direct contact with two circular steel platens (40 mm in diameter and 5 mm thick), and compressed by imposing displacements to the upper platen. The test was carried on until complete crash of the sample. As one can see from Figure 3.19, two mechanisms of crack propagation are present: either crack nucleate and the proximity of large pores and develop horizontally, or meso pores act as source and then crack connect to larger voids.

The numerical model is capable of reproducing the effective birth and growth of crack aligned along the direction of loading.

From a comparison of the phase-field of compressed materials with multiple scales of porosity and experimental results on real BA samples, Figure 3.19, the following observations can be made: (i.) large pores act as source for cracks (the green arrow); (ii.) small pores act as source for smaller cracks (white arrows); (iii.) small pores act as bridges fostering crack propagation between far away macro-cracks (white arrow).

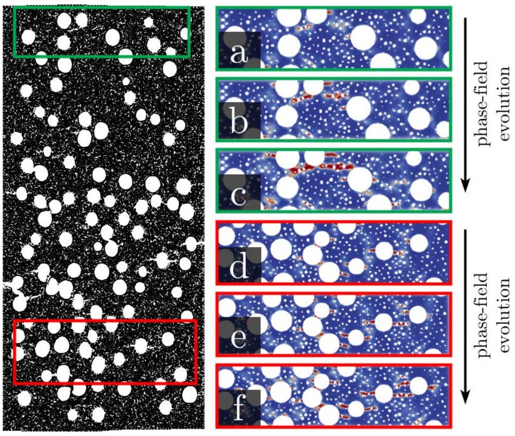

FIGURE 3.17: Phase-field evolution of sample S2D. The sample is characterised by a macro-porosity Φ_{macro} of 25% while meso-porosity Φ_{meso} amounts to the 10%. Meso pores are responsible for two mechasims: for the nucleation (a-b) and accretion (c) of cracks; for connecting far away macro pores (d-e) ultimately leading to failure (e).

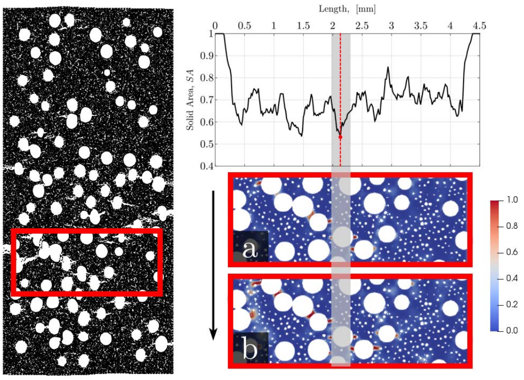

FIGURE 3.18: MSA prediction of the cross-section where damage should occur, and comparison with the results of the phase-field simulations for the specimens S2D ($\Phi_{\text{macro}} = 25\%$, $\Phi_{\text{meso}} = 10\%$).

3.7 Results and conclusions

Fracture growth is strongly influenced by inhomogeneities, which deviate cracks and deeply affect failure. Photoelastic experiments on PMMA plates with notches and circular holes embedded in them, show curve crack trajectory for particular loading conditions. The change in trajectory from the rectilinear path is due to the rotation of the principal tensile direction along the crack path, a thing which can be ascribed to both the presence of the void ahead of the crack and to the loading conditions. A phase-field model based on the energy split is employed to effectively reproduce this

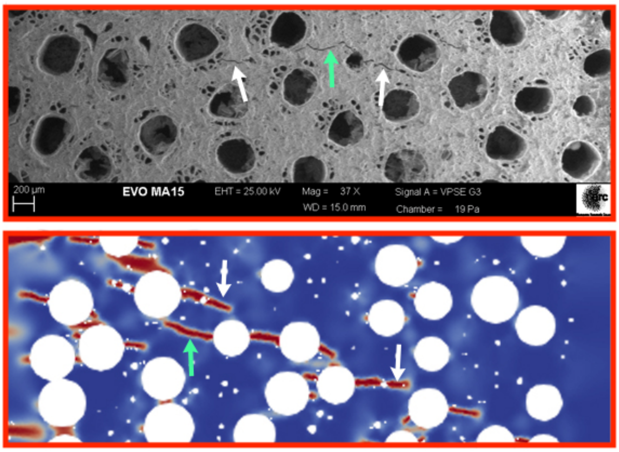

FIGURE 3.19: Crack pattern in a BA sample tested under compression orthogonal to the main channels (up). Phase-field simulating crack pattern in a porous material with two scales of porosity (down).

failure behaviour. This conclusion provides a firm experimental basis to several studies dedicated to the numerical simulation of crack propagation via phase-field in brittle materials.

Furthermore, failure of prismatic samples characterised by single-scale and double-scale porosity is analysed in the present work. The phase-field approach has proven to be efficient in the prediction of the behaviour at failure of brittle ceramics characterised by single or multiple porosity scales. In particular, mechanisms of crack nucleation and propagation are correctly reproduced: large pores induce crack nucleation while small pores foster their propagation by connecting far off pores; small pores cause the formation of small cracks which then propagate and reach larger voids to finally induce failure. Small pores (associated to what can be called *meso-porosity*) have proven to be responsible for damage diffusion in the specimen, a thing that causes the softening branches of the stress-strain curves for double-scale specimen to be less steep then those of single-scale specimen. Once the total porosity is fixed, specimens with higher values of meso-porosity performs better than those having a majority of macro-pores. As a consequence, pore size must be considered as a major influential parameter when dealing with porous ceramics.

By analysing the solutions of simulations with the phase-field approach of compression tests on porous materials, it was possible to compare its prediction of crack nucleation with those of the MSA method. The MSA method is a simple yet powerful instrument to determine the section of a material with organised porosity where damage may arise. Nonetheless, the chaotic and random distribution of voids in real porous ceramics has shown to pose a treat in the accuracy of this method; in very few cases the MSA method has efficiently predicted crack nucleation.

4

Reduced peridynamics for delamination of thin films

4.1 Introduction

Composite materials, and in particular laminates, have many applications in the aerospace and automotive industries. This is due to having high mechanical properties, such as strength and stiffness, at the cost of relatively low weight. Among the various type of damage that can detriment their mechanical response, composite laminates are especially subject to delamination. Delamination is an insidious type of failure which involves a loss of continuity of the material at an interface region, and which has negative consequences on the laminates strength and stiffness [36, 37]. As such, a lot of effort has been put to correctly model and predict its evolution mainly through the application of Cohesive Zone Models (CZM) [38–43] or extended finite element methods (XFEM). CZM assigns to the damage zones a traction-separation law which is cohesive and damage begins to develop when the stress reaches a limit defined in the costitutive law. The downside of the model is that crack path must be known beforehand, thus, spontaneous crack nucleation cannot be reproduced. The extended finite element method (XFEM) on the contrary was developed specifically for problems where the trajectory of a crack is unknown. Belytschko et al. [160] proposed this extended formulation by enriching the shape functions of fe-method with extra featured functions based on the partition of unity. Still, XFEM needs a special constitutive equation to deal with the process zone of the crack; a law which is typically cohesive.

The need of special techniques, such as CZM, to deal with fracture in general, and more in particular with delamination, emerges from the fact that local theories of continuum mechanics relay on the definition of strain. Therefore, equilibrium equations require the displacement to be differentiable, a thing that forbid discontinuities such as jumps [44].

In this regard, strongly nonlocal theories which employs integrals to define the equilibrium equations are particularly well-suited. Among the many

[45–48], the peridynamic theory of continuum mechanics has gained attention of the research community primarily because of its capability of treating fracture. Nevertheless, a very recent paper points the attention to a fully nonlocal theory of fractional order continua which seems to compete with peridynamics [49], although fracture and delamination has not yet been addressed there.

Peridynamics (PD) is a fairly recent nonlocal theory proposed in 2000 by S. A. Silling [35]. This approach can be regarded as the natural extension of molecular dynamics to a continuous medium and to arbitrarily large systems with long range interactions at the macroscale [50]. In the PD theory, the continuum is modelled as a collection of particles which can interact with one another through forces. The maximum distance between particles at which an interaction exists is called *horizon*. The type of interaction defines the kind of peridynamics at hand: a model where the forces acting on a pair of particles depend only on their own movement is called *bond-based* [51, 52]. An alternative form of PD, called *state-based*, has also been introduced in [53, 54]: there forces also depend on all the particles in their neighbourhood. PD has also been employed to model impact, explosion and high speed crashing [55–57].

The applications of PD to 2D elements have been thoroughly studied and numerical schemes have been developed to deal with these problems [58–60]. For instance, this is the case of debonding of multilaminates, which has been studied in [61–63] among others. Within 2D PD, dimensionally reduced formulations suitable for geometrically thin (nonlocal) solids have also been pursued. This is because they are particularly attractive as they can lead to faster computational algorithms and still lead to a good insight of the physical phenomenon (see e.g. [64, 65]). The proposed reduced models treat membrane tearing or in-plane failure, although they do not deal with damages occurring through the thickness, such as delamination.

Here, a reduced formulation of *bond-based* peridynamics, specifically tailored to account for through-thickness mode-I cracks, is introduced. This is achieved first by carefully characterizing the kinematics. To this aim, in Section 4.3, the displacement field is additively decomposed in the sum of its absolutely continuous part and its jump one. In a more mathematical language, we would say that the natural functional space in which geometrical changes for the continua at hand are allowed is the one formed by functions of Special Bounded Variations, SBV, largely utilised in analysis and its applications (see e.g. [67]). The latter singles out both the sites of discontinuities and their magnitude. Further assumptions on both parts of the displacement field lead to a reduced form of the elastic bond-based PD energy. In Section 4.3.3, for such an effective energy the reduced Lagrangian is then explicitly retrieved. This procedure and the assumptions mentioned above generate a hierarchy of terms characterizing the strain energy stored inside the planar element. This hierarchy of functionals allows for a consistent variational approach, governing the search of unknown displacement fields by means of a minimization procedure. Semi-analytical solutions for test cases are then compared with numerical simulations in Section 4.3.5. These are performed on fully three-dimensional systems and built by means of standard FEM analysis of PD bond-based body [68, 69], while the analytical model is based on the dimensionally reduced formulation previously described. The above mentioned comparison allows for showing that the numerical and analytical solutions exhibit a high degree of agreement, both in terms of moment-curvature relationship and in terms of nucleation and growth of the delamination surface. In Section 4.4, we assess the convergence between the proposed reduced model and local theories, when the *horizon*(δ) tends to zero. By enforcing a condition of bounded and non-vanishing energy the scaling of the displacement field with the horizon is established. Since the scaling of all the terms in the energy is then known, the nonlocal model can be localized and a cohesive reduced local formulation is retrieved. This is due to some terms of the energy associated to the jump part of the displacement surviving the limit operation.

4.2 A brief review of bond-based peridynamics

Bond-based peridynamic models a continuum body $\mathbb{B}$ in the standard three dimensional space, as a collection of material particles interacting with one another, in pairs, through bonds. Given any couple of interacting particles $\boldsymbol{x}$ and $\boldsymbol{x}'$, bonds exert forces on them, and in the most basic formulation of peridynamics (bond-based peridynamics), these forces act along the line connecting the pair of material points. The maximum distance two particles $\boldsymbol{x}$ and $\boldsymbol{x}'$ can have for an interaction to exist is called *horizon*, δ. All the particles $\boldsymbol{x}'$ within the finite distance δ from $\boldsymbol{x}$ make up its *family*, $\mathbb{H}$:

$$\mathbb{H} = \left\{ \boldsymbol{x}' \in \mathbb{B},\ \text{s.t.}\ |\boldsymbol{x} - \boldsymbol{x}'| \leq \delta \right\}.$$

When the body $\mathbb{B}$ undergoes a deformation, particles may change position; we call $\boldsymbol{u}[\boldsymbol{x}, t]$ the displacement of particle $\boldsymbol{x}$ at time t and $\boldsymbol{u}[\boldsymbol{x'}, t]$ that of the particle $\boldsymbol{x}'$. Such displacement causes a variation in the forces $\boldsymbol{f}$ exerted between the material points; these, along with applied loads make up the totality of the forces acting on a specific particle. If one represents $\boldsymbol{u} = \tilde{\boldsymbol{u}}[\boldsymbol{x}, t]$, then $\boldsymbol{u}' = \tilde{\boldsymbol{u}}[\boldsymbol{x}', t]$, and the governing equation of motion for the PD bond-based model [35] can be written as the second-order in time partial integro-differential equation

$$\rho \ddot{\boldsymbol{u}}[\boldsymbol{x}, t] = \int\limits_{\mathbb{H}} \boldsymbol{f}[\boldsymbol{x}, \boldsymbol{x}', \boldsymbol{u}, \boldsymbol{u}', t]\ \mathrm{dV}' + \boldsymbol{b}[\boldsymbol{x}, t], \tag{4.1}$$

where ρ is the mass density of the continuum body (dot indicates derivative with respect to time), $\boldsymbol{f}$ is the so-called pairwise force field or force density which has dimensions of force per unit volume squared. All the constitutive informations of the model are hidden within the vector field $\boldsymbol{f}$. It can be observed that in equation (4.1) no spatial derivatives of the displacement field appear.

Since in this work we will be focusing on the static analysis of a peridynamic body, the dependance on t can be dropped, and the equation of motion can be specialised as

$$0 = \int_{\mathbb{H}} \boldsymbol{f}[\boldsymbol{x}, \boldsymbol{x}', \boldsymbol{u}, \boldsymbol{u}'] \, \mathrm{dV} + \boldsymbol{b}[\boldsymbol{x}]. \tag{4.2}$$

In bond-based peridynamics Newton's Third Law enforces an equilibrium condition on each pair of particles and thus the pairwise force field ($\boldsymbol{f}$) is antisymmetric with respect to particles switch, namely:

$$\boldsymbol{f}[\boldsymbol{x}, \boldsymbol{x}', \boldsymbol{u}, \boldsymbol{u}'] = -\boldsymbol{f}[\boldsymbol{x}', \boldsymbol{x}, \boldsymbol{u}', \boldsymbol{u}], \tag{4.3}$$

also called the linear admissibility condition. In more advanced formulations of peridynamics, i.e. *state-based* and *non-ordinary state based*, rather than asking for the equilibrium of each pair of particles $(\boldsymbol{x}, \boldsymbol{x}')$ individually, the global equilibrium of a particle $\boldsymbol{x}$ is enforced. This hypothesis frees from the limiting condition of forces of equal modulus and opposite direction (4.3) allowing for not equilibrated pair of forces (*state-based*) or even couples (*non-ordinary state based*).

Lastly, $\boldsymbol{b}$ collects the distributed external loads. Once the deforming body has been defined, $\mathbb{B}$, supplementary boundary conditions for equation (4.2) are necessary in order to find a solution; these are in the form:

$$\boldsymbol{u}[\bar{\boldsymbol{x}}] = \boldsymbol{u}_0, \tag{4.4}$$

where $\boldsymbol{x} = \bar{\boldsymbol{x}}$ for all the points belonging to the boundary $\partial\mathbb{B}$ of the analysed body $\mathbb{B}$.

Since the equation of motion is characterised by the absence of spatial derivatives, no restriction on the derivability of the fields in space is requested.

Equation (4.2) is the most general formulation for the bond-based peridynamic model as the pairwise force field, $\boldsymbol{f}$, is function of the displaced particles regardless of the type of motion they undergo. If the material is *microelastic* in the sense of Silling [35], it is assumed the existence of a potential energy, called *pairwise potential function* ω. Under this hypothesis what causes a variation in the pairwise force function is a change in the relative distance between material particles. If $\boldsymbol{x}$ is the position vector of a particle in the reference configuration, $\boldsymbol{x}'$ represents a particle in its family $\mathbb{H}[\boldsymbol{x}]$, then relative position vector is defined as

$$\boldsymbol{\xi} = \boldsymbol{x} - \boldsymbol{x}'. \tag{4.5}$$

Likewise, a relative displacement can be evaluated as

$$\boldsymbol{\eta} = \boldsymbol{u}[\boldsymbol{x}] - \boldsymbol{u}[\boldsymbol{x}'], \tag{4.6}$$

leading to

$$\boldsymbol{f}[\boldsymbol{x}, \boldsymbol{x}', \boldsymbol{u}, \boldsymbol{u}'] \to \boldsymbol{f}[\boldsymbol{\xi}, \boldsymbol{\eta}].$$

A costitutive relation for the definition of f has been proposed by many authors, starting from the microelastic case of Silling [35]. One of the simplest choices is the standard linear elastic perfectly brittle relation revisited by Zhou [161, 162],

$$f[\boldsymbol{\xi}, \boldsymbol{\eta}] = \mathbb{C}[\boldsymbol{\xi}]\, \boldsymbol{\eta} \cdot \mu[\boldsymbol{\eta}, \boldsymbol{\xi}]. \tag{4.7}$$

Here $\mathbb{C}$ is called the *micromodulus tensor*, a second-order tensor of the following form:

$$\mathbb{C}[\boldsymbol{\xi}] = c\, \frac{\boldsymbol{\xi} \otimes \boldsymbol{\xi}}{\sigma[\boldsymbol{\xi}]} \;, \tag{4.8}$$

where c is called the *bond constant* (a positive scalar quantity), and $\sigma[\boldsymbol{\xi}]$ is a function ensuring integrability of (4.7).

The function μ of equation (4.7) is a history-dependent scalar-valued function (also called *failure parameter*) which enforces bond breakage under tension only:

$$\mu[\boldsymbol{\eta}, \boldsymbol{\xi}] = \begin{cases} 1 & \text{for } s < s_{\mathrm{cr}} \\ 0 & \text{otherwise} \end{cases} \;, \tag{4.9}$$

where s stands for the bond elongation. Typically $s = \frac{|\boldsymbol{\xi}+\boldsymbol{\eta}|-|\boldsymbol{\xi}|}{|\boldsymbol{\xi}|}$, but in a linear setting it is reasonable to assume

$$s = \frac{\boldsymbol{\xi} \cdot \boldsymbol{\eta}}{|\boldsymbol{\xi}|^2}. \tag{4.10}$$

The linear elastic perfectly brittle costitutive model represented by equation (4.7) models a spring network system and is completely defined by only two parameters: the bond constant, which is related to the stiffness of each bond, and the critical stretch which limits the elongation of any bond. The former is the only elastic parameter involved, making the bond-based PD formulation a one-parameter elastic constitutive model; this is a major difference to local linear elasticity which depends on two material parameters (i.e. Young's Modulus and Poisson ratio). This reduction in the number of parameters of the PD formulation fixes Poisson ratio of modelled material at a value of $1/4$ for 3D of plane strain cases, or $1/3$ for the plane stress case. Solutions to the equilibrium problem of (4.2-4.4) in the peridynamic theory can be proven to be stationary points of the total potential energy under certain conditions [51]:

- the material assumed can be modelled with an elastic law;
- stationarity is measured with respect to incremental (even discontinuous) deformations.

In PD satisfying the equilibrium condition is sufficient for the stationarity of the potential energy. The total potential energy reads

$$\Pi[\boldsymbol{u}] = \frac{1}{2} \int_{\mathbb{B}} \int_{\mathbb{H}} \omega \, \mathrm{d}V' \mathrm{d}V - \int_{\mathbb{B}} \boldsymbol{b} \cdot \boldsymbol{u} \, \mathrm{d}V, \tag{4.11}$$

where for the case of a linear microelastic material, by virtue of (4.8), the *pairwise potential function* is

$$\omega[\boldsymbol{\xi},\boldsymbol{\eta}] = \int \boldsymbol{f}[\boldsymbol{\xi},\boldsymbol{\eta}] \cdot \mathrm{d}\boldsymbol{\eta} = \begin{cases} \frac{1}{2}\frac{c}{\sigma[\boldsymbol{\xi}]}(\boldsymbol{\xi}\cdot\boldsymbol{\eta})^2 & \text{for } s < s_{\mathrm{cr}} \\ \omega_{\mathrm{cr}} & \text{otherwise} \end{cases} . \tag{4.12}$$

The quantity ω_{cr} is the critical absorbed energy which amounts to the maximum energy a bond can store before breaking. More insight on the critical stretch and energy are given in the following (Section 4.3.2).
As stated by Zhou [161], additional conditions on $\sigma[\boldsymbol{\xi}]$,

$$\frac{|\boldsymbol{\xi}|^2}{\sigma[\boldsymbol{\xi}]} \geq p[\boldsymbol{\xi}], \quad c\int_{\mathcal{H}} \frac{|\boldsymbol{\xi}|^4}{\sigma[\boldsymbol{\xi}]}\mathrm{d}\boldsymbol{\xi} < \infty \tag{4.13}$$

are necessary to bound the stiffness and the energy respectively of the PD model to finite positive values by choosing a nonnegative $\mathrm{L}^1(\mathbb{H})$ function $p[\boldsymbol{\xi}]$. Essentially, equations (4.13) ask for positive definiteness of the micromodulus function and a bound for the energy associated to each bond. Silling's original microelastic model is retrieved by choosing $\sigma[\boldsymbol{\xi}] = |\boldsymbol{\xi}|^3$. The micromodulus, or rather the stiffness of the model resulting from a particular choice of the micromodulus, is shown in the Fig. 4.1 for σ chosen from a one-parameter family of functions.

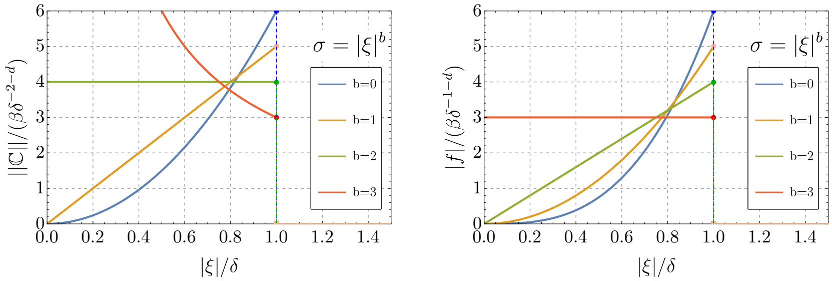

FIGURE 4.1: On the left, the shape of the micromodulus function for different σ; b is a scalar parameter; $\|\mathbb{C}\|$ is the norm of the micromodulus tensor, δ is the horizon, d is the dimension of the problem, β is a constant quantity expressing the proportionality between the bond constant c and the horizon. On the right, the force $|f|$ exerted by the bonds for increasing bond length. In the present paper only discontinuous micromodulus functions have been considered

4.3 A dimensionally-reduced model for thin plates

In the present work we propose a dimentionally-reduced model for the delamination of thin elements. In order to do so, certain assumptions must be made on the kinematics of the plate, and on the constitutive relation of the bond-based peridynamic continua.

4.3.1 Kinematics

Since fracture of a material can be seen as the birth and growth of a discontinuity in its displacement field, one can imagine the kinematics to be split into a continuous part, accounting for elastic deformations, and a jump part, accounting for the displacements due to the delamination:

$$\boldsymbol{u}[\boldsymbol{x}] = \boldsymbol{u}_a[\boldsymbol{x}] + \boldsymbol{u}_J[\boldsymbol{x}], \tag{4.14}$$

where the index a indicates the absolutely continuous part while the index J indicates the jump part. In this sense, it can be said that $\boldsymbol{u}$ belongs to the functional space of functions of Special Bounded Variations.
We restrict ourselves now to the study of thin bodies, $\mathbb{B}$, characterised by a constant thickness H. Given a region of the three-dimensional euclidean space $\mathbb{E}^3$, and a Cartesian reference frame (O, x_1, x_2, x_3), Figure 4.2, it is possible to assume the continuous part of the displacement as efficiently approximated by a polynomial expansion of the sort

$$\boldsymbol{u}_a[\boldsymbol{x}] \approx \boldsymbol{\mathcal{A}}[x_1, x_2] + \boldsymbol{\mathcal{B}}[x_1, x_2]x_3 + \cdots \quad . \tag{4.15}$$

Such expansion my or may not refer to a Taylor series. It is important to highlight that the choice of the reduction plane (the expansion point in the series expansion) can have effects on the hierarchical distribution of terms in the reduced formulation ([65]); in the following we will choose the mid-plane of the plate so to adapt to classical local elastic reduced formulations.

The jump part of the displacement field, which represents delamination occurring through the thickness, will be defined in a rather general way as

$$\boldsymbol{u}_J[\boldsymbol{x}] = \boldsymbol{j}[x_1, x_2]\, \Theta(x_3 - h[x_1, x_2]), \tag{4.16}$$

where the $h[x_1, x_2]$ is the delamination function, defining the surface on which a displacement discontinuity may arise, while Θ is the heaviside function; lastly, $\boldsymbol{j}[x_1, x_2]$ is the vector function defining the jump itself. Mixed mode fracture processes are allowed by the ansatz made on $\boldsymbol{u}_J$. Due to the kinematic split imposed in equation (4.14), the relative displacement field now reads:

$$\boldsymbol{\eta} = \boldsymbol{\eta}_a + \boldsymbol{\eta}_J. \tag{4.17}$$

4.3.2 Damage

It is important to highlight that in nonlocal theories a discontinuity in the displacement field does not necessarily mean fracture nucleation/propagation. In fact, in the peridynamic theory of continuum mechanics particles that are already separated by a finite distance can very well withstand a jump in

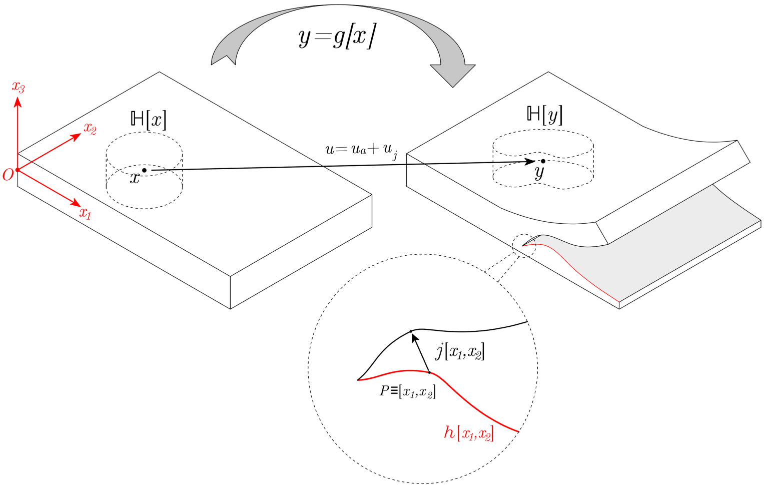

FIGURE 4.2: Deformation map $g(\boldsymbol{x})$ for a plate of thickness H undergoing delamination. Each point $P \equiv [x_1, x_2]$ of the reference configuration lying on the delamination surface jump to a new position specified by the vector $\boldsymbol{j}[P]$.

their relative displacement. What ensure the effective birth of a delamination surface is the η function (4.9) which represents the failure criterion for the bonds. The state of interaction can be determined by means of equation (4.9), which enforces a critical stretch condition ($s < s_{\mathrm{cr}}$). In many other cases present in the literature, instead of a critical elongation crisis criterion, an energy-based one is employed [163–165]. The energy-based criterion attributes the breakage of a bond to the reach of a limit quantity in the stored energy, called critical bond energy ω_{cr}. Both the critical stretch and critical energy can be evaluated by means of an energy comparison with standard local theory of fracture mechanics. In particular, the PD energy necessary for the growth of a new surface in the body is imposed to be equal to the critical energy release rate of Griffith type [151]. The energy necessary for the growth of a surface in the PD body is the energy that is required to break all the bonds which pass through that particular surface, see Figure 4.3. In this fashion, for the case of the critical stretch, one obtains [64, 166]

$$s_{cr} = \sqrt{\frac{G_c}{\beta[\mathbb{H}, \sigma]\ \delta}} \tag{4.18}$$

where G_c is the critical energy release rate of Griffith fracture mechanics.

4.3.3 Lagrangian formulation

It has been proven that, like in local elasticity, the PD equilibrium equation coincides with the Euler-Lagrange equations for the total Lagrangian. The

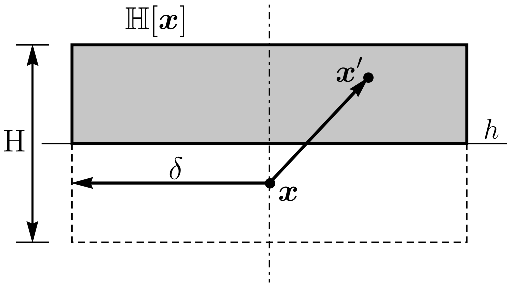

FIGURE 4.3: Computation of the total energy necessary to break all the bonds connecting the material point $\boldsymbol{x}$ with those $\boldsymbol{x}'$ on the other side of the fracture surface h.

solution of the equilibrium problem of the nonlocal PD body can thus be seen as stationary points of the PD lagrangian:

$$\mathcal{L} = \mathcal{K} - \mathcal{E}_{el} + \mathcal{W}, \tag{4.19}$$

where $\mathcal{E}_{el}$ is the elastic energy, $\mathcal{K}$ is the kinetic energy, and $\mathcal{W}$ is the work of the external loads. By explicitly expressing the various terms, and by neglecting the kinetic energy due to the static assumption, equation (4.19) becomes

$$\mathcal{L} = -\frac{1}{2}\int_{\mathbb{B}}\int_{\mathbb{H}} \omega[\boldsymbol{\xi},\boldsymbol{\eta}]\,\mathrm{dV}'\mathrm{dV} + \int_{\mathbb{B}} \boldsymbol{b}\cdot\boldsymbol{u}\,\mathrm{dV}. \tag{4.20}$$

Equation (4.20) is characterised by the absence of spatial derivatives for the displacement field.

The lagrangian formulation for the dimensionally-reduced problem is obtained by means of a through-thickness integration. By assuming the cartesian product $\mathbb{B} = \mathbb{B}_\alpha \times \mathbb{B}_3$ to hold, where

$$\mathbb{B}_\alpha := \left\{(x_1, x_2),\ \forall \boldsymbol{x}, \boldsymbol{x}' \in \mathbb{B}\right\};\quad \mathbb{B}_3 := \left\{x_3,\ \forall \boldsymbol{x}, \boldsymbol{x}' \in \mathbb{B}\right\} \tag{4.21}$$

one can write

$$\mathcal{L} = \int_{\mathbb{B}_\alpha} \Lambda[x_1, x_2, \boldsymbol{u}]\mathrm{dS}_\alpha. \tag{4.22}$$

Here

$$\Lambda[x_1, x_2, \boldsymbol{u}] = -\Lambda_{\mathcal{E}} + \Lambda_{\mathcal{W}} = -\frac{1}{2}\int_{\mathbb{H}}\int_{\mathbb{B}_3} \omega[\boldsymbol{\xi},\boldsymbol{\eta}]\,\mathrm{d}x_3\mathrm{dV}' + \int_{\mathbb{B}_3} \boldsymbol{b}\cdot\boldsymbol{u}\,\mathrm{d}x_3. \tag{4.23}$$

All the functionals involved here (4.22) are nonlocal, in the sense that the unknown function $\boldsymbol{u}$ is evaluated at different points of the body. An equivalent form of the Euler-Lagrange equation for nonlocal functionals is now necessary to find the stationary points of (4.22). The research of stationarity points, and more generally, minimizing functions for nonlocal functionals has been investigated [167, 168]; for the particular case of the static PD nonlocal functional [169–171] one has

$$\min_u \mathcal{L} \to 2\frac{\partial \Lambda_{\mathcal{E}}}{\partial \boldsymbol{q}} - \frac{\partial \Lambda_{\mathcal{W}}}{\partial \boldsymbol{q}} = 0, \tag{4.24}$$

where the $\boldsymbol{q}$ is the vector of the unknown functions of the problem, namely for a linear approximation of the continuous part of the displacement

$$\boldsymbol{q} = \{h[x_1, x_2], \boldsymbol{j}[x_1, x_2], \boldsymbol{\mathcal{A}}[x_1, x_2], \boldsymbol{\mathcal{B}}[x_1, x_2]\}.$$

In order to retrieve equation (4.24) the linear admissibility condition (4.3) must be enforced on the results of [169–171].

4.3.4 Hierarchical form of the reduced pairwise potential function

The reduced form of the Lagrangian is not easily obtained for a general PD costitutive law, nonetheless once certain conditions on the micromodulus tensor $\mathbb{C}$ are met, the integration through the thickness of the pairwise potential function,

$$\Lambda_{\mathcal{E}} = \int_{\mathbb{B}_\alpha} \int_{-\frac{H}{2}}^{\frac{H}{2}} \int_{-\frac{H}{2}}^{\frac{H}{2}} \omega[\boldsymbol{\xi}, \boldsymbol{\eta}] \, \mathrm{d}x_3 \mathrm{d}x_3' \, \mathrm{dS}_\alpha, \tag{4.25}$$

becomes feasible. Here, ω is that of equation (4.12) and $\mathbb{B}_\alpha$ is the region defined in (4.21). For the linear elastic case the influence of the function σ and thus of the shape of the micromodulus function, equation (4.8), on the overall behaviour has been investigated in [172]. Since it was shown that the rate of convergence is not sensitive to the micromodulus function shape, in the present work, the choice of $\sigma = 1$ has been made. Integration of equation (4.25) through the thickness is not immediate due to the hidden presence of the failure parameter μ which introduces nonlinearity in the PD model. Neglecting the failure parameter allows to evaluate the reduced form of the energy for the fully elastic case, i.e. when the load as yet to break any bond. If ω_{red} is the result of the double integration through the thickness of equation (4.25), by $\omega_{\text{red},a}$ and $\omega_{\text{red},J}$ we refer to the part associated to the continuous displacement field and to the jump field respectively:

$$
\begin{aligned}
\frac{\omega_{\mathrm{red,a}}}{c} = \; & \tfrac{1}{2}\mathrm{H}^2\left(x_1'-x_1\right)^2\left(\mathcal{A}_1[x_1']-\mathcal{A}_1[x_1]\right)^2+ \\
& \tfrac{1}{48}\mathrm{H}^4\big(x'^2\mathcal{B}_1[x_1]^2+x'^2\mathcal{B}_1(x')^2+2x'\mathcal{A}_3(x')\mathcal{B}_1(x')+2x'\mathcal{A}_1(x')\mathcal{B}_3(x')+2\mathcal{A}_3(x')^2+ \\
& \quad +x^2\mathcal{B}_1(x')^2-2x\mathcal{A}_3(x')\mathcal{B}_1(x')+2x'\mathcal{A}_3(x')\mathcal{B}_1[x_1]-2x\mathcal{A}_3(x')\mathcal{B}_1[x_1]+ \\
& \quad -2x'\mathcal{B}_1(x')\mathcal{A}_3[x_1]+2x\mathcal{B}_1(x')\mathcal{A}_3[x_1]-2x'\mathcal{A}_3[x_1]\mathcal{B}_1[x_1]-2x\mathcal{A}_1(x')\mathcal{B}_3(x')+ \\
& \quad -2x'\mathcal{B}_3(x')\mathcal{A}_1[x_1]+2x\mathcal{B}_3(x')\mathcal{A}_1[x_1]+2x'\mathcal{A}_1(x')\mathcal{B}_3[x_1]-2x\mathcal{A}_1(x')\mathcal{B}_3[x_1]+ \\
& \quad -2x'\mathcal{A}_1[x_1]\mathcal{B}_3[x_1]-4\mathcal{A}_3(x')\mathcal{A}_3[x_1]-2x'x\mathcal{B}_1(x')^2-2x'x\mathcal{B}_1[x_1]^2+x^2\mathcal{B}_1[x_1]^2+ \\
& \quad +2x\mathcal{A}_3[x_1]\mathcal{B}_1[x_1]+2x\mathcal{A}_1[x_1]\mathcal{B}_3[x_1]+2\mathcal{A}_3[x_1]^2\big) \\
& \tfrac{1}{1440}\mathrm{H}^6\left(10\mathcal{B}_3(x')\mathcal{B}_3[x_1]+7\mathcal{B}_3(x')^2+7\mathcal{B}_3[x_1]^2\right),
\end{aligned}
\tag{4.26}
$$

$$
\begin{aligned}
\frac{\omega_{\mathrm{red,J}}}{c} = \; & -\tfrac{1}{6}j[x_1']j[x_1]h[x_1']h[x_1]\left(2h[x_1']^2-3h[x_1']h[x_1]+2h[x_1]^2\right)+ \\
& \mathrm{H}\big(-\tfrac{1}{3}j[x_1']\mathcal{A}_3[x_1']h[x_1']^3-\tfrac{1}{6}j[x_1']^2h[x_1']^3+\tfrac{1}{3}j[x_1']h[x_1']^3\mathcal{A}_3[x_1]-\tfrac{1}{6}j[x_1]^2h[x_1]^3+ \\
& \quad +\tfrac{1}{2}j[x_1']\mathcal{A}_1[x_1']h[x_1']^2(x-x_1')+\tfrac{1}{2}j[x_1']h[x_1']^2(x_1'-x)\mathcal{A}_1[x_1]-\tfrac{1}{4}j[x_1]h[x_1]^4\mathcal{B}_3[x_1]+ \\
& \quad +\tfrac{1}{2}j[x_1]\mathcal{A}_1[x_1'](x-x_1')h[x_1]^2+\tfrac{1}{2}j[x_1](x_1'-x)\mathcal{A}_1[x_1]h[x_1]^2+\tfrac{1}{3}j[x_1]\mathcal{A}_3[x_1']h[x_1]^3+ \\
& \quad +\tfrac{1}{6}j[x_1']j[x_1]h[x_1']^3+\tfrac{1}{6}j[x_1']j[x_1]h[x_1]^3+\tfrac{1}{3}j[x_1']h[x_1']^3(x-x_1')\mathcal{B}_1[x_1']+ \\
& \quad -\tfrac{1}{4}j[x_1']h[x_1']^4\mathcal{B}_3[x_1']-\tfrac{1}{3}j[x_1]\mathcal{A}_3[x_1]h[x_1]^3+\tfrac{1}{3}j[x_1](x_1'-x)h[x_1]^3\mathcal{B}_1[x_1]\big) \\
& \mathrm{H}^2\left(-\tfrac{1}{8}j[x_1']j[x_1]\left(h[x_1']^2+h[x_1]^2\right)\right)+ \\
& \mathrm{H}^3\big(-\tfrac{1}{12}j[x_1']\mathcal{A}_3[x_1']h[x_1']-\tfrac{1}{24}j[x_1']^2h[x_1']+\tfrac{1}{12}j[x_1']h[x_1']\mathcal{A}_3[x_1]+\tfrac{1}{12}j[x_1]\mathcal{A}_3[x_1']h[x_1]+ \\
& \quad -\tfrac{1}{12}j[x_1]\mathcal{A}_3[x_1]h[x_1]+\tfrac{1}{8}j[x_1']\mathcal{A}_1[x_1'](x_1'-x)+\tfrac{1}{8}j[x_1'](x-x_1')\mathcal{A}_1[x_1]-\tfrac{1}{24}j[x_1]^2h[x_1]+ \\
& \quad +\tfrac{1}{8}j[x_1](x-x_1')\mathcal{A}_1[x_1]+\tfrac{1}{12}j[x_1](x_1'-x)\mathcal{B}_1[x_1']h[x_1]+\tfrac{1}{12}j[x_1']h[x_1'](x-x_1')\mathcal{B}_1[x_1]+ \\
& \quad +\tfrac{1}{24}j[x_1']j[x_1]h[x_1]-\tfrac{1}{12}j[x_1']h[x_1']^2\mathcal{B}_3[x_1]+\tfrac{1}{24}j[x_1']j[x_1]h[x_1']-\tfrac{1}{12}j[x_1]\mathcal{B}_3[x_1']h[x_1]^2+ \\
& \quad -\tfrac{1}{24}j[x_1']h[x_1']^2\mathcal{B}_3[x_1']-\tfrac{1}{24}j[x_1]h[x_1]^2\mathcal{B}_3[x_1]+\tfrac{1}{8}j[x_1]\mathcal{A}_1[x_1'](x_1'-x)\big) \\
& \mathrm{H}^4\big(\tfrac{1}{12}j[x_1']\mathcal{A}_3[x_1']-\tfrac{1}{12}j[x_1']\mathcal{A}_3[x_1]-\tfrac{1}{12}j[x_1]\mathcal{A}_3[x_1']+\tfrac{1}{24}j[x_1'](x_1'-x)\mathcal{B}_1[x_1']+ \\
& \quad +\tfrac{1}{24}j[x_1](x-x_1')\mathcal{B}_1[x_1]-\tfrac{1}{96}j[x_1']j[x_1]+\frac{j[x_1']^2}{24}+\tfrac{1}{12}j[x_1]\mathcal{A}_3[x_1]+\tfrac{1}{24}j[x_1]^2+ \\
& \quad +\tfrac{1}{24}j[x_1'](x_1'-x)\mathcal{B}_1[x_1]+\tfrac{1}{24}j[x_1](x-x_1')\mathcal{B}_1[x_1']\big) \\
& \mathrm{H}^5\left(\tfrac{1}{48}j[x_1]\mathcal{B}_3[x_1']+\tfrac{1}{48}j[x_1']\mathcal{B}_3[x_1]+\tfrac{5}{192}j[x_1']\mathcal{B}_3[x_1']+\tfrac{5}{192}j[x_1]\mathcal{B}_3[x_1]\right).
\end{aligned}
\tag{4.27}
$$

Clearly $\omega_{\mathrm{red}} = \omega_{\mathrm{red,a}} + \omega_{\mathrm{red,J}}$. Equations (4.27-4.28) have been specialised for the plane strain case in order to appreciate better the contributions of the various terms of the displacement field. The variables x_1 and x_1' represent respectively the in-plane component of the position vector for particle $\boldsymbol{x}$ and $\boldsymbol{x}'$. Furthermore, we have used $\boldsymbol{\mathcal{A}} = \{\mathcal{A}_1, \mathcal{A}_3\}$, $\boldsymbol{\mathcal{B}} = \{\mathcal{B}_1, \mathcal{B}_3\}$ and $\boldsymbol{j} = \{0, j_3\}$. The latter limits the kinematics to that of a pure Mode-I delamination.

It is possible to see how the dimensional reduction of the pairwise potential function generates a hierarchy of terms characterizing the strain energy stored inside the planar element. These terms have an immediate physical interpretation, especially those related to the continuous part of the displacement field $\omega_{red,a}$. In fact, since $\mathcal{A}_1[x]$ is the in-plane component of the

displacement field for the points on the reduction plane, the term scaling with H^2 of $\omega_{red,a}$ can be regarded as purely membrane. In the higher order term, such as H^4, one can assess the presence of purely bending contributions (for example, those depending solely on $\mathcal{B}_1[x']^2$), but also of mixed ones. The mixed terms introduce coupling of membrane behaviour and bending behaviour. This is a unique feature of the nonlocal formulation, which is typically not present in linear model of plates for local elasticity. Lastly, the terms scaling with H^6 are higher oder terms depending only on $\mathcal{B}_3[x_1]$ which is the nonlocal equivalent of a local strain deformation through the thickness ($\partial_{x_3}(\boldsymbol{u}_a \cdot \boldsymbol{e}_3) \approx 0$, where $\boldsymbol{e}_3$ is the unit vector normal to the plane (x_1, x_2)). In models such as the Kirchhoff plate, $\mathcal{B}_3[x_1]$ is null.
The contribution of the jump part of the displacement field on the reduced energy, reflected in $\omega_{red,J}$ is more scattered. We see contribution of the jump field to both membrane, mixed and bending related quantities. Here, again, coupling occurs between the different fields of the jump part of the displacement and the continuous part. The highest order term in the thickness (H) is determined by the order of the truncation in the Taylor expansion of the continuous part of the displacement. By retaining only terms up to the first order in x_3, the highest power becomes 6. This particular choice was made in order to check the convergence of the nonlocal model, which will be done in the last section of this paper.
Under the aforementioned conditions the solution for the Euler-Lagrange system of equations (4.24) of the PD model was achieved by using a Galerkin approach, resulting in a system of the kind

$$\int_{\mathcal{B}_\alpha} \left(2\frac{\partial \Lambda_{\mathcal{E}}}{\partial \boldsymbol{q}} - \frac{\partial \Lambda_{\mathcal{W}}}{\partial \boldsymbol{q}} \right) \delta \boldsymbol{q} = 0. \tag{4.28}$$

System (4.28) was then solved iteratively. We will present in the following section the analytical solution and numerical validation for the case of a clamped cantilever under bending.

4.3.5 A comparison with numerical results

In order to compare and validate the semi-analytical scheme presented, a numerical algorithm was designed using Ansys. Several authors [68] put forward solutions for the FEM analysis of bond-based PD solids. Most of these are meshfree schemes where material particles (nodes) are physically connected through links. The elastic and post-elastic behaviour of the links depends on the constitutive law of the bond-based formulation. In the elastic regime the energy stored by a link $\mathcal{E}$, inclined by α connecting the couple of particles $\{\boldsymbol{x}, \boldsymbol{x}'\}$ each associated with a discretised volume V or V', can be approximated for small enough V and V' to

$$\mathcal{E}[\boldsymbol{x}, \boldsymbol{x}'] = \frac{1}{2} \int_V \int_{V'} \mathbb{C}\boldsymbol{v} \cdot \boldsymbol{v} \, \mathrm{dVdV'} \approx \frac{v^2}{2} \frac{c}{\sigma[|\boldsymbol{\xi}|]} |\boldsymbol{\xi}|^2 \cos^2[\alpha - \beta] \mathrm{VV'}, \tag{4.29}$$

which resembles the energy of a truss connecting the couple of points $\{\boldsymbol{x}, \boldsymbol{x}'\}$ and subjected to a concentrated force acting with an inclination β in $\boldsymbol{x}'$, $k_i\, v^2 \cos^2[\alpha - \beta]/2$. Therefore,

$$k_i = \frac{1}{2}\frac{c}{\sigma[|\boldsymbol{\xi}|]}|\boldsymbol{\xi}|^2\, \mathrm{V}\mathrm{V}', \tag{4.30}$$

and the link between particles can be efficiently approximated by a truss (Figure 4.4).

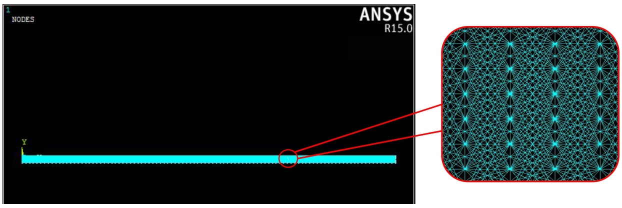

FIGURE 4.4: Side-view of a clamped plate implemented in ANSYS. Bonds have been modeled as trusses.

The case of a bent cantilever. We prove the coherence of the numerical scheme and the analytical solution of the lagrangian formulation by testing the behaviour of a cantilever plate subjected to couples at the free edge, as shown in Figure 4.5. Nonlocal and local parameters are reported in the following (Table 4.1). The test is a force-induced test, where the acting couples have been pushed up to a value of M_{max} corresponding to a curvature of the free-edge section of $\chi_{max} = 1.23\text{E} - 04/L$, where L stands for the length of the plate.

Mechanical and geometric quantities	**Value**
Young's Modulus [MPa]	5000
Critical surface energy G_c [J/m^2]	5.3
Thickness over length (H/L)	1/25
Nonlocal parameters	**Value**
Horizon(δ)/Length(L)	1/5
Bond constant c [N/mm^6]	0.5
Critical stretch s_{cr} [-]	0.01

TABLE 4.1: Parameters of the local equivalent material and geometry of the plate (up); nonlocal parameter of the peridynamic bond-based reduced model (down).

The numerical and analytical solutions are obtained independently, in fact, the foundations of the numerical scheme adopted here are those typical of bond-based peridynamics applications in the FEM framework [68]. On the contrary, the analytical model was subjected to the limitations of the presented theory. Nonetheless, one can see from Figure (4.5) a very close behaviour for the two different solutions.

As one would expect the plate shows a delamination surface originating from the free end of the plate and moving towards the clamped end (Figure 4.6) progressively as the load is increased past the "elbow" point in the moment-curvature plot (Figure 4.5). The nucleation and subsequent growth of the crack front leads to a concentration of the deformation in the proximity of the delamination surface. We remark that a discontinuity in the displacement field does not mean bond breakage; hence, we see the birth of a more damaged zone from which we can expect the crack to propagate.

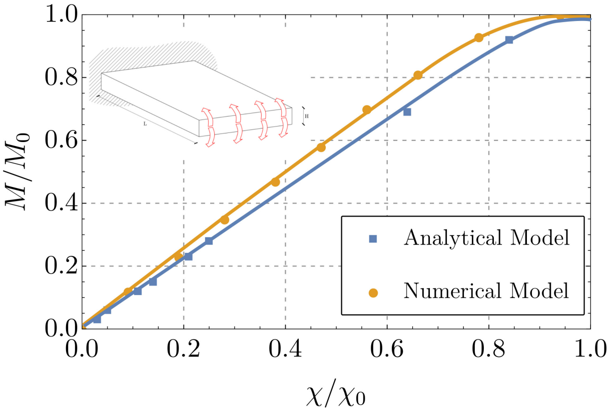

FIGURE 4.5: Comparison between numerical and analytical model of a clamped plate subjected to two opposite couples acting on the free end.

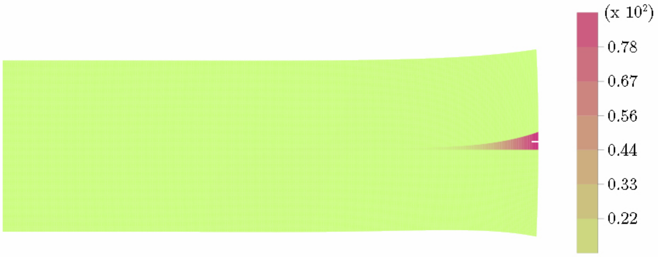

FIGURE 4.6: Post-elastic behaviour of the analytical model showing normalised average strain (average strain devided by maximum average strain in the body) upon crack nucleation for the chosen load distribution. The displacement of the configuration are scaled by a factor of 100 in order to make the deformed shape appreciable.

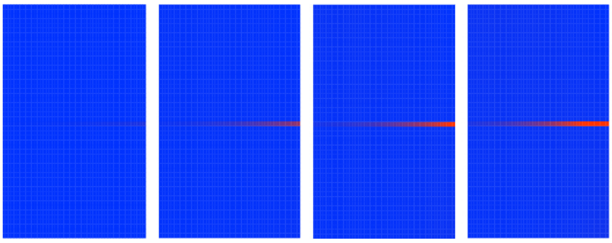

FIGURE 4.7: Evolution of crack surface (in red) from undamaged beam (left) to damaged one (right).

4.4 Convergence to a local elastic model

Convergence of the proposed PD model to local elasticity is assured for the continuous part of the displacement field only [173–175]. Nonetheless, with an appropriate scaling of the jump field functions the so called "localization" becomes feasible.

By applying (4.17) to (4.12), the first term of (4.20), which is the elastic energy of a bond-based PD body, becomes

$$\frac{1}{4}\int\limits_{\mathbb{B}}\int\limits_{\mathbb{H}} \mu\mathbb{C}\,\boldsymbol{\eta}_a\cdot\boldsymbol{\eta}_a \mathrm{d}V'\mathrm{d}V + \frac{1}{4}\int\limits_{\mathbb{B}}\int\limits_{\mathbb{H}} \mu\mathbb{C}\,\boldsymbol{\eta}_a\cdot\boldsymbol{\eta}_J \mathrm{d}V'\mathrm{d}V + \frac{1}{4}\int\limits_{\mathbb{B}}\int\limits_{\mathbb{H}} \mu\mathbb{C}\,\boldsymbol{\eta}_J\cdot\boldsymbol{\eta}_J \mathrm{d}V'\mathrm{d}V. \tag{4.31}$$

To ensure convergence for vanishing nonlocality, i.e. $\delta \rightarrow 0$, the scaling of each term must be checked.

4.4.1 Peridynamic parameter evaluation

The model of an isotropic homogeneous linear elastic material in the bond-based peridynamic theory is characterised by one single constant, called the bond constant c. This constant is typically defined by means of an energetic equivalence with standard local elastic material. It has huge effects on the value of this constant the deformation map imposed for the equivalence, i.e. isotropic expansion, pure elongation or even shear. The energy obtained after the convergence to the local model is, in fact, affected by the choice of the bond constant to the point that certain terms can converge to classical ones typical of local theories while others may not. For example, if one were to make the choice of imposing equivalence of the stretching energy in the peridynamic model and in the local elastic one, only first order terms in H of the localized PD model would converge while quadratic, cubic and higher order ones would not.

In the following, for the evaluation of the bond constant, a relatively common and general hypothesis of isotropic expansion is made. This choice is not expected to make all the terms converge to the classical ones, but it can give a rough idea of the possibilities of the model obtained by the convergence. The energy density for a bond-based PD linear elastic material under isotropic expansion ($\boldsymbol{\eta} = \alpha\boldsymbol{\xi}$) is defined as

$$W_{PD} = \frac{1}{2}c\alpha^2 \int\limits_{\mathbb{H}} |\boldsymbol{\xi}|^{4-b}\mathrm{dV} = \frac{1}{2}c\alpha^2\, \gamma[\mathbb{H}, b, d]\, \delta^{4-b+d}, \tag{4.32}$$

where γ is a scalar function which depends on the shape of the family $\mathbb{H}$, the dimension of the problem d, and the parameter b which comes from the choice of $\sigma[|\boldsymbol{\xi}|] = |\boldsymbol{\xi}|^b$. Likewise, the energy of an isotropic expanding linear elastic material in classic local elasticity is defined as

$$W_{CL} = \frac{1}{2}\alpha^2\, \boldsymbol{I}\cdot\mathbb{E}[\boldsymbol{I}] = \frac{1}{2}\alpha^2\frac{3\mathrm{E}}{1-2\nu}, \tag{4.33}$$

where $\boldsymbol{I}$ is the identity tensor, while $\mathbb{E}$ is the fourth-order elasticity tensor, E is the Young's modulus of the local elastic material and ν is Poisson ratio. The value of Poisson ratio ν for a bond-based material is fixed to $1/4$ or $1/3$ depending on the dimension of the problem.
By enforcing equivalence between the energies (4.32) and (4.33) one retrieves

$$c = \frac{3\mathrm{E}}{\gamma[b]\, \delta^{4-b+d}(1-2\nu)}. \tag{4.34}$$

For the case of a spherical horizon one obtains

$$c = \frac{15\,\mathrm{E}}{56\,\delta^6}. \tag{4.35}$$

According to (4.34), the scaling of the bond constant is then defined as $c \sim \delta^{b-4-d}$.

4.4.2 Displacement scaling

The continuous part of the energy (first term of equation (4.31)) is found to be scaling as

$$\int\limits_{\mathbb{B}}\int\limits_{\mathbb{H}} \frac{c}{|\boldsymbol{\xi}|^b}(\boldsymbol{\xi}\cdot\boldsymbol{\eta}_a)^2\mathrm{dVdV'} \sim \delta^{b-4-d-b+2+2m+d} = \delta^{2m-2}, \tag{4.36}$$

since the scaling of c is defined in (4.35), and the other terms scale as follow: $|\boldsymbol{\xi}| \sim \delta$; $|\boldsymbol{\eta}| \sim \delta^m$; $V' \sim \delta^d$. For the integral term to stay bounded and nonvanishing one requires $m = 1$.
Hence, $\boldsymbol{\eta}_a \sim \delta^1$, which means that

$$\boldsymbol{\eta}_a \approx \nabla_{\boldsymbol{x}}\boldsymbol{\mathcal{A}}[x_1, x_2]\, \boldsymbol{\xi} + \nabla_{\boldsymbol{x}}\boldsymbol{\mathcal{B}}[x_1, x_2]\boldsymbol{\xi}\, x_3 + \boldsymbol{\mathcal{B}}[x_1, x_2]\, \boldsymbol{\xi}\cdot\boldsymbol{e}_3 + \cdots \tag{4.37}$$

defines the scaling of the shape functions, since $\boldsymbol{\xi} \sim \delta^1$. In particular, no scaling is required

$$\nabla_{\boldsymbol{x}}\boldsymbol{\mathcal{A}}[x_1, x_2] \sim \delta^0 \quad , \quad \nabla_{\boldsymbol{x}}\boldsymbol{\mathcal{B}}[x_1, x_2] \sim \delta^0 \quad , \quad \boldsymbol{\mathcal{B}}[x_1, x_2] \sim \delta^0. \tag{4.38}$$

In a similar fashion, the second term of (4.31) must follow the following scalings:

$$\int_{\mathbb{B}}\int_{\mathbb{H}} \frac{c}{|\boldsymbol{\xi}|^b}(\boldsymbol{\xi}\cdot\boldsymbol{\eta}_J)(\boldsymbol{\xi}\cdot\boldsymbol{\eta}_a)\mathrm{dVdV'} \sim \delta^{b-4-d-b+2+m+n+d} = \delta^{-2+m+n}. \tag{4.39}$$

In order for the energy to stay bounded the scaling of the jump part of the displacement field (defined by n) must fulfil the condition of $n \geq 1$, since from (4.36) $m = 1$. Accordingly, from the last term of the energy one obtains:

$$\int_{\mathbb{B}}\int_{\mathbb{H}} \frac{c}{|\boldsymbol{\xi}|^b}(\boldsymbol{\xi}\cdot\boldsymbol{\eta}_J)^2\mathrm{dVdV'} \sim \delta^{b-4-d-b+2+2n+d} = \delta^{-2+2n}, \tag{4.40}$$

which gives the redundant condition: $n \geq 1$. In view of (4.16) and for vanishing nonlocality one can approximate the relative jump displacement $\boldsymbol{\eta}_J$ as

$$\boldsymbol{\eta}_J \approx \nabla_{\boldsymbol{\xi}}\boldsymbol{u}'_J\Big|_{\boldsymbol{\xi}=0}\cdot\boldsymbol{\xi}, \tag{4.41}$$

where $\boldsymbol{u}'_J$ is the displacement of the particle $\boldsymbol{x}'$. If we call p the scaling of $\nabla_{\boldsymbol{\xi}}\boldsymbol{u}'_J$ then by virtue of (4.40), $p \geq 0$. Though, since

$$\nabla_{\boldsymbol{x}}\,\boldsymbol{u}'_J\Big|_{\boldsymbol{\xi}=0} = \nabla_{\boldsymbol{x}}\boldsymbol{j}\;\Theta(x_3 - h[x_1,x_2]) + \boldsymbol{j}\otimes(\boldsymbol{e}_3 - \nabla_{\boldsymbol{x}}h)\;\phi(x_3 - h[x_1,x_2]), \tag{4.42}$$

where ϕ is the Dirac delta distribution, one can easily assess that in order for $h[x_1,x_2]$ and the energy to be bounded, the following scalings must hold

$$\nabla_{\boldsymbol{x}}\boldsymbol{j} \sim \delta^0 \;\;,\;\; \boldsymbol{j} \sim \delta^0 \;\;,\;\; \nabla_{\boldsymbol{x}}h \sim \delta^0. \tag{4.43}$$

4.4.3 The scaling of the crisis criterion

Alongside the energy, the damage criterion ($s < s_{\mathrm{cr}}$) must scale too as $\delta \to 0$. The scaling of the critical stretch s_{cr} is defined by equation (4.18), so $s_{\mathrm{cr}} \sim \delta^{-1/2}$. On the other hand, the scaling of the stretch s is defined from equation (4.10):

$$s \sim \delta^0 \tag{4.44}$$

Clearly, this condition depends on the fact that in the previous section we asked the energy to be bounded. In fact, by comparing equations (4.10) and (4.12) for $\sigma[\boldsymbol{\xi}] = |\boldsymbol{\xi}|^b$, one can write

$$\omega = \frac{1}{2}cs^2\;|\boldsymbol{\xi}|^{4-b}. \tag{4.45}$$

Since the pairwise potential energy ω must scale as δ^{-d} for the whole energy to be bounded, and the scalings of all the other quantities in equation (4.45) has been defined, then it becomes straight-forward to check that the scaling of s is that of equation (4.44).

It would thus seem that under these conditions for vanishing horizon δ, whenever the stretch is bounded no failure can occur as the critical stretch is growing indefinitely ($s_{cr} \to \infty$ while s is finite).
In the limit of small enough δ by employing equations (4.41) and (4.42)

$$s = \frac{\xi \cdot \nabla_{\xi} \boldsymbol{u}'_J\Big|_{\xi=0} \cdot \xi}{|\xi|^2} = \nabla_{\xi} \boldsymbol{u}'_J\Big|_{\xi=0} : \frac{\xi \otimes \xi}{|\xi|^2}. \tag{4.46}$$

The second tensor in the double dot product[1] is a quantity that scales as δ^0 whereas the first tensor harbours a singularity, the Dirac's Delta function ϕ, which for $x_3 = h[x_1, x_2]$ makes the stretch infinite. Hence, whenever on the delamination surface, the criterion is immediately not satisfied. Finally:

$$s < s_{\text{cr}} \to \begin{cases} \text{False} & \text{for } x_3 = h[x_1, x_2] \\ \text{True} & \text{otherwise} \end{cases} . \tag{4.47}$$

4.4.4 Localised energy in plane strain

Localisation of the PD non local model has been obtained by means of a limit operation, for vanishing δ, on the PD nonlocal elastic energy. The localised energy is composed of a part entirely defined by the continuous part of the displacement field, term (4.36), and a part composed by mix and purely jump terms

$$\mathcal{E}_{local} = \mathcal{E}_{local,a} + \mathcal{E}_{local,J}, \tag{4.48}$$

where for the assumption of continuous displacement field (4.15) truncated at first order in x_3, and plane strain

$$\begin{aligned} \mathcal{E}_{local,a} =& \text{HE}\left(\frac{3}{56}\mathcal{A}_1'[x_1]^2 + \frac{5}{84}\mathcal{B}_3[x_1]\mathcal{A}_1'[x_1] + \frac{5}{168}\mathcal{A}_3'[x_1]^2 + \right. \\ & \left. \frac{5}{84}\mathcal{B}_1[x_1]\mathcal{A}_3'[x_1] + \frac{5}{168}\mathcal{B}_1[x_1]^2 + \frac{3}{56}\mathcal{B}_3[x_1]^2\right) + \\ & \text{H}^3\text{E}\left(\frac{1}{224}\mathcal{B}_1'[x_1]^2 + \frac{5\mathcal{B}_3'[x_1]^2}{2016}\right). \end{aligned} \tag{4.49}$$

---

[1] Given two tensors A and B we mean by double dot product the operation $\text{A:B}^T = \text{Tr(AB)} = A_{ij}B_{ji}$.

Here $\boldsymbol{\mathcal{A}} = \{\mathcal{A}_1, \mathcal{A}_3\}$, $\boldsymbol{\mathcal{B}} = \{\mathcal{B}_1, \mathcal{B}_3\}$ and the primes indicates derivative with respect to x_1. Meanwhile,

$$\begin{aligned}
\mathcal{E}_{local,J} = \quad & \mathrm{HE}\left(\frac{5}{168}\mathcal{B}_1[x_1]j_3'[x_1] + \frac{5}{336}j_3'[x_1]^2 + \frac{5}{168}j_3'[x_1]\mathcal{A}_3'[x_1]\right) \\
& \mathrm{H}^2\mathrm{E}\left(\frac{5}{672}j_3'[x_1]\mathcal{B}_3'[x_1]\right) + \qquad\qquad (4.50) \\
& \mathrm{E}\left(\frac{3}{28}j_3[x_1]\mathcal{B}_3[x_1] - \frac{5}{84}j_3'[x_1]\mathcal{B}_1[x_1]h[x_1] + \right. \\
& \quad -\frac{5}{84}h'[x_1]j_3[x_1]\mathcal{B}_1[x_1] - \frac{5}{84}j_3[x_1]j_3'[x_1]h'[x_1] + \\
& \quad -\frac{5}{84}j_3'[x_1]h[x_1]\mathcal{A}_3'[x_1] - \frac{5}{84}j_3[x_1]h'[x_1]\mathcal{A}_3'[x_1] + \\
& \quad -\frac{5}{168}j_3'[x_1]h[x_1]^2\mathcal{B}_3'[x_1] + \frac{5}{84}h[x_1]j_3[x_1]\mathcal{B}_1'[x_1] + \\
& \quad -\frac{5}{168}h[x_1]j_3'[x_1]^2 - \frac{5}{84}j_3[x_1]h[x_1]h'[x_1]\mathcal{B}_3'[x_1] + \\
& \quad \left. +\frac{5}{84}j_3[x_1]\mathcal{A}_1'[x_1]\right),
\end{aligned}$$

where the hypothesis of purely Mode-I delamination $\boldsymbol{j} = \{0, j_3\}$ has been considered.

Interestingly, the localized form of the energy (4.49-4.50) for a linear elastic material inherits the coupling of the membrane and bending from the nonlocal model.

The energy expressed in equation (4.48) can be thought to represent a material with cohesive constitutive law due to the energy associated to a jump in the displacement. The term "cohesive" is not adequate for the reduced nonlocal formulation of section 4.3, since there the jump part of the displacement is not directly causing the damage. On the contrary, in the localised energy the failure parameter μ, converging to equation (4.47), lets the crack develop as long as there is a discontinuity in the displacement.

The localised formulation of the nonlocal model introduced in section 4.3 can now be obtained by writing the lagrangian for a local plate where the internal energy is that of equations (4.49-4.50) and then minimizing it. Here, the local model based on (4.49-4.50) has been tested on the same problem as that of section 4.3.5, i.e. a cantilever plate subjected to couples acting on the free edge. The results are presented in the following graphs (Figure 4.8,4.9), for a force-controlled test. The test has been carried out until a final configuration, characterised by a curvature of $\chi_{max} = 7.4\mathrm{E}-04/L$, the corresponding acting couple of value M_{max}, and a crack advancement of $\Delta_{max} \sim \mathrm{H}$, was reached. Localisation has the result of stiffening the model, as is shown by a sensitivity analysis performed on the horizon of the nonlocal model presented in Section 4.3.

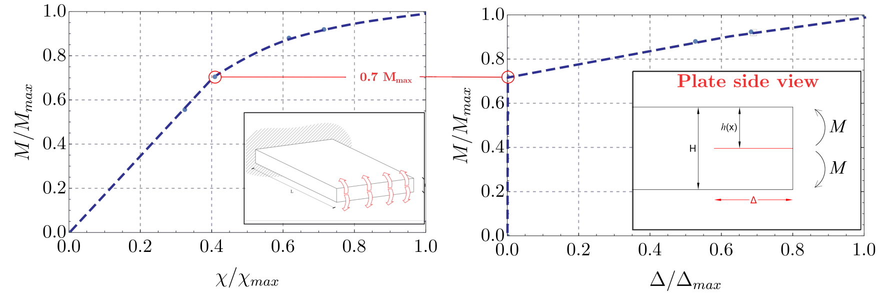

FIGURE 4.8: Acting force versus curvature (on the left); acting force versus crack advancement. Nonlinear behaviour arises due to crack propagation once the energy stored in the peridynamic bonds reaches a critical value.

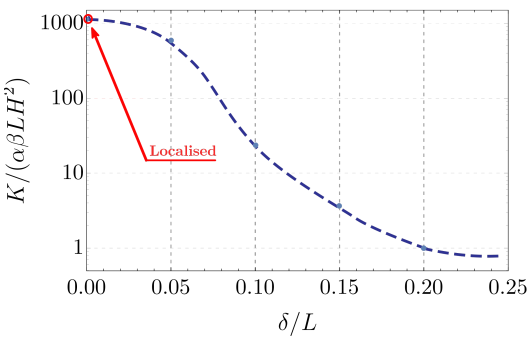

FIGURE 4.9: Sensitivity analysis performed on the nonlocal model for varying horizon (δ). Here, K is the bending stiffness, β is the constant quantity of equation (4.35), L is the length of the plate, H is the thickness, and α is a scalar depending on the load distribution.

4.4.5 Kirchhoff-like plate under mode I delamination

The kinematics of a Kirchhoff plate are readily retrieved by imposing

$$\mathcal{A}_1[x_1] \to 0, \;\; \mathcal{B}_3[x_1] \to 0, \;\; \mathcal{B}_1[x_1] \to -\mathcal{A}_3'[x_1], \tag{4.51}$$

such that

$$\boldsymbol{u}_a[x_1, x_3] = \{-\mathcal{A}_3'[x_1]x_3, \; \mathcal{A}_3[x_1]\}. \tag{4.52}$$

Mode I delamination is achieved by choosing the jump function and its derivative in the following way:

$$j_1[x_1] \to 0, \;\; j_1'[x_1] \to 0, \tag{4.53}$$

such that

$$\boldsymbol{u}_J[x_1, x_3] = \{0, j_3[x_1]\,\Theta(x_3 - h[x_1])\}, \tag{4.54}$$

where Θ is the heaviside function. Under these conditions the terms of localised energy become

$$\mathcal{E}_{local,a} = \frac{1}{224}\mathrm{EH}^3\mathcal{A}_3''[x_1]^2, \tag{4.55}$$

and

$$\begin{aligned}\mathcal{E}_{local,J} = & -\mathrm{E}\,\Bigg(\frac{5}{84}j_3[x_1]h[x_1]\mathcal{A}_3''[x_1] - \frac{5}{84}j_3[x_1]j_3'[x_1]h'[x_1] - \frac{5}{168}h[x_1]j_3'[x_1]^2 + \\ & + \frac{5}{336}j_3'[x_1]^2\Bigg)\end{aligned} \tag{4.56}$$

respectively. It is worth mentioning that the retrieved local energy for the continuous part of the displacement is a quantity resembling the classical result for Kirchhoff plates: $\mathcal{E}_{local,a} = \frac{\mathrm{H}^3\mathrm{E}}{12(1-\nu^2)}\mathcal{A}_3''[x_1]^2$, where for obvious reasons a Poisson ratio of $1/4$ has to be considered.

4.5 Conclusions

The peridynamic theory of continuum mechanics is a rather new field of research. Due to its recent formulation certain problems remain unaddressed. One of them is studied in the present paper, where the formulation of a reduced model for the explicit study of though-thickness delamination of thin structures is put forward.

The model is obtained by making an hypothesis on the kinematics of the thin element, which is assumed as the sum of a continuous part and a jump part. A particular choice of these fields is made which express the dependance on the out-of-plane variable explicitly, thus making the integration through the thickness feasible. The resulting reduced model retains information on delamination through the functions defining the jump displacement. The reduction procedure generates a hierarchy of terms in the elastic energy stored inside the plate. A mechanical interpretation of those terms is possible (especially for the part of the energy associated to the continuous part of the displacement) and is proposed. The model is then tested against a numerical simulation using standard FEM analysis of BPD and a good agreement is found. The nonlocal feature of the model allows to retrieve a reduced formulation were coupling of membrane and bending behaviour occurs despite the formulation is expressed for a linear setting. To further exploit this aspect, localization of the nonlocal model is performed. Firstly, the convergence of the nonlocal energy formulation to a finite and non-vanishing local energy is assessed and then tested for a simple case. The localized reduced model shows (i.) coupling of bending and stretching and (ii.) a cohesive nature. Cohesiveness is expressed by the fact that energy can be stored by the part of the energy associated to the discontinuous displacement field when a fracture is propagating.

Bibliography

[1] A.H. Hueuer et al. “Innovative Materials Processing Strategies: A Biomimetic Approach”. In: *Science* 255 (1992), pp. 1098–1105.

[2] C.E. Bryne and D.C. Nagle. “Cellulose derived composites - A new method for materials processing”. In: *Mat. Res. Innovat.* 1 (1997), pp. 137–144.

[3] P. Greil. “Biomorphous ceramics from lignocellulosics”. In: *Journal of the European Ceramic Society* 21 (2011), pp. 105–118.

[4] P. Greil, T. Lifka, and A. Kaindl. “Biomorphic Cellular Silicon Carbide Ceramics from Wood: I. Processing and Microstructure”. In: *J. Eu. Ceram. Soc.* 18 (1998), pp. 1961–1973.

[5] C.R. Rambo et al. “Microcellular Al_2O_3 Ceramics from Wood for Filter Applications”. In: *J. Am. Ceram. Soc.* 91.3 (2008), pp. 852–859.

[6] J. Qian et al. “Fabrication, chemical composition change and phase evolution of biomorphic hydroxyapatite”. In: *J Mater Sci: Mater Med* 19 (2008), pp. 3373–3383.

[7] C. Eichenseer et al. “Biomorphous porous hydroxyapatite-ceramics from rattan (Calamus Rotang)”. In: *J. Mater. Sci.: Mater. Med.* 21 (2010), pp. 131–137.

[8] W.R. Legant et al. “Microfabricated tissue gauges to measure and manipulate forces from 3D microtissues”. In: *Proceedings of the National Academy of Sciences* 106.25 (2009), pp. 10097–10102.

[9] G. W. Kooistra, V. S. Deshande, and H. N. G. Wadley. “Hierarchical corrugated core sandwich panel concepts”. In: *Journal of applied mechanics* 74.2 (2007), pp. 259–268.

[10] F.P.W. Melchels et al. “Mathematically defined tissue engineering scaffold architectures prepared by stereolithography”. In: *Biomaterials* 31 (2010), pp. 6909–6916.

[11] N. Fleck, V. S. Deshande, and M.F. Ashby. “Micro-architectured materials: past, present and future”. In: *Proc. R. Soc. A* 466 (2010), pp. 2495–2516.

[12] A. Tampieri et al. “From wood to bone: multi-step process to convert wood hierarchical structures into biomimetic hydroxyapatite scaffolds for bone tissue engineering”. In: *Journal of Materials Chemistry* 19 (2009), pp. 4973–4980.

[13] D. Bigoni et al. "Ceramics with the signature of wood: a mechanical insight". In: *Materials Today Bio* 5 (2020), p. 100032.

[14] M. Valentini et al. "Crack propagation in a brittle elastic material with defects". In: *Journal of Applied Mechanics* 6 (1999), pp. 79–86.

[15] A.B. Movchan. "Integral characteristics of elastic inclusions and cavities in the two-dimensional theory of elasticity". In: *European Journal Applied Mathematics* 3 (1992), pp. 21–30.

[16] A.B. Movchan and N.V. Movchan. *Mathematical modelling of solids with non regular boundaries*. CRC Press, Boca Raton, FL, 1995.

[17] T.N. Blittencourt et al. "Quasi-Automatic simulation of crack propagation for 2D LEFM problems". In: *Eng. Fracture Mechanics* 55 (1996), pp. 321–334.

[18] M. Hori and N. Vaikuntan. "Rigoruos formulation of crack path in two dimensional elastic body". In: *Mechanics of Materials* 26 (1997), pp. 1–14.

[19] Y. Sumi, S. Nemat-Nasser, and L.M. Keer. "On crack branching and curving in a finite body". In: *Int. J. Fracture* 21 (1983), pp. 67–79.

[20] D. Misseroni et al. "Experimental and analytical insights on fracture trajectories in brittle materials with voids". In: *International Journal of Solids and Structures* 63 (2015), pp. 219–225.

[21] G. Noselli, V.S. Deshpande, and N.A. Fleck. "An analysis of competing toughening mechanisms in layered and particulate solids". In: *Int. J. Fracture* 183 (2013), pp. 241–258.

[22] G. Xu, A.F. Bower, and M. Ortiz. "The influence of crack trapping on the toughness of fibre reinforced composites". In: *J. Mech. Phys. Solids* 46 (1998), pp. 1815–1833.

[23] R. Cavuoto et al. "Crack growth via phase-field modelling and failure of ceramics with multiscale porosity". Submitted.

[24] A.P. Roberts and E.J. Garboczi. "Elastic Properties of Model Porous Ceramics". In: *J. Am. Ceram. Soc.* 83 (2000), pp. 3041–48.

[25] W. Pabst, E. Gregorova, and G. Ticha. "Elasticity of porous ceramics - A critical study of modulus-porosity relations". In: *J. Eu. Ceram. Soc.* 26 (2006), pp. 1085–97.

[26] C.G. Sammis and M.F. Ashby. "The failure of brittle porous solids under compressive stress states". In: *Acta metall.* 34 (1986), pp. 511–526.

[27] M.E. Gurtin. *The Linear Theory of Elasticity*. Ed. by C. Truesdell. Springer-Verlag, Berlin, 1972.

[28] M.F. Ashby. "The mechanical properties of cellular solids". In: *Metallurgical Transactions A* 14 (1983), pp. 1755–1769.

[29] L. J. Gibson and M. F. Ashby. *Cellular solids - structure and properties*. 2nd ed. Cambridge: Cambridge University Press, 1999.

[30] R.W. Rice. “Evaluation and extension of physical property-porosity models based on minimum solid area”. In: *Journal of materials science* 31 (1996), pp. 102–118.

[31] S. Nemat-Nasser and M. Hori. *Micromechanics: overall properties of heterogeneous materials*. 2nd ed. North Holland, 1999.

[32] F.W. Nyongesaa and B.O. Aduda. “Fracture Strength of Porous Ceramics: Stress Concentration Vs Minimum Solid Area Models”. In: *African Journal of Science and Technology* 5 (2006).

[33] R.W. Rice. “Limitations of pore-stress concentrations on the mechanical properties of porous materials”. In: *Journal of materials science* 32 (1997), pp. 4731–36.

[34] Y. Cui, Y.F. Gao, and H.B. Chew. “Two-scale porosity effects on cohesive crack growth in a ductile media”. In: *Int. J. Sol. Struc.* 200 (2020), pp. 188–197.

[35] S.A. Silling. “Reformulation of elasticity theory for discontinuities and long-range forces”. In: *Journal of the Mechanics and Physics of Solids* 48.1 (2000), pp. 175–209. ISSN: 0022-5096. DOI: `https://doi.org/10.1016/S0022-5096(99)00029-0`. URL: `https://www.sciencedirect.com/science/article/pii/S0022509699000290`.

[36] T. Inoue et al. “Delamination effect on impact properties of ultrafine-grained low-carbon steel processed by warm caliber rolling”. In: *Metall. Mater. Trans. A* 41 (2010), pp. 341–355.

[37] B.P. Naganarayana and S.N. Atluri. “Strength reduction and delamination growth in thin and thick composite plates under compressive loading”. In: *Computational Mechanics* 16 (1995), pp. 170–189.

[38] D.S. Dugdale. “Yielding of steel sheets containing slits”. In: *Journal of the Mechanics and Physics of Solids* 8 (1960), pp. 100–104.

[39] G.I. Barenblatt. “The Mathematical Theory of Equilibrium Cracks in Brittle Fracture”. In: *Advances in Applied Mechanics* 7 (1962), pp. 55–129.

[40] A. Hillerborg, M. Modeer, and P.-E. Petersson. “Analysis of crack formation and crack growth in concrete by means of fracture mechanics and finite elements”. In: *Cement and Concrete Research* 6 (1976), pp. 773–781.

[41] A. Turon et al. “An engineering solution for mesh size effects in the simulation of delamination using cohesive zone models”. In: *Engineering Fracture Mechanics* 74 (2007), pp. 1665–1682.

[42] M. Elices et al. “The cohesive zone model: advantages, limitations and challages”. In: *Eng. Fract. Mech.* 69 (2002), pp. 137–163.

[43] C. Fan, P.-Y. Ben Jar, and J.J. Roger Cheng. “Cohesive zone with continuum damage properties for simulation of delamination in fibre composites and failure of adhesive joints”. In: *Engineering Fracture Mechanics* 75 (2008), pp. 3866–3880.

[44] F. Erdogan and M. Ozturk. “On the singularities in fracture and contact mechanics”. In: *Journal of applied mechanics* 75 (2008), pp. 051111–1–12.

[45] I.A. Kunin. *Theory of elastic media with a microstructure: Nonlocal theory of elasticity*. Moscow, Izdatel’stvo Nauka, 1975.

[46] A.C. Eringen. “Linear theory of nonlocal elasticity and dispersion of plane waves”. In: *Int. J. Eng. Sci.* 10.5 (1972), pp. 425–435.

[47] A.C. Eringen. “Nonlocal continuum theory of liquid crystals”. In: *Mol. Cryst. Liq. Cryst.* 75 (1981), pp. 321–343.

[48] Y.Z. Povstenko. “The nonlocal theory of elasticity and its applications to the description of defects in solid bodies”. In: *J Math Sci* 97 (1999), pp. 3840–3845.

[49] S. Patnaik, S. Sidhardh, and F. Semperlotti. “Towards a Generalized Approach to Nonlocal Elasticity via Fractional Order Mechanics”. In: *International Journal of Mechanical Sciences* 189.1 (2020), p. 105992.

[50] P. Seleson et al. “Perydinamics as an up-scaling of molecular dynamics”. In: *Multiscale Modeling and Simulation* 8 (2009), pp. 204–227.

[51] M. Zimmermann. “A Continuum Theory with Long-Range Forces for Solids”. PhD thesis. Department of Mechanical Engineering, 2005.

[52] D. Han et al. “The Review of the Bond-based Peridynamics Modeling”. In: *Journal of Micromechanics and Molecular Physics* 4.1 (2019), p. 1830001.

[53] S.A. Silling. “Linearized theory of peridynamic states”. In: *Journal of Elasticity* 99.1 (2010), pp. 85–111.

[54] Y. Gao and S. Oterkus. “Ordinary State-based Peridynamic modelling for fully coupled thermoelastic problems”. In: *Continuum Mech. Thermodyn.* 31 (2019), pp. 907–937.

[55] L. Jooeun, L. Wenyang, and H. Jung-Wuk. “Impact fracture analysis enhanced by contact of peridynamic and finite element formulations”. In: *International Journal of Impact Engineering* 87 (2016), pp. 108–119.

[56] N. Liu, D. Liu, and W. Zhou. “Peridynamic modelling of impact damage in three-point bending beam with offset notch”. In: *Appl. Math. Mech.-Engl. Ed.* 38 (2017), pp. 99–110.

[57] J. Xu et al. “Peridynamic Analysis of Impact Damage in Composite Laminates”. In: *Journal of Aerospace Engineering* 21 (2008).

[58] F. Bobaru and Y. D. Ha. “Adaptive Refinement and Multiscale Modeling in 2D Peridynamics”. In: *Journal for Multiscale Computational Engineering* 9.6 (2011), pp. 635–659.

[59] Q.V. Le, W.K. Chan, and J. Schwartz. “A two-dimensional ordinary state based peridynamic model for linearly elastic solids”. In: *Int. J. Numer. Meth. Eng.* 98 (2014), pp. 547–561.

[60] G. Sarego et al. "Linearized State-based Peridynamics for 2D Problems". In: *Int. J. Numer. Meth. Eng.* 108.10 (2016), pp. 1174–1197.

[61] X.-W. Jiang et al. "Peridynamic modeling of Mode-I delamination growth in double contilever composites beam test: a Two-dimensional modeling using revised energy-based failure criteria". In: *Appl. Sci.* 9 (2019), p. 656.

[62] U. Yolum et al. "Peridynamic modelling of delamination in DCB specimen". In: *Procedia Structural Integrity* 13 (2018), pp. 2126–2131.

[63] Y.L. Hu, N.V. De Carvalho, and E. Madenci. "Peridynamic modeling of delamination growth in composites laminates". In: *Comp. Struct.* (2015).

[64] S.A. Silling and F. Bobaru. "Peridynamic modeling of membranes and fibers". In: *International Journal of Non-Linear Mechanics* 40 (2005), pp. 395–409.

[65] M. Taylor and D.J. Steigmann. "A two-dimensional pridynamic model for thin plates". In: *Mathematics and Mechanics of Solids* 20.8 (2013), pp. 998–1010.

[66] R. Cavuoto et al. "A reduced peridynamic model for through-thickness delamination of thin films." Submitted.

[67] R. Choksi et al. "Structured Deformations as Energy Minimizers in Models of Fracture and Hysteresis". In: *Mathematics and Mechanics of Solids* 4.3 (1999), pp. 321–356.

[68] Z. Yang et al. "Implementation of Peridyanmics Beam and Plate Formulations in Finite Element Framework". In: *Continuum Mech. Thermodyn.* 31 (2019), pp. 301–315.

[69] R.W. Macek and S.A. Silling. "Peridynamics via finite element analysis". In: *Finite Elements in Analysis and Design* 43 (2007), pp. 1169–1178.

[70] P. Fratzl and R. Weinkamer. "Nature's Hierarchical Materials". In: *Material Science* 52 (2007), pp. 1263–1334.

[71] R. Weinkamer and P. Fratzl. "Mechanical Adaptation of Biological Materials - the Example of Bone and Wood". In: *Material Science and Engng. C-Materials for Biological Appl.* 31 (2011), pp. 1164–1173.

[72] A. Buehrig et al. "Biomimetic cellular metals-using hierarchical structuring for energy absorption". In: *Bioinspiration and Biomimetics* 11.4 (2016).

[73] M. Fraldi et al. "A hybrid deterministic-probabilistic approach to model the mechanical response of helically arranged hierarchical strands". In: *J. Mech. Phys. Solids* 106 (2016), pp. 338–352.

[74] F. Ongaro, E. Barbieri, and N.M. Pugno. "The in-plane elastic properties of hierarchical composite cellular materials: Synergy of hierarchy, material heterogeneity and cell topologies at different levels". In: *Mechanics of Materials* 103 (2016), pp. 135–147.

[75] F. Ongaro et al. “Mechanics of filled cellular materials”. In: *Mech. Materials* 97 (2016), pp. 26–47.

[76] A. Vigliotti and D. Pasini. “Mechanical properties of hierarchical lattices”. In: *Mechanics of Materials* 62 (2013), pp. 32–43.

[77] Z.L. Yu et al. “Bioinspired polymeric woods”. In: *Sci. Advances* 4 (2018).

[78] L. Zorzetto and D. Ruffoni. “Wood-Inspired 3D-Printed Helical Composites with Tunable and Enhanced Mechanical Performance”. In: *Adv. Funct. Materials* 28 (2018).

[79] F. Libonati et al. “Mechanics of collagen-hydroxyapatite model nanocomposites”. In: *Mechanics Research Communications* 58 (2014), pp. 17–23.

[80] G.X. Gu et al. “Unraveling the role of nacre’s mineral bridges”. In: *Journal of the mechanical behavior of biomedical materials* 76 (2107), pp. 135–144.

[81] F. Libonati et al. “Bone-Inspired Materials by Design: Toughness Amplification Observed Using 3D Printing and Testing”. In: *Advanced Engineering Materials* 18.8 (2016), pp. 1299–1310.

[82] F. Auricchio et al. “A novel layered topology of auxetic materials based on the tetrachiral honeycomb microstructure”. In: *Materials and Design* 179 (2019).

[83] C.T. Bauer et al. “Hierarchical macroscopic fibrillar adhesives: in situ study of buckling and adhesion mechanisms on wavy substrates”. In: *Bioinspir. Biomim.* 10 (2015), p. 066002.

[84] L. Bardella et al. “A critical evaluation of micromechanical models for syntactic foams”. In: *Mechanics of Materials* 50 (2012), pp. 53–69.

[85] U. Sabu et al. “Microwave assisted synthesis of biomorphic hydroxyapatite”. In: *Ceramics International* 45 (2019), pp. 6718–6722.

[86] A. Tampieri, S. Sprio, and A. Ruffini. “Study of the hydrothermal transformation of wood- derived calcium carbonate into 3D hierarchically organized hydroxyapatite”. In: *Chemical Engineering Journal* 217 (2013), pp. 150–158.

[87] A. Tampieri et al. “Heterogeneous chemistry in the 3-D state: an original approach to generate bioactive, mechanically-competent bone scaffolds”. In: *Biomaterials Science* 7 (2019), pp. 307–321.

[88] J. Szekely. *Gas-solid Reactions*. 1st ed. Academic Press, 1976.

[89] R.I. Martin and P.W. Brown. “Mechanical properties of hydroxyapatite formed at physiological temperature”. In: *Journal of Material Science: Materials in Medicine* 6 (1995), pp. 138–143.

[90] A.J. Wagoner Johnson and B.A. Herschler. “A review of the mechanical behavior of CaP and CaP/polymer composites for applications in bone replacement and repair”. In: *Acta Biomaterialia* 7 (2011), pp. 16–30.

[91] J. Cao, C.R. Rambo, and H. Sieber. “Preparation of Porous Al2O3-Ceramics by Biotemplating of Wood”. In: *J. Por. Mat* 11 (2004), pp. 163–172.

[92] C.R. Rambo and H. Sieber. “Novel Synthetic Route to Biomorphic Al2O3 Ceramics”. In: *Adv. Mater.* 17.8 (2005), pp. 1088–1091.

[93] M. Singh and B.M. Yee. “Reactive processing of environmentally conscious, biomor- phic ceramics from natural wood precursors”. In: *J. Eu. Cer. Soc.* 24.2 (2004), pp. 209–217.

[94] J. Cao, O. Rusina, and H. Sieber. “Processing of porous TiO2-ceramics from biological preforms”. In: *Cer. Inter.* 30.7 (2004), pp. 1971–1974.

[95] X. Li et al. “Synthesis and hierarchical pore structure of biomorphic manganese oxide derived from woods”. In: *J. Eu. Ceram. Soc.* 26 (2006), pp. 3657–3664.

[96] S. Binghe et al. “The synthesis and microstructure of morph-genetic TiC/C ceramics”. In: *Carbon* 42 (2004), pp. 177–182.

[97] C.R. Rambo et al. “Manufacturing of biomorphic (Si, Ti, Zr)-carbide ceramics by sol-gel processing”. In: *Carbon* 43 (2005), pp. 1174–1183.

[98] L. Esposito et al. “Microstructure and properties of porous b-SiC template from soft woods”. In: *J. Eu. Cer. Soc.* 24 (2004), pp. 533–540.

[99] V.E. Tarasov. “Elasticity of fractal materials using the continuum model with non-integer dimensional space”. In: *Comptes Rendus Mechanique* 343.1 (2015), pp. 57–73.

[100] V. Kunin et al. “Static and dynamic elastic properties of fractal-cut materials”. In: *Extreme Mechanics Letters* 6 (2016), pp. 103–114.

[101] X. Zhai et al. “Real-time visualisation of dynamic fractures in porcine bones and the loading-rate effect on their fracture toughness”. In: *Journal of the Mechanics and Physics of Solids* 131 (2019), pp. 258–371.

[102] D. Yin et al. “Mechanical test and fractal analysis on anisotropic fracture of cortical bone”. In: *Applied Surface Science* 357 (2015), pp. 2063–2069.

[103] *ASTM C1424 - 04 Standard test method for monotonic compressive strength of ad- vanced ceramics at ambient temperature. ASTM C1424 - 04 Standard test method for monotonic compressive strength of advanced ceramics at ambient temperature.*

[104] *ASTM C1161 - 18 Standard test method for flexural strength of advanced ceramics at ambient temperature.*

[105] F. Libonati et al. “Fracture mechanics of hydroxyapatite single crystals under geometric confinement”. In: *Journal of the mechanical behavior of biomedical materials* 20 (2013), pp. 184–191.

[106] M. Gei, D. Bigoni, and S. Guicciardi. “Failure of silicon nitride under uniaxial compression at high temperature”. In: *Mechanics of Materials* 36 (2004), pp. 335–345.

[107] S. Timoshenko and J.N. Goodier. *Theory of Elasticity*. 2nd ed. McGraw-Hill, 1951.

[108] S. Timoshenko. "On the distribution of stresses in a circular ring compressed by two forces acting along a diameter". In: *The London, Edinburgh, and Dublin Philosophical Magazine and Journal of Science* 44 (1922), pp. 1014–1019.

[109] E.A. Ripperger and N. Davids. "Critical Stresses in Circular Ring". In: *America Society of Civil Engineering* 2308 (1946), pp. 619–628.

[110] J.C. Jeager and R. Hoskins. "Stresses and failure in rings of rock load in diametral tension or compression". In: *Brit. J. Appl. Phys.* 17 (1966), pp. 685–695.

[111] D.W. Hobbs. "The tensile strength of rocks". In: *Int. J. Rock Mech. Mining Sci.* 1 (1963), pp. 385–396.

[112] J.A. Hudson. "Tensile strength and the ring test". In: *Int. J. Rock Mech. Mining Sci.* 6 (1968), pp. 91–97.

[113] L.S. Srinath and Y.V.G. Acharya. "Stresses in a Circular Ring". In: *Appl. Sci. Res.* 4 (1954), pp. 189–194.

[114] B. Choi et al. "Measurement of tensile strength of brittle rocks using a half ring shaped specimen". In: *Geosciences Journal* 23 (2019), pp. 649–660.

[115] *UNI EN 583-3 - Non destructive testing - Ultrasonic examination - Transmission technique.*

[116] *BS EN 408-2010-A1 2012- Timber structures. Structural timber and glued laminated timber. Determination of some physical and mechanical properties.*

[117] *ISO 8375:2009 - Timber structures — Glued laminated timber — Test methods for determination of physical and mechanical properties.*

[118] *ISO/TR 22157-1 2004 - Bamboo — Determination of physical and mechanical prop- erties — Part 1: Laboratory manual.*

[119] *ISO/TR 22157-2 2004 - Bamboo — Determination of physical and mechanical prop- erties — Part 2: Requirements.*

[120] A.A. Abdel-Wahab, K. Alam, and V.V. Silberschmidt. "Analysis of anisotropic viscoelastoplastic properties of cortical bone tissues". In: *Journal of the mechanical behavior of biomedical materials* 4.5 (2011), pp. 807–820.

[121] Y.C. Fung. *Biomechanics: Mechanical Properties of Living Tissues*. 2nd ed. Springer, 1993.

[122] Y.H. An and R.A. Draughn. *Mechanical Testing of Bone and the Bone-Implant Interface*. CRC Press, 2000.

[123] M. Cuppone et al. "The Longitudinal Young's Mod- ulus of Cortical Bone in the Midshaft of Human Femur and its Correlation with CT Scanning Data". In: *Calcif Tissue Int* 74 (2004), pp. 302–309.

[124] K.V. Arun and K.K. Jadhav. “Behaviour of Human Femur Bone Under Bending and Impact Loads”. In: *European Journal of Clinical and Biomedical Sciences* 2.2 (2016), pp. 6–13.

[125] J.H. McElhaney et al. “Mechanical properties of cranial bone”. In: *J. Biomechanics* 3 (1970), pp. 495–511.

[126] M. Biggemann, D. Hilweg, and P. Brinckmann. “Prediction of the compressive strength of vertebral bodies of the lumbar spine by quantitative computed tomography”. In: *Skeletal Radiol* 17 (1988), pp. 264–269.

[127] A.B. Movchan, S.A. Nazarov, and O.R. Polyakova. “The quasi-static growth of a semi-infinite crack in a plane containing small defects.” In: *Comptes Rendus de L’Academie des Sciences., Paris, Series II* 313 (1991), pp. 1223–1228.

[128] Y. Sumi. “Computational crack path prediction.” In: *Theoretical and Applied Fracture Mechanics* 4 (1985), pp. 149–156.

[129] K.T. Faber and A.G. Evans. “Crack deflection processes-I. Teory and -II. Experiment”. In: *Acta Metallurgica* 31 (1983), pp. 565–584.

[130] D. Misseroni. “Experiments on fracture trajectories in ceramic samples with voids.” In: *Journal of the European Ceramic Society* 36 (2016), pp. 2277–2281.

[131] M. Mirkhalaf, A.K. Dastjerdi, and F. Barthelat. “Overcoming the brittleness of glass through bio-inspiration and micro-architecture.” In: *Nature Communications* 5 (2014), p. 3166.

[132] G.A. Francfort and J.J. Marigo. “Revisiting brittle fracture as an energy minimization problem”. In: *Journal of the Mechanics and Physics of Solids* 46 (1998), pp. 1319–1342.

[133] B. Bourdin, G.A. Francfort, and J.J. Marigo. “The Variational Approach to Fracture”. In: *Journal of Elasticity* 91 (2008), pp. 5–148.

[134] G. Dal Maso and R. Toader. “Existence and approximation results”. In: *A model for the quasistatic growth of brittle fractures, existance and approximation results* 162 (2002), pp. 101–135.

[135] L. Ambrosio and V.M. Tortorelli. “Approximation of functionals depending on jumps by elliptic functionals via Gamma-convergence”. In: *Communications on Pure and Applied Mathematics* 43 (1990), pp. 999–1036.

[136] L. Ambrosio and V.M. Tortorelli. “On the approximation of free discontinuity problems”. In: *Boll.Un.Mat.Ital.* 6 (1992), pp. 105–123.

[137] *An introduction to Gamma-convergence* (1993).

[138] D.P. Braides. *Approximation of Free Discontinuity Problems*. Springer Verlag, Berlin, 1998.

[139] D.P. Braides. *Gamma-convergence for beginners*. Oxford University Press, New York, 2002.

[140] C. Miehe, M. Hofacker, and F. Welschinger. "A phase field model for rateindependent crack propagation: robust algorithmic implementation based on operator splits". In: *Comput. Methods Appl. Mech. Engng.* 199 (2010), pp. 2765–2778.

[141] C. Miehe, F. Welschinger, and M. Hofacker. "Thermodynamically consistent phase-field models of fracture: variational principles and multi-field fe-implementation". In: *Int. J. Numer. Methods Engrg.* 83 (2010), pp. 1273–1311.

[142] I.S. Aranson, V.A. Kalatsky, and V.M. Vinokur. "Continuum field description of crack propagation". In: *Phys Rev Lett* 85 (2000), pp. 118–121.

[143] A. Karma, D.A. Kessler, and H. Levine. "Phase-field model of mode III dynamic fracture". In: *Phys Rev Lett* 87 (2001), p. 045501.

[144] V. Hakim and A. Karma. "Laws of crack motion and phase-field models of fracture". In: *J Mech Phys Solids* 57 (2009), pp. 342–368.

[145] H. Henry and H. Levine. "Dynamic instabilities of fracture under biaxial strain using a phase field model". In: *Phys Rev Lett* 93 (2004), p. 105504.

[146] C. Kuhn and R. Muller. "A phase field model for fracture". In: *Proc Appl Math Mech* 8 (2008), pp. 10223–10224.

[147] C. Kuhn and R. Muller. "A continuum phase field model for fracture". In: *Eng Fract Mech* 77 (2010), pp. 3625–34.

[148] H. Amor, J.J. Marigo, and C. Maurini. "Regularized formulation of the variational brittle fracture with unilateral contact: numerical experiments". In: *J Mech Phys Solids* 57 (2009), pp. 1209–29.

[149] S. Sprio et al. "Hierarchical porosity inherited by natural sources affects the mechanical and biological behaviour of bone scaffolds". In: *Journal of the European Ceramic Society* 40 (2020), pp. 17717–1727.

[150] M.J. Borden et al. "A phase-field description of dynamic brittle fracture". In: *Comput. Methods Appl. Mech. Engrg.* 217-220 (2012), pp. 77–95.

[151] A.A. Griffith. "The phenomena of rupture and flow in solids". In: *Philos. Trans. Royal Soc. London A* 221 (1921), pp. 163–198.

[152] V.A. Lubarda, D. Kracjinvovic, and S. Mastilovic. "Damage model for brittle elastic solids with unequal tensile and compressive strength". In: *Engineering Fracture Mechanics* 49 (1994), pp. 681–697.

[153] B.D. Coleman and W. Noll. "The thermodynamics of elastic materials with heat conduction and viscosity". In: *Archives for Rational Mechanics and Analysis* 13 (1963), pp. 167–178.

[154] M.A. Msekh et al. "Abaqus implementation of phase-field model for brittle fracture". In: *Comput. Mater. Sci.* 96 (2015), pp. 472–484.

[155] J. Wambacq et al. "Interior-point methods for the phase-field approach to brittle and ductile fracture". In: *Comput. Methods Appl. Mech. Engrg.* 375 (2021), p. 113612.

[156] D. Jodlbauer, U. Langer, and W. Thomas. "Parallel Matrix-Free Higher-Order Finite Element Solvers for Phase-Field Fracture Problems". In: *Mathematical and Computational Applications* 25.3 (2020).

[157] R.W. Rice. "Porosity of ceramics". In: Marcel Dekker Inc, 1998, pp. 211–212.

[158] R.W. Rice. "Microstructure dependance of mechanical behaviour of ceramics". In: *Treatise on materials science and technology* 11 (1977), pp. 199–378.

[159] R.W. Rice. "Comparison of stress concentration versus minimum solid area based mechanical property-porosity relations". In: *Journal of Materials Science* 28 (1993), pp. 2187–2190.

[160] J. Dolbow and T. Belytschko. "A finite element method for crack growth without remeshing". In: *Int. J. Numer. Meth. Eng.* 46.1 (1999), pp. 131–150.

[161] K. Zhou and D. Qiang. "Mathematical and numerical analysis of linear peridynamic models with nonlocal boundary conditions". In: *Siam J. Numer. Anal.* 48.5 (2010), pp. 1759–1780.

[162] Q. Du and K. Zhou. "Mathematical Analysis for the Peridynamic Nonlocal Continuum Theory". In: *Mathematical Modeling and Numerical Analysis* 45 (2011), pp. 217–234.

[163] J.T. Foster, S.A. Silling, and W. Chen. "An energy based failure criterion for use with peridynamic states". In: *International Journal for Multiscale Computational Engineering* 9 (2011), pp. 675–687.

[164] H. Zhang and P. Qiao. "A two-dimensional ordinary state-based peridynamic model for elastic and fracture analysis". In: *Engineering Fracture Mechanics* 232 (2020), p. 107040.

[165] E. Madenci and S. Oterkus. "Ordinary State-based Peridynamics for plastic deformation according to von Mises yield criteria with isotropic hardening". In: *J. Mech. Phys. Solids* 86 (2016), pp. 192–219.

[166] S.A. Silling and R.B. Lehoucq. "Peridynamic theory of solid mechanics". In: *Advances in Applied Mechanics* 44 (2010), pp. 73–168.

[167] P. Elbau. "Sequential Lower Semi-Continuity of Non-Local Functionals". In: *arXiv: Functional Analysis* (2011).

[168] D. Foss, P. Radu, and C. Wright. "Existence and regularity of minimizers for nonlocal energy functionals". In: *Differential and Integral Equations* 31.11-12 (2018), pp. 807–832.

[169] T. Mengesha and Q. Du. "On the variational limit of a class of nonlocal functionals related to peridynamics". In: *Nonlinearity* 28 (2015), pp. 3999–4035.

[170] J.C. Bellido and C. Mora-Corral. “Existence for nonlocal variational problems in peridynamics”. In: *Siam J. Numer. Anal.* 46.1 (2014), pp. 890–916.

[171] B. Aksoylu and T. Mengesha. “Results on nonlocal boundary value problems”. In: *Numerical Functional Analysis and Optimization* 31.12 (2010), pp. 1301–1317.

[172] F. Bobaru et al. “Convergence, adaptive refinement, and scaling in 1D peridynamics”. In: *Int. J. Numer. Meth. Eng.* 77 (2009), pp. 852–877.

[173] J.C. Bellido, C. Mora-Corral, and P. Pedregal. “Hyperelasticity as a Gamma-limit of Peridynamics when the Horizon goes to Zero”. In: *Calculus of Variations and Partial Differential Equations* 54 (2015), pp. 1643–1670.

[174] J.C. Bellido, J. Cueto, and C. Mora-Corral. “Bond-based peridynamics does not converge to hyperelasticity as the horizon tend to zero”. In: *Journal of Elasticity* 141 (Sept. 2020).

[175] S.A. Silling and R.B. Lehoucq. “Convergence of Peridynamics to Classical Elasticity Theory”. In: *Journal of Elasticity* 93 (2008), p. 13.

UNIVERSITY OF TRENTO

Phase-field and reduced peridynamic theories for fracture problems

Riccardo Cavuoto